Improvements on the application of direct-CFD in high-fidelity unsteady aeroelastic simulations

Master Thesis

H. Verdonck

Faculty of Aerospace Engineering
Delft University of Technology

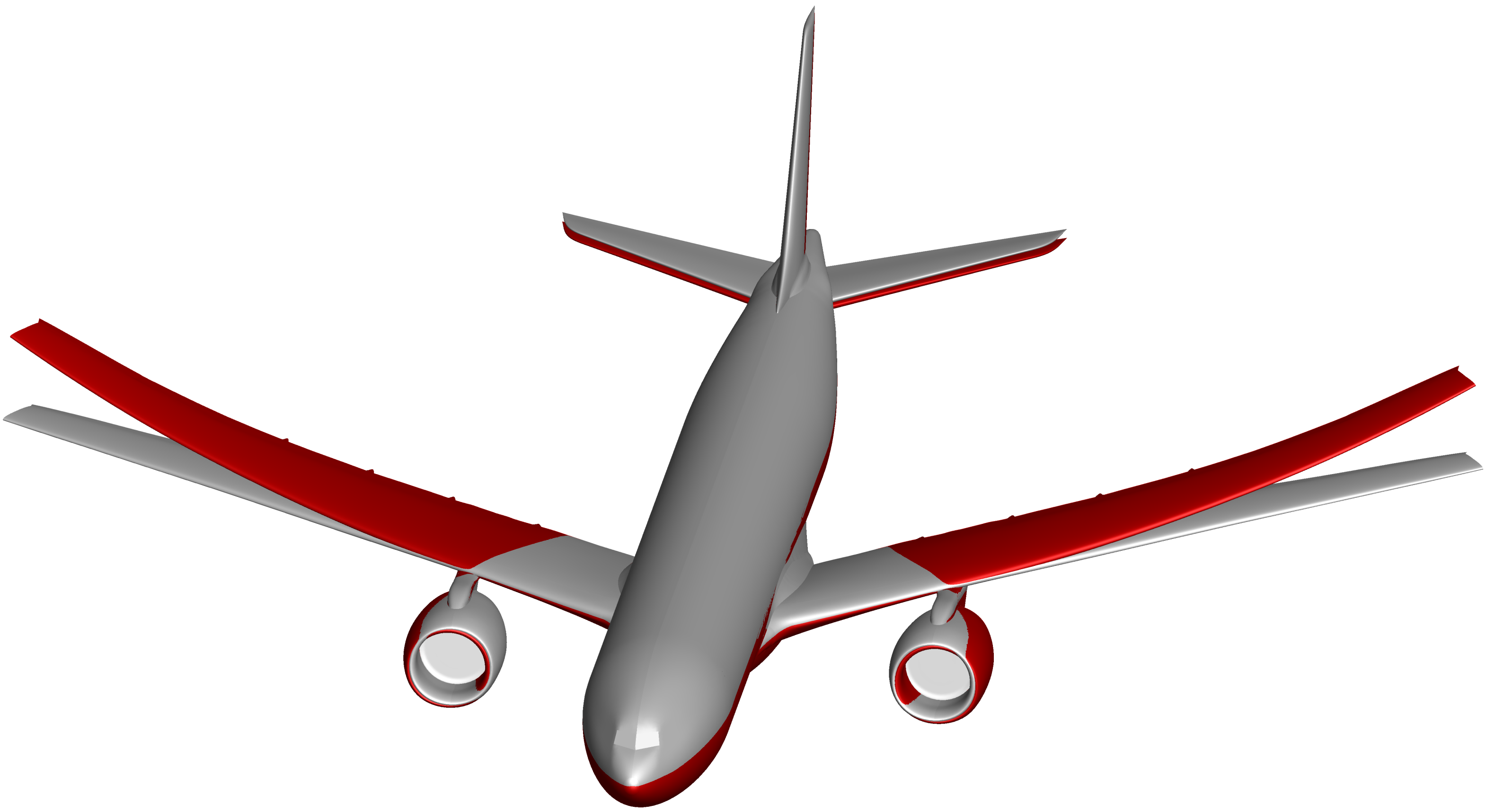

TU Delft

AIRBUS

Improvements on the application of direct-CFD in high-fidelity unsteady aeroelastic simulations

Master Thesis

by

H. Verdonck

to obtain the degree of Master of Science
at the Delft University of Technology,
to be defended publicly on Monday February 25, 2019 at 10:00 AM.

Student number:	4298195	
Project duration:	June 1, 2018 – February 28, 2019	
Thesis committee:	Dr. ir. A. H. van Zuijlen,	TU Delft, supervisor
	Dr. ir. M. I. Gerritsma,	TU Delft
	Dr. ir. J. G. Holierhoek,	TU Delft
	Ir. H. Bleecke,	Airbus GmbH, supervisor

This thesis is confidential and cannot be made public until February 25, 2029.

An electronic version of this thesis is available at `http://repository.tudelft.nl/`.

TU Delft

Abstract

Aircraft manufacturers have to prove a flutter free design for all operational cases within the complete flight envelope plus a safety margin. This certification process relies on validated flutter computations which have to be made for all flight conditions including variations in the aircraft's loading and failure cases. The aerodynamic component of these unsteady aeroelastic simulations is restricted to fast computational methods due to the large parameter space. Linear, inviscid models were the industry standard for this application. They had to be corrected by wind-tunnel or CFD data to cover transonic flow phenomena. Recently, high-fidelity aerodynamic models have been introduced which, in contrast to the previous methods, have an inherent quality to represent the important transonic flow phenomena for all flight conditions. However, the significant computational cost of these models restricts the computation of unsteady aerodynamics to a limited set of reference elastic modes. These unsteady aerodynamic reference results are subsequently mapped to all 'production' flutter computations with a least-squares method. This thesis report presents an investigation on the possibility of accuracy or robustness improvements in the implementation of this new, high-fidelity direct-CFD method in unsteady aeroelastic simulations. An error estimation study quantified the impact of approximation errors of the least-squares method on the frequency and damping curves of the 'production' computational case. Modal basis quality criteria are established and their performance is compared for a test case. In contrast to the proposed hypothesis, global mode assurance criteria are sufficient to predict the errors. Local or aerodynamically weighted quality criteria show similar performance and can therefore be considered redundant for the presented test case. In case of a non-satisfactory reference set, the modal basis can be enriched automatically and effectively in order to eliminate the approximation error. Additionally, a performance study of two reference selection methods on four computational test cases has been conducted. The application of the elastic modes of a nominal structural lay-out as reference is satisfactory for nominal structure flutter computations at different load distributions and for failure case simulations without strongly deviating mode shapes. However, this reference selection method can be insufficient regarding the approximation error for critical failure cases with strongly deviating mode shapes with respect to the nominal structure modes. Yet, for all test cases the error estimators are able to predict this approximation error, such that they can be eliminated by modal basis enrichment. On the other hand, a new method is proposed which uses the POD (Proper Orthogonal Decomposition) theory to decompose a wide range of modes for different failure and load cases into a reference set. This method performed satisfactory for all test cases, without any enrichment necessity. The prerequisite for a good performance of this reference selection method is a well-considered selection of the POD setup and the presence of the considered failure cases in the POD input.

Preface

This thesis considers improvements on the application of direct-CFD in high-fidelity unsteady aeroelastic simulations. The implementation of this new high-fidelity aerodynamic model introduced uncertainty in the mapping of the reference unsteady aerodynamic results to the considered flutter computations. The thesis study focuses on the error estimation of this mapping and improvements on the reference modal basis selection. This research topic was issued by the loads and aeroelastics department of Airbus Commercial Aircraft. The amazing opportunity to make use of Airbus' facilities and to work in close collaboration with the aeroelastic experts is something I will never forget.

The last nine months at Airbus have flown by. The challenging topic had me on the ropes multiple times and made me reconsider the original hypothesis three months in. The thesis results as they are presented today would never have been possible without the constant support of my colleagues and mentors. There are a couple persons I would like to thank in particular. Sander van Zuijlen, my thesis supervisor, for giving me the chance to work under your supervision. I appreciated your valuable feedback during our meetings and the improvements you brought into this thesis. Hans Bleecke, my supervisor and mentor at Airbus, your unwavering support pushed me through those times when all direction seemed lost. Reik Thormann and Bernd Stickan, I am grateful for everything you both taught me on aeroelastics and thesis writing.

Next to the professional support, my thesis work would not have been possible without my family and friends. I would like to take a moment to thank those who are closest to me. First and foremost, my parents, I might not always say it out loud, but your interest, support and love touches my heart. My sisters, Eva and Julie, for sticking up with me and making home feel home. Moemoe and Vava for creating that one place on Earth where time stands still and happiness is simple. You are my role models. Oma, you might no longer be by my side, but I hope that you are proud of what I have become. Last but not least, I would like to thank two wonderful ladies who made my time in Bremen also worthwhile when the books were closed. Amina and Bilge, I have never lived with two more clever, beautiful and funny girls. You made me explore and fall in love with Bremen in all its beauties, thank you.

H. Verdonck
Bremen, February 2019

Contents

List of Figures

List of Tables

Nomenclature

Greek symbols

β	Coefficient radial basis function	-
γ	Specific heat ratio	-
δ	Non-dimensional damping	-
$\boldsymbol{\epsilon}$	Least-squares residual matrix	-
η	Small numerical value	-
$\boldsymbol{\phi}$	Eigenvector	-
$\boldsymbol{\Phi}$	Eigenvector matrix	-
ϕ	Radial basis function	-
κ	Thermal conductivity	W/(mK)
λ	Eigenvalues POD method	-
μ_t	Dynamic eddy viscosity	kg/(ms)
ν	Kinematic viscosity coefficient	m^2/s
ω	Circular frequency	rad/s
Ω	Finite volume	-
Ψ	Least-squares participation factors	-
ρ	Density	kg/m^3
σ	Damping in Laplace variable	rad/s
τ_{ij}	Viscous shear stress tensor	$kg/(ms^2)$

Roman symbols

$\mathbf{A}$	Generalized air force matrix	-
a_x	Aircraft acceleration	m/s^2
b	Airfoil half-chord	m
c_p	Specific heat	J/K
$C_{L_{\text{Target}}}$	Target lift coefficient	-
C_{m_y}	Pitch coefficient	-
d^g	Distance from mesh deformation group	m
$\mathbf{D}$	Damping matrix	-
$\mathbf{D}^*$	Generalized damping matrix	-
$\mathbf{D}_{gyro}$	Gyroscopic damping matrix	-
$\mathbf{D}_{struc}$	Structural damping matrix	-
E	Young's modulus	Pa
EI	Flexural rigidity	Nm^2
$f_{v1}, c_{b1}, \sigma, c_{b2}, c_{w1}$	S-A turbulence model constants	-
$\mathbf{f}_a$	Aerodynamic force vector	N
$\mathbf{F}$	Determinant aeroelastic equation	-
$\mathbf{F}_a$	Aerodynamic force matrix	N
$\mathbf{f}_g$	Gravitational force vector	N
G	Shear modulus	Pa
GJ	Torsional rigidity	Nm^2
h	Altitude	m
H	Total enthalpy	J
$\mathbf{I}$	Identity matrix	-
I	Moment of inertia	m^4
J	Polar moment of inertia	m^4
k	Reduced frequency = Non-dimensional frequency	-
k^*	Turbulent kinetic energy	J
$\mathbf{K}$	Stiffness matrix	-
$\mathbf{K}^*$	Generalized stiffness matrix	-
$\mathbf{M}$	Mass matrix	-
$\mathbf{M}^*$	Generalized mass matrix	-
M_∞	Upstream Mach number	-
p	Laplace variable	rad/s
p	Pressure	Pa
Pr	Prandtl number	-
$\mathbf{q}$	Modal displacement coordinates	-
q_j	Heat flux	kg/s^3
$\mathbf{R}$	Residual vector	-
Re	Reynolds number	-
S	Sutherland's temperature	K
$\mathbf{S}_i$	Function values structural grid	-
S_{ij}^*	Mean shear rate	-
t	Time	s
T	Temperature	K
u	Velocity component in x-direction	m/s
U	Total internal energy	J
U_∞	Flight velocity	m/s
U^e	Finite element strain energy	J
v	Velocity component in y-direction	m/s
w	Velocity component in z-direction	m/s
$\mathbf{W}, \mathbf{E}, \mathbf{F}, \mathbf{G}$	Vectors of fluid unknowns	-
W^e	Finite element work	J
$\mathbf{x}$	Vector of structural node displacements	m
$\mathbf{X}$	Input matrix POD method	-

Mathematical notation

q	Scalar
$\mathbf{q}$	Vector
$\mathbf{Q}$	Matrix
$[\bar{\cdot}]$	Time-invariant mean
$[\tilde{\cdot}]$	Favre-averaged mean
$[\hat{\cdot}]$	Fourier coefficient
$[\dot{\cdot}]$	1st time derivative
$[\ddot{\cdot}]$	2nd time derivative
$[\circ]$	Element-wise matrix product

Abbreviations

ALE	Arbitrary Lagrangian Eulerian
CFD	Computational Fluid Dynamics
CSM	Computational Structural Mechanics
DGT	Dynamic Ground Test
DLM	Doublet-Lattice Method
DNS	Direct Numerical Simulation
EVM	Eddy Viscosity Model
FC	Failure Case
FEM	Finite Element Method
FS	Front Spar
FVT	Flight Vibration Test
GAF	Generalized Air Force Matrix
GVT	Ground Vibration Test
HTP	Horizontal Tail Plane
IB	Inboard
LCO	Limit-Cycle Oscillations
LFD	Linearized Frequency Domain
LSQ	Least-Squares
MAC	Mode Assurance Criterion
OB	Outboard
POD	Proper Orthogonal Decomposition
RANS	Reynolds Averaged Navier-Stokes
RBF	Radial Basis Function
RFW	Radius Full Weight
RS	Rear Spar
RZW	Radius Zero Weight
TE	Trailing Edge
VCAS	Velocity - Calibrated Airspeed
VEAS	Velocity - Equivalent Airspeed
VTP	Vertical Tail Plane

1

Thesis Outline

1.1. Background of aeroelasticity and flutter prediction

Aeroelasticity is the coupling between aerodynamic, elastic and inertial forces. In 1947, A.R. Collar was one of the first to publish a comprehensive description on aeroelastic theory. He defined the problem as ”the study of the mutual interaction that takes place within the triangle of the inertial, elastic, and aerodynamic forces acting on structural members exposed to an airstream, and the influence of this study on design.” [12] Figure 1.1 visualizes this interaction triangle which became named after him.

As illustrated in this triangle, different fields can be specified within the aeroelasticity concept. The inertial forces can be neglected when the time scales are large, this is denoted as static aeroelasticity. On the other hand, coupling between only the inertial and aerodynamic forces is considered when the structure is defined to be rigid. This is the field of flight dynamics. In a standstill scenario, the aerodynamic forces are not available. The interaction of the remaining inertial and elastic forces is the field of structural dynamics. Finally, the interaction of all three components results in dynamic aeroelasticity, the subject of this thesis study.

The need for a proper understanding of these phenomena was illustrated by a range of tragic events in aviation history. The effect of aeroelasticity is as old as heavier-than-air flight itself. Aeroelasticity might have even been decisive in the race to the first flight. Attempts by S. Langley in his monoplane aircraft failed due to torsional divergence, a static aeroelastic effect. The Wright brothers noticed that these monoplane wings lacked torsional rigidity. This understanding made them write their names in the history books by achieving the first heavier-than-air flight in their Wright’s flyer biplane. In the following decades, the flight speed of the developed aircraft increased, and so did the possibility of flutter occurrences. The first recorded flutter incident was the crash of the Handley Page O/400 bomber.

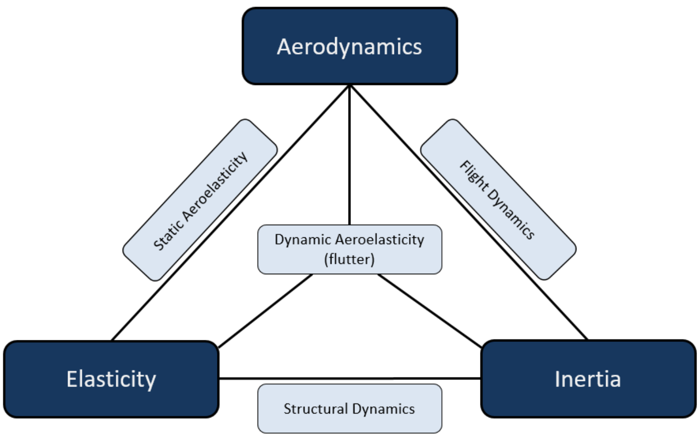

Figure 1.1: Collar Triangle [12]

This aircraft experienced strong antisymmetric rear fuselage and tail oscillations caused by the independently connected elevator panels. These events formed only the onset of aeroelasticity related crashes, multiple events were to follow in the subsequent years. The need for aeroelastic understanding and prediction was triggered and aeroelastic research developed into a wide and active field in the aeronautical industry. [14]
The strong connection between aeroelasticity and the aeronautical world is no coincidence. For optimal performance, aerospace structures require low weight and a slender aerodynamic design. This results in flexible structures which are relatively heavily loaded, making them utmost susceptible for coupling between the aeroelastic forces defined by Collar. Different aeroelastic phenomena are observed in aircraft design. The three most well-known effects are divergence, control effectiveness and flutter. Divergence and control effectiveness are static effects which were seen on early aircraft. However their influence on design is becoming less prominent in recent years. Flutter, however, is a dynamic instability which emerges when a structural mode absorbs net energy from the airflow within one vibrational period. Classical flutter is the result of a coupling of two or more structural modes, yet flutter can also originate due to the coupling of only one structural mode with unsteady flow phenomena such as shocks or lag effects. Flutter is still a main subject in unsteady aeroelastic research and is often the main point of concern in the aeroelastic design and certification of commercial aircraft. Aircraft manufacturers have to prove that their aircraft are flutter free within the flight envelope plus a safety margin. They have to show validated calculations for all mass distributions, taking into account the overweight that could be added by repair, repainting, water ingress or production scatter. On top of that, they have to show that no flutter will appear in the event of a wide range of structural failure cases during operation.

1.2. Research motivation and objective

Modeling dynamic aeroelastic effects requires a theoretical model for each of the three disciplines defined by Collar. The main driver for this research project are recent developments in the aerodynamic modeling and its implementation in the unsteady aeroelastic simulation procedures. At Airbus, unsteady aerodynamics are modeled with a linear, inviscid DLM model, corrected with CFD or wind-tunnel data for transonic effects. DLM models were the industry standard for the unsteady aerodynamics in the aeroelastic context [27]. The most recent development is the gradual replacement of this low-fidelity model with a high-fidelity direct LFD model [36]. The theoretical background of this new model will be elaborated in detail later in this report, but the main benefit for the aeroelastic simulation will be a flow description which captures most of the physically complex flow phenomena. The two most significant improvements are: 1) The effects of shocks and viscosity are inherently available, important for the modeling of the transonic flight regime, 2) The LFD computational domain has a denser spatial mesh, which will give a more detailed view on the flow phenomena. A comparison between the computational mesh for the DLM method and the LFD method is shown in Figure 1.2.

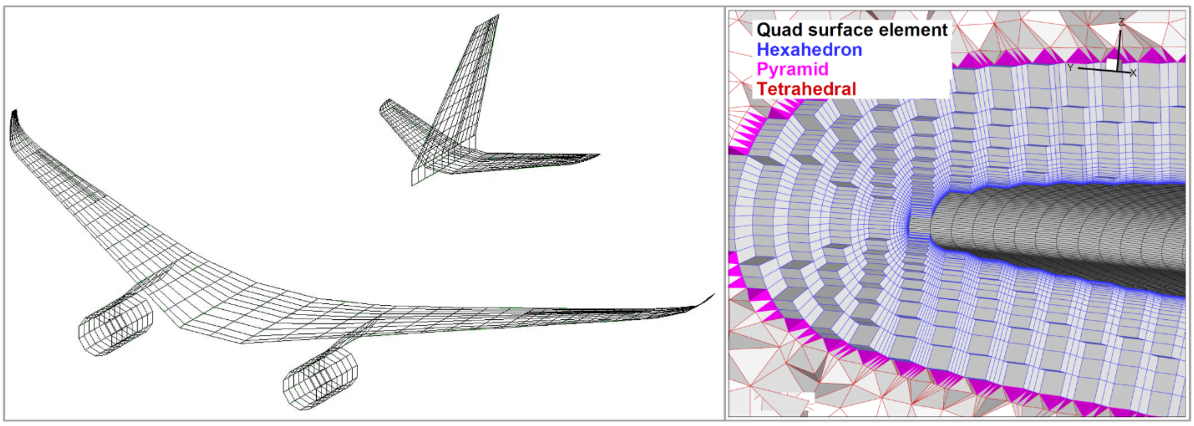

Figure 1.2: Comparison of computational grid between DLM (left) and LFD (right). (DLM figure property of Airbus GmbH/LFD figure obtained from [32])

Introducing this new method in the unsteady aeroelastic simulation procedures has induced some uncertainty in the interaction with the other models. The assumption is made that - in the new setup - the aerodynamics are no longer the restrictive element for capturing the aeroelastic physics. Rather, this more detailed and high-fidelity modeling of the aerodynamics opens up the question if the available fidelity of the dynamic structural model is high enough to match the improved accuracy as a whole. Implementing a new method can also lead to new or unknown uncertainties in the procedure. Given the recent introduction of the LFD model, the possibility for optimization of its implementation can definitely be expected. These motives can be formalized in following research objective.

Research objective:
Investigate the possibility of accuracy or robustness improvements in the implementation of high-fidelity direct-CFD methods in unsteady aeroelastic simulations.

The first research topic was an investigation on the impact of dynamic model imperfections in combination with the new high-fidelity, spatially refined aerodynamic model. However, a sensitivity study on dynamic model variations showed that the expected benefits in the unsteady aeroelastic modeling for dynamic model improvements are small. The necessity for further investigations on this topic are therefore deemed out of the scope of this thesis. The setup and results of the structural sensitivity study are documented in Appendix A.
Instead, this thesis report will focus on a second topic which is a direct result of the practical implementation of the new LFD method. In practice, flutter computations have to be made for a large number of parameter combinations depending on the flight conditions, structural lay-out and mass distribution of the aircraft. However, the direct LFD method can only be computed for a subset of the full computational space, due to its relatively high computational cost. The unsteady aerodynamics are therefore only calculated for a small number of elastic mode shapes. These aerodynamic results are then mapped to the other considered cases using a least-squares approximation based on the respective structural mode shapes. The selection of the reference case is currently done through engineering judgment and the effect of the approximation errors introduced by the least-squares method are not well understood. Especially in case of structural failure cases this could lead to bad mode approximations and correspondingly introduce errors in the frequency and damping curves. In this respect the research question to be answered reads:

Research Question:
How can the selection of an aerodynamic reference modal basis be made more robust and accurate for usage of direct-CFD methods in unsteady aeroelastic simulations?

This question is divided in two subquestions.

Research Question 1:
Can the error introduced in the frequency and damping curves caused by the approximation error of the direct-CFD method be quantified by error estimation?

Research Question 2:
What is the best method for the reference modal basis selection for usage in direct-CFD methods in unsteady aeroelastic simulations?

1.3. Methodology and report overview

This section describes the proposed research methodology to answer the presented research questions. Correspondingly, an overview of the report lay-out will be elaborated.

1.3.1. Theoretical background

Chapter 2 describes the required theoretical background for all presented study topics. Introductions will be given into the dynamic structural modeling, aerodynamic modeling, aeroelastic coupling and flutter prediction methods. For each of these disciplines a discussion of the theoretical principles will be given as well as an elaboration on the applied tools and processes in the thesis project. Finally, a detailed overview will explain the interaction of all sub-models to form the unsteady aeroelastic simulation process. Additional to this discussion of the aeroelastic simulation process, the theory of the Proper Orthogonal Decomposition (POD) method will be introduced. This modal reduction method will be applied multiple times in the error estimation and reference modal basis selection studies.

1.3.2. Error estimation of the reference modal basis selection

Chapter 3 describes the study on the error estimation of the least-squares approximation error on the frequency and damping curves. Given the large computational space for flutter computations, the new LFD unsteady aerodynamic method can only be executed for a limited number of structural mode shapes to keep the computational time within reasonable bounds. The corresponding results of the reference modal basis are mapped to the considered 'production' flutter computation based on the respective shapes of the 'production' modes and the reference modes. The impact of the reference case selection on the frequency and damping curves will be tested. Different criteria which should identify the quality of a given reference set for a specific considered 'production' computation will be established. These quality criteria are based on the mode approximation errors, possibly weighted with the reference aerodynamics to identify areas which have a bigger impact on the flutter curves. A best-practice threshold for the quality criteria will be defined which could be implemented in the practical flutter simulation procedure.

1.3.3. POD-based reference modal basis selection

A possible improvement for the implementation of the direct LFD method could be a better, more automated selection of the reference case. Two methods of reference modal basis selection will be compared in Chapter 4. The first one uses a set of physical modes corresponding to a single structural lay-out and mass distribution. The second reference set will be made by applying a proper orthogonal decomposition (POD) method on a large set of structural lay-out and load cases. The results of both methods will be compared for four test cases for which the direct aerodynamics are available. This study will also form a test subject to verify the quality criteria obtained in the error estimation study.

To complete the report, Chapter 5 will summarize the conclusions of the presented studies and give an outlook on future investigations which could be executed on this topic.

2 Theory

As complex as it is to predict dynamic aeroelastic behavior, so simple seems the mathematical description of the problem. The whole unsteady aeroelastic representation of an aircraft for a given flight condition can be described by the second order, linear, ordinary differential equation:

$$\mathbf{M}\ddot{\mathbf{x}} + \mathbf{D}\dot{\mathbf{x}} + \mathbf{K}\mathbf{x} = \mathbf{f}_a(t, \mathbf{x}, \dot{\mathbf{x}}) - \mathbf{f}_g. \tag{2.1}$$

The left hand side is the governing equation for mechanical vibrations, with the mass matrix $\mathbf{M}$, the damping matrix $\mathbf{D}$, the stiffness matrix $\mathbf{K}$ and the vector of structural node displacements $\mathbf{x}$. The matrix inputs for this left hand side will be provided by the dynamic structural model. The right hand side is the difference between the aerodynamic force vector $\mathbf{f}_a$ and the gravitational force vector $\mathbf{f}_g$. The aerodynamic forces are a function of time t, the position $\mathbf{x}$ and motion $\dot{\mathbf{x}}$ of the structure and the flight conditions (Mach number M_∞, altitude h,...). The goal of flutter analysis is to assess the stability of the dynamic structure with respect to small perturbations, i.e. do perturbations of the system grow or decay in amplitude? Flutter analysis can therefore be restricted to a linear stability problem and correspondingly the solution is assumed to be a damped harmonic oscillation:

$$\mathbf{x}(t) = \hat{\mathbf{x}}e^{pt}, \tag{2.2}$$

with the Laplace variable p denoted as:

$$p = \frac{b}{U_\infty}(\sigma + i\omega) = \delta + ik, \tag{2.3}$$

where σ and ω represent the damping and circular frequency, respectively. These parameters are non-dimensionalized to δ and k by the airfoil half-chord b and the flight velocity U_∞. This gives the new governing equation in the frequency domain:

$$\left[\frac{U_\infty^2}{b^2}p^2\mathbf{M} + \frac{U_\infty}{b}p\mathbf{D} + \mathbf{K}\right]\hat{\mathbf{x}} = \frac{1}{2}\rho U_\infty^2 \mathbf{F}_a(p, M_\infty)\hat{\mathbf{x}}, \tag{2.4}$$

with the aerodynamic force matrix $\mathbf{F}_a$ dependent on the Laplace variable p and the flight conditions.

This chapter will present the theory and applied software tools for all sub-models required to solve the dynamic aeroelastic equation. At the end of the chapter an overview of the state-of-the-art unsteady aeroelastic simulation process applied in the research project will be given. Finally, also the proper orthogonal decomposition of vector spaces, which will prove to be an important method later in this thesis, will be introduced.

2.1. Dynamic structural model

The left hand side of the dynamic aeroelastic equation is modeled by a finite element model. This method has been the dominating instrument for structural modeling in almost all engineering disciplines. It provides the opportunity to model complex structures for which analytical solutions are no

longer a feasible alternative. As the name suggests, the finite element model discretizes the structural continuum in a set of geometrically simple finite elements (beams, plates, shells, etc.), for which elasticity and strain-displacement matrices can be easily established.
The finite element method is based on the equilibrium of all finite elements in its mesh. This equilibrium is enforced by applying the principle of virtual work, which states that for a body or element in equilibrium the external virtual work applied to the body through a small virtual displacement is equal to the internal virtual work,

$$\delta U^e - \delta W^e = 0, \tag{2.5}$$

where δU^e is the virtual strain energy and δW^e the virtual work exerted by body forces, surface force or concentrated loads. The element stiffness and mass matrices can be derived by this relation with the known element density, elasticity, and strain-displacement matrices. The global stiffness $\mathbf{K}$, mass $\mathbf{M}$ and damping $\mathbf{D}$ matrices can then be defined by assembling all element matrices. A detailed derivation and discussion of finite element procedures is given by Bathe [5].

2.1.1. Modal analysis

The dynamic characteristics of a structural system are defined through a modal analysis which describes the response of the structure to free vibrations. In this case, both the damping $\mathbf{D}$ and the external forces are assumed to be zero. This reduces initial equation 2.1 to

$$\mathbf{M}\ddot{\mathbf{x}} + \mathbf{K}\mathbf{x} = 0. \tag{2.6}$$

Assuming the purely harmonic solution to be of the form $\mathbf{x}(t) = \boldsymbol{\phi} e^{i\omega t}$ and rearranging gives the eigenvalue problem

$$\left(\mathbf{K} - \omega^2 \mathbf{M}\right) \boldsymbol{\phi} = 0, \tag{2.7}$$

which can be solved for the eigenvalues ω and the eigenvectors $\boldsymbol{\phi}$.

2.1.2. Generalized coordinates

The finite element nodal points form the unknowns in governing equation 2.4. Converting these unknowns to generalized coordinates, defined by the mode shapes of the structure, will reduce the computational cost and give a physical meaning to the unknown displacements. The order of the problem is reduced from the total number of degrees of freedom in the finite element mesh to the number of elastic modes considered for the flutter computation. The transformation between element nodal coordinates $\mathbf{x}$ and modal coordinates $\mathbf{q}$ is given by

$$\hat{\mathbf{x}} = \boldsymbol{\Phi}\hat{\mathbf{q}}, \tag{2.8}$$

with $\boldsymbol{\Phi}$ the eigenvector matrix assembled out of all considered eigenvectors $\boldsymbol{\phi}$ of the modal analysis. Introducing this transformation in equation 2.4 and projecting with $\boldsymbol{\Phi}^T$ gives

$$\left[\frac{U_\infty^2}{b^2} p^2 \boldsymbol{\Phi}^T \mathbf{M} \boldsymbol{\Phi} + \frac{U_\infty}{b} p \boldsymbol{\Phi}^T \mathbf{D} \boldsymbol{\Phi} + \boldsymbol{\Phi}^T \mathbf{K} \boldsymbol{\Phi}\right] \hat{\mathbf{q}} = \frac{1}{2} \rho U_\infty^2 \boldsymbol{\Phi}^T \mathbf{F}_a(p, M_\infty) \boldsymbol{\Phi} \hat{\mathbf{q}}, \tag{2.9}$$

which can be simplified to

$$\left[\frac{U_\infty^2}{b^2} p^2 \mathbf{M}^* + \frac{U_\infty}{b} p \mathbf{D}^* + \mathbf{K}^*\right] \hat{\mathbf{q}} = \frac{1}{2} \rho U_\infty^2 \mathbf{A}(p, M_\infty) \hat{\mathbf{q}}, \tag{2.10}$$

with $\mathbf{M}^*$, $\mathbf{D}^*$, and $\mathbf{K}^*$ denoted as the generalized mass, damping and stiffness matrix, respectively. In aeroelastic applications, matrix $\mathbf{A}(p, M_\infty)$ is known as the Generalized Air Force (GAF) matrix.
The eigenvector matrix $\boldsymbol{\Phi}$ is orthogonal with respect to $\mathbf{M}$ and $\mathbf{K}$, which makes that both $\mathbf{M}^*$ and $\mathbf{K}^*$ are diagonal matrices. Moreover, $\boldsymbol{\Phi}$ can be normalized by an arbitrary factor. Typically, it is mass normalized such that

$$\boldsymbol{\phi}^T \mathbf{M} \boldsymbol{\phi} = \mathbf{M}^* = \mathbf{I}, \tag{2.11}$$

where $\mathbf{I}$ is the identity matrix and correspondingly

$$\mathbf{\Phi}^T \mathbf{K} \mathbf{\Phi} = \mathbf{K}^* = \text{diag}(\boldsymbol{\omega}^2). \tag{2.12}$$

The eigenvector matrix $\mathbf{\Phi}$ is not orthogonal to $\mathbf{D}$, so $\mathbf{D}^*$ is not necessarily diagonal. However, because $\mathbf{D}$ is difficult to compute, in practice $\mathbf{D}^*$ is usually defined as a diagonal matrix with experimentally found damping values.

2.1.3. Tool environment thesis project

MSC-NASTRAN, one of the most common structural solvers in the aerospace industry, is used to produce and solve the finite element model [30]. The structural eigenmodes and frequencies are computed and the generalized mass and stiffness matrices are forwarded to the flutter solver. The gyroscopic damping term is also obtained from Nastran. The structural damping matrix, however, is derived from a Ground Vibration Test (GVT). The specific model used for this thesis project is a realistic aircraft model consisting out of approximately 125,000 structural elements.

Note that the linear solution algorithm of NASTRAN will be used. This assumes that the mass, stiffness and damping matrices are constant with respect to the displacement and motion of the structure. It is reasonable to use linear structural models under the assumptions that the materials are linearly elastic, the deformations are small and the boundary conditions constant. These are reasonable assumptions for general unsteady and steady aeroelastic simulations and it has been shown that linear structural models suffice to model flutter calculations for conventional aircraft. However, small differences in the results were observed for very flexible wings comparing linear and non-linear structural models [34].

2.2. Aerodynamic model

For the certification analysis of commercial aircraft, the aerodynamic model has to cope with a difficult combination of physical and practical requirements. Most commercial aircraft operate in the transonic regime. Typical cruise conditions range between Mach 0.8 and 0.9. In these flight conditions a mix of subsonic and supersonic flow characteristics result in non-linear flow behavior such as supersonic flow regions, shock waves and shock-boundary interaction. One of the main difficulties is shock movement which causes a non-linear time-lag of the aerodynamic forces on the structural oscillations. This phenomenon results in a strong reduction of the critical flutter speed, which is denoted as the transonic dip, as shown in Figure 2.1. This figure illustrates that the phenomena in the transonic regime can only be accurately modeled with non-linear, viscous aerodynamic models.

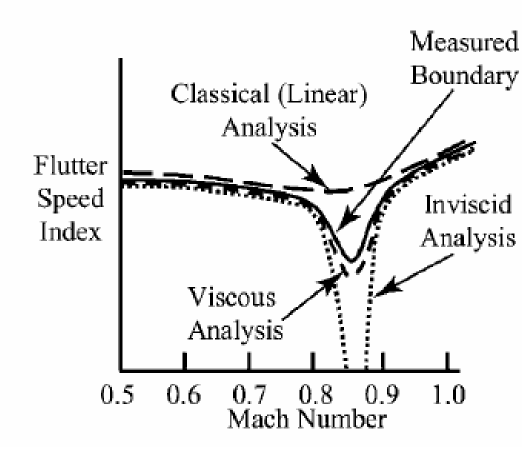

Figure 2.1: Transonic Dip [27]

Classical methods based on the subsonic small disturbance theory, such as the doublet-lattice method, completely miss the transonic dip phenomenon. In the sub- and supersonic flight regimes, however, these methods will give accurate results. Non-linear, but inviscid models are often overconservative in the transonic regime. They predict a flutter speed much lower than reality. This is because neglecting viscous effects results in predictions of the shock positions too much downstream, increasing the aerodynamic coupling of torsion and bending motions. Moreover, the flutter speed increase at the

end of the transonic dip is caused by shock-induced separation when viscous effects are considered. However, for inviscid computations, this effect is caused by the shock reaching the trailing edge [27].
Non-linear, viscous aerodynamic models are standard engineering tools. However, the practical application of flutter computations in aeronautical design introduces one major difficulty. Flutter computations span traditionally a large parameter space of aerodynamic and structural parameters. The unsteady airloads have to be computed for a wide range of elastic mode shapes for each considered load case scenario as a function of the flight condition and reduced frequency k. As a conclusion, the aerodynamic model has to be capable to both capture the complex physics of the transonic flow regime and to retain a low computational cost. These requirements are difficult to fulfill simultaneously.
For the last decades, the computational cost constraint had the consequence that only linear, inviscid aerodynamic models (such as DLM) were practically feasible for this type of calculations [1, 27]. The prediction of these models then had to be enhanced with correction factors from CFD or wind-tunnel experiments in order to make them also suitable in the transonic regime. Recent developments have shown that there are models which can retain the fidelity of viscous, non-linear CFD models and are computationally cheap enough to make them feasible for this usage. For this thesis a high-fidelity LFD (linear frequency domain) method will be applied to solve the fluid equations. This method retains RANS-like fidelity while being only a fraction of the computational cost of conventional unsteady RANS simulations [20, 36]. This section will give a full overview of this aerodynamic model, starting with the introduction of the Reynolds-Averaged Navier-Stokes (RANS) equations, followed by a discussion of the required spatial finite volume discretization and the linear frequency domain solution method.

2.2.1. Navier-Stokes equations

The Navier-Stokes equations describe the motion of viscous, compressible fluid flow. This set of equations will thus give an accurate representation of the flow behavior, even in the transonic flight regime. The fluid motion is described by establishing equations for mass continuity, momentum and energy conservation. Respectively, these three equations are given in 3-dimensional, conservative form using Einstein notation:

$$\frac{\partial \rho}{\partial t} + \frac{\partial(\rho u_j)}{\partial x_j} = 0, \tag{2.13}$$

$$\frac{\partial(\rho u_i)}{\partial t} + \frac{\partial(\rho u_i u_j)}{\partial x_j} = -\frac{\partial p}{\partial x_i} + \frac{\partial \tau_{ij}}{\partial x_j}, \tag{2.14}$$

$$\frac{\partial(\rho U)}{\partial t} + \frac{\partial(\rho E u_j)}{\partial x_j} = -\frac{\partial(p u_j)}{\partial x_j} + \frac{\partial(u_i \tau_{ij})}{\partial x_j} - \frac{\partial q_j}{\partial x_j}. \tag{2.15}$$

In this conservative form the body forces are neglected. The local velocity components in Cartesian coordinates are represented by u_i. The other variables in the N-S equations are the fluid density ρ, pressure p, heat flux q_j, total internal energy U and the viscous shear stress tensor τ_{ij}. Applying the assumption of a Newtonian fluid and Stokes' hypothesis, τ_{ij} can be defined as a function of the velocity components and the viscosity coefficient μ of the fluid as

$$\tau_{ij} = \mu\left(\frac{\partial u_i}{\partial x_j} + \frac{\partial u_j}{\partial x_i}\right) - \frac{2\mu}{3}\frac{\partial u_k}{\partial x_k}\delta_{ij}. \tag{2.16}$$

This dynamic viscosity coefficient μ can be defined as a function of temperature T by Sutherland's law

$$\mu = \mu_{ref}\left(\frac{T}{T_{ref}}\right)^{3/2}\frac{T_{ref} + S}{T + S}, \tag{2.17}$$

where S is Sutherland's temperature, a gas constant (110.4 K for air). T_{ref} and μ_{ref} are known reference temperature and viscosity conditions. The heat flux vector q_j can be expressed by Fourier's law

$$q_j = -\kappa\frac{\partial T}{\partial x_j}, \tag{2.18}$$

where κ is the thermal conductivity of the fluid. This flow property can be derived from the specific heat variable c_p, dynamic viscosity μ and Prandtl number Pr as

$$\kappa = -\frac{c_p \mu}{\mathrm{Pr}}. \tag{2.19}$$

Assuming a perfect gas, the equation of state is used to define a relation between the pressure and total internal energy:

$$p = (\gamma - 1)\rho\left(U - \frac{u_i u_i}{2}\right), \tag{2.20}$$

with γ the specific heat ratio, a gas constant. As means of simplification, the total enthalpy can be introduced into the energy equation

$$H = U + \frac{p}{\rho}. \tag{2.21}$$

Inserting this in equation 2.15 and rewriting the equations to contain one term with the time derivatives and one term with the divergence of the flux tensors gives a simplified version of the Navier-Stokes equations as

$$\frac{\partial \rho}{\partial t} + \frac{\partial(\rho u_j)}{\partial x_j} = 0, \tag{2.22}$$

$$\frac{\partial(\rho u_i)}{\partial t} + \frac{\partial}{\partial x_j}(\rho u_i u_j + p\delta_{ij} - \tau_{ij}) = 0, \tag{2.23}$$

$$\frac{\partial(\rho U)}{\partial t} + \frac{\partial}{\partial x_j}\left(\rho H u_j + q_j - u_i \tau_{ij}\right) = 0. \tag{2.24}$$

These simplified equations can also be given in vector form, where the Einstein notation has been replaced by the conventional Cartesian formulation.

$$\frac{\partial \mathbf{W}}{\partial t} + \frac{\partial \mathbf{E}}{\partial x} + \frac{\partial \mathbf{F}}{\partial y} + \frac{\partial \mathbf{G}}{\partial z} = 0, \tag{2.25}$$

with,

$$\mathbf{W} = \begin{pmatrix} \rho \\ \rho u \\ \rho v \\ \rho w \\ \rho U \end{pmatrix} \tag{2.26}$$

$$\mathbf{E} = \begin{pmatrix} \rho u \\ \rho u^2 + p - \tau_{xx} \\ \rho u v - \tau_{xy} \\ \rho u w - \tau_{xz} \\ \rho H u - u\tau_{xx} - v\tau_{xy} - w\tau_{xz} + q_x \end{pmatrix} \tag{2.27}$$

$$\mathbf{F} = \begin{pmatrix} \rho v \\ \rho u v - \tau_{xy} \\ \rho v^2 + p - \tau_{yy} \\ \rho v w - \tau_{yz} \\ \rho H v - u\tau_{xy} - v\tau_{yy} - w\tau_{yz} + q_y \end{pmatrix} \tag{2.28}$$

$$\mathbf{G} = \begin{pmatrix} \rho w \\ \rho u w - \tau_{xz} \\ \rho v w - \tau_{yz} \\ \rho w^2 + p - \tau_{yz} \\ \rho H w - u\tau_{xz} - v\tau_{yz} - w\tau_{zz} + q_z \end{pmatrix} \tag{2.29}$$

Equation 2.25, together with the constitutive equations 2.16 and 2.18 and the thermodynamic relationship in equation 2.20 gives a closed set of equations for viscous compressible fluid motion. This set of equations can be solved numerically by means of a Direct Numerical Simulation (DNS). This would mean that the whole range of spatial and temporal turbulence scales have to be resolved, which makes the computational cost of DNS proportional to Re^3. As a result, the DNS solution of the Navier-Stokes equation can only be effectively applied to scientific problems with a simple flow description and at low Reynolds numbers. For engineering applications the computational cost is too excessive, which induces the need for approximate solution alternatives of the Navier-Stokes equation. The most common approximation method is Reynolds averaging which will be discussed in the upcoming section.

2.2.2. Reynolds averaging

The Reynolds Averaged Navier-Stokes (RANS) equations decompose the flow in a mean component superimposed with flow fluctuations (turbulence). This turbulence has to be defined as function of the mean flow characteristics, which is done with so-called turbulence models to close the RANS equations. Conventional Reynolds-averaging is done through Reynolds decomposition of the flow parameters in a time-averaged and a fluctuating part

$$Q = \bar{Q} + Q'', \tag{2.30}$$

where Q is an arbitrary parameter for which the time-averaged component $\bar{Q}$ is defined as

$$\bar{Q} = \lim_{\Delta t \to \infty} \frac{1}{\Delta t} \int_{t_1}^{t_1+\Delta t} Q dt. \tag{2.31}$$

In compressible flows the density also has to be decomposed in a mean and turbulent part. In order to simplify the equations, Favre-averaging is applied to some parameters (u, v, w and H), which adds mass-weighted averaging to the conventional averaging. This is done by taking the time average of the multiplication of the variable with the density, followed by a division of the average density

$$\tilde{Q} = \frac{\overline{\rho Q}}{\bar{\rho}} = \frac{1}{\bar{\rho}} \lim_{\Delta t \to \infty} \frac{1}{\Delta t} \int_{t_1}^{t_1+\Delta t} \rho Q dt, \tag{2.32}$$

$$Q = \tilde{Q} + Q'. \tag{2.33}$$

Note that averages of the fluctuations obtained by conventional Reynolds averaging are zero ($\overline{Q''} = 0$) and that the average of fluctuations of the Favre-averaging multiplied with the density are zero ($\overline{\rho Q'} = 0$). Introducing the conventional and Favre-averaging into the Navier-Stokes equations and simplifying gives following results for the state vectors:

$$\frac{\partial \bar{\mathbf{W}}}{\partial t} + \frac{\partial \bar{\mathbf{E}}}{\partial x} + \frac{\partial \bar{\mathbf{F}}}{\partial y} + \frac{\partial \bar{\mathbf{G}}}{\partial z} = 0, \tag{2.34}$$

with,

$$\bar{\mathbf{W}} = \begin{pmatrix} \bar{\rho} \\ \bar{\rho}\tilde{u} \\ \bar{\rho}\tilde{v} \\ \bar{\rho}\tilde{w} \\ \bar{\rho}\tilde{U} \end{pmatrix} \tag{2.35}$$

$$\bar{\mathbf{E}} = \begin{pmatrix} \bar{\rho}\tilde{u} \\ \bar{\rho}\tilde{u}^2 + \bar{p} - \bar{\tau}_{xx} + \overline{\rho u'^2} \\ \bar{\rho}\tilde{u}\tilde{v} - \bar{\tau}_{xy} + \overline{\rho u'v'} \\ \bar{\rho}\tilde{u}\tilde{w} - \bar{\tau}_{xz} + \overline{\rho u'w'} \\ \bar{\rho}\tilde{H}\tilde{u} - \tilde{u}\bar{\tau}_{xx} - \tilde{v}\bar{\tau}_{xy} - \tilde{w}\bar{\tau}_{xz} + \bar{q}_x + \frac{\partial \overline{\rho H'u'}}{\partial x} \end{pmatrix} \tag{2.36}$$

$$\bar{\mathbf{F}} = \begin{pmatrix} \bar{\rho}\tilde{v} \\ \bar{\rho}\tilde{v}\tilde{u} - \bar{\tau}_{yx} + \overline{\rho v'u'} \\ \bar{\rho}\tilde{v}^2 + \bar{p} - \bar{\tau}_{yy} + \overline{\rho v'^2} \\ \bar{\rho}\tilde{v}\tilde{w} - \bar{\tau}_{yz} + \overline{\rho v'w'} \\ \bar{\rho}\tilde{H}\tilde{v} - \tilde{u}\bar{\tau}_{xy} - \tilde{v}\bar{\tau}_{yy} - \tilde{w}\bar{\tau}_{yz} + \bar{q}_y + \frac{\partial\overline{\rho H'v'}}{\partial y} \end{pmatrix} \tag{2.37}$$

$$\bar{\mathbf{G}} = \begin{pmatrix} \bar{\rho}\tilde{w} \\ \bar{\rho}\tilde{w}\tilde{u} - \bar{\tau}_{zx} + \overline{\rho w'u'} \\ \bar{\rho}\tilde{w}\tilde{v} - \bar{\tau}_{zy} + \overline{\rho w'v'} \\ \bar{\rho}\tilde{w}^2 + \bar{p} - \bar{\tau}_{zz} + \overline{\rho w'^2} \\ \bar{\rho}\tilde{H}\tilde{w} - \tilde{u}\bar{\tau}_{xz} - \tilde{v}\bar{\tau}_{yz} - \tilde{w}\bar{\tau}_{zz} + \bar{q}_z + \frac{\partial\overline{\rho H'w'}}{\partial z} \end{pmatrix} \tag{2.38}$$

The averaging has resulted in extra terms in the momentum equations and the energy equation. As a result the Navier-Stokes equations are no longer of a closed form. The extra term in the momentum equations is of the form $-\overline{\rho u_i' u_j'}$ and is called the Reynolds stress tensor, the extra term in the energy equation is of the form $-\overline{\rho H' u_i'}$. Additional expressions have to be found for these extra terms, which is known as turbulence modeling.

2.2.3. Turbulence modeling

Turbulence models give expressions for the additional terms in the RANS equations ($-\overline{\rho u_i' u_j'}$ and $-\overline{\rho H' u_i'}$) in order to get a closed form which can be solved numerically. Physicists have been looking for the perfect model for decades, but so far no overall superior turbulence model has emerged. They vary in accuracy, computational time, and most of them outperform others for a specific case, but perform worse when some flow characteristics change [11, 17]. For this thesis project the one-equation Spalart-Allmaras (S-A) turbulence model is used, which will be introduced here briefly for the modeling of the Reynolds stress tensor.

The S-A turbulence model is based on the Eddy Viscosity Model (EVM) approach. This uses the Boussinesq hypothesis which proposes that the Reynolds stress tensor is proportional to the mean shear rate S_{ij}^*, with the eddy viscosity μ_t as proportionality factor

$$-\overline{\rho u_i' u_j'} \cong 2\mu_t S_{ij}^* - \frac{2}{3}\delta_{ij}\bar{\rho}k^*, \tag{2.39}$$

with k^* being the turbulent kinetic energy and δ_{ij} the Kronecker delta. The mean shear rate can also be written as a function of velocity gradients as shown in equation 2.16. This gives the full equation for the Reynolds stress tensor:

$$-\overline{\rho u_i' u_j'} = \mu_t\left(\frac{\partial\tilde{u}_i}{\partial x_j} + \frac{\partial\tilde{u}_j}{\partial x_i} - \frac{2}{3}\delta_{ij}\frac{\partial\tilde{u}_k}{\partial x_k}\right) - \frac{2}{3}\delta_{ij}\bar{\rho}k^*. \tag{2.40}$$

The modeling problem has now been reduced to the eddy viscosity μ_t only, which is a scalar field quantity. Turbulence models try to express this eddy viscosity as a function of the mean velocity field. S-A is a one-equation model, meaning that it gives a description for the eddy viscosity by only one transport equation. The eddy viscosity μ_t is given as

$$\mu_t = \rho\tilde{\nu}f_{v1}, \tag{2.41}$$

with an empirically determined constant f_{v1} and the kinematic eddy viscosity $\tilde{\nu}$ computed by the transport equation:

$$\frac{D\tilde{\nu}}{Dt} = c_{b1}\tilde{S}\tilde{\nu} + \frac{1}{\sigma}\left[\nabla\cdot(\tilde{\nu}\nabla\tilde{\nu}) + c_{b2}(\nabla\tilde{\nu})^2\right] - c_{w1}f_w\left[\frac{\tilde{\nu}}{d}\right]^2. \tag{2.42}$$

The total derivative on the left-hand side represents convection and the terms on the right-hand side represent, respectively, turbulence production, diffusion and destruction. c_{b1}, σ, c_{b2} and c_{w1} are all

empirical constants. A full description of the parameters and constants is described by Spalart and Allmaras in [31].
The S-A turbulence model is originally established specifically for application in the aeronautical industry. It has superior computational qualities, since only one transport equation has to be solved, while giving good results for simple attached flows and for flow-separation prediction. This proves to be sufficient for most aeronautical applications and especially flutter simulations [10]. However, it lacks complexity to model flow reattachment and free shear layer flow phenomena [11, 17].

2.2.4. Finite volume discretization

So far the Navier-Stokes equations have been in continuous form for the complete formulation in equation 2.25 and in Reynolds averaged formulation in equation 2.34. A spatial discretization method has to be employed to solve these equations numerically. Finite volume methods are the standard spatial discretization procedure for the Navier-Stokes equations. They prescribe the conservation principles on small, discrete control volumes. The outflow of one cell becomes the inflow for the neighboring cell. A simple sketch of a structured 2D finite volume mesh is shown in Figure 2.2.

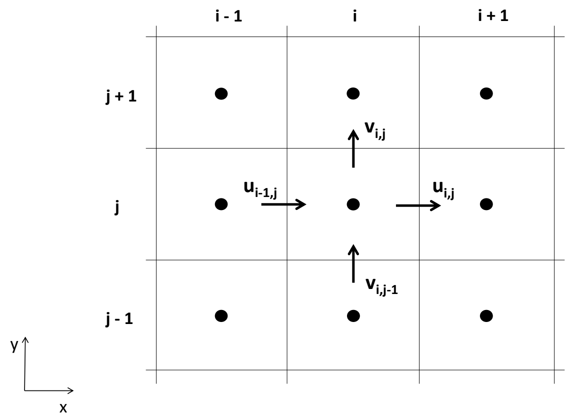

Figure 2.2: Example of a finite volume discretization. Adapted from [17].

The continuous conservation equation 2.34 is transformed into

$$\frac{\partial}{\partial t}\int_{\Omega} \mathbf{W} d\,|\Omega| + \int_{\partial\Omega} [\mathbf{E}(\mathbf{W}), \mathbf{F}(\mathbf{W}), \mathbf{G}(\mathbf{W})] \cdot \mathbf{n} d\,|\partial\Omega| = 0, \tag{2.43}$$

by integrating over the finite volume Ω, with $|\Omega|$ denoting the volume, $|\partial\Omega|$ denoting the surface area of the faces $\partial\Omega$ and $\mathbf{n}$ representing the outward pointing normal on $\partial\Omega$. Note that the averaging bars introduced by the Reynolds averaging are omitted from here onwards. This equation holds for a fixed mesh of finite volumes. However, as will be discussed later, unsteady aeroelastic simulations require an aerodynamic domain which can deform upon structural motion. This will cause deformations of the finite volume mesh. Mesh motion is incorporated in the governing equation by transforming it into the Arbitrary Lagrangian Eulerian (ALE) representation [9]. The time variation of the conservative variables $\mathbf{W}$ on the fixed volume is expanded in a term describing the time variation over the volume and a term describing the flux of the conservative variables across the edges due to mesh motion. Therefore the first term of equation 2.43 can be rewritten as

$$\int_{\Omega(t)} \frac{\partial \mathbf{W}}{\partial t} d\,|\Omega| = \frac{\partial}{\partial t}\int_{\Omega(t)} \mathbf{W} d\,|\Omega| - \int_{\partial\Omega(t)} \mathbf{W}\dot{\mathbf{x}} \cdot \mathbf{n} d\,|\partial\Omega|, \tag{2.44}$$

where $\dot{\mathbf{x}}$ denotes the mesh velocity. Introducing this description into 2.43 and rewriting gives

$$\frac{\partial}{\partial t}\int_{\Omega(t)} \mathbf{W} d\,|\Omega| + \int_{\partial\Omega(t)} \left([\mathbf{E}, \mathbf{F}, \mathbf{G}] \cdot \mathbf{n} - \mathbf{W}\dot{\mathbf{x}} \cdot \mathbf{n}\right) d\,|\partial\Omega| = 0, \tag{2.45}$$

which describes the finite volume formulation of the Navier-Stokes equations on a moving mesh. Replacing the volume integration by an integration matrix over the finite volume $\boldsymbol{\Omega}$ and the surface integral by a summation of the fluxes over the volume faces gives

$$\frac{d\,(\mathbf{\Omega W})}{dt} + \sum_{k=1}^{N} \left([\mathbf{E}, \mathbf{F}, \mathbf{G}] \cdot \mathbf{n} - \mathbf{W}\dot{\mathbf{x}} \cdot \mathbf{n}\right) \mathbf{n}_k \partial \Omega_k = 0, \tag{2.46}$$

where N stands for the total number of surfaces of the volume. In this formulation the flux is assumed to be constant over the surface. This equation can be written in a final semi-discrete condensed form:

$$\frac{d\,(\mathbf{\Omega W})}{dt} + \mathbf{R}(\mathbf{W}, \mathbf{x}, \dot{\mathbf{x}}) = 0, \tag{2.47}$$

with $\mathbf{R}$ denoting the residual vector describing the flux of the conservative variables by both convection and mesh motion.

2.2.5. Linear frequency domain

The Reynolds averaged Navier-Stokes method produces accurate results, even in the transonic regime. However, a direct approach by solving the RANS equations in the time domain is too computationally expensive for industrial aeroelastic applications. Therefore new solution methods were developed which retain RANS-like accuracy in the transonic regime at a significantly reduced cost.
One method is the linear frequency domain solution of the Navier-Stokes equations. Instead of expensive time integration, the semi-discrete RANS equations in ALE form shown in equation 2.47 are time-linearized around a steady-state condition and brought into the frequency domain. This time-linearization is justified for small harmonic perturbations of the structure, which is the physical onset for flutter. This method was originally developed for turbomachinery applications, but has been brought to application readiness for external flows in the recent years. All references discussed here show the application of LFD for external flows. Derivation of the theory for the Euler equations is given in [20] and for the full non-linear, inviscid Navier-Stokes equations in [23, 25]. The method has been introduced in the industrial flow solver TAU developed by the DLR, which has been discussed and validated in [19, 36]. The brief mathematical description given here is based on these references.

As said above, the starting point is the spatially discretized ALE RANS equation 2.47. The structural oscillations are assumed to be of a small, harmonic form, and thus the grid-node locations can be decomposed in a time-invariant mean denoted as $\bar{\mathbf{x}}$ and a time-dependent small perturbation. This small perturbation can be written in the frequency domain by taking only the first, harmonic term of a Fourier series expansion with amplitude denoted as $\hat{\mathbf{x}}$ and angular frequency as ω.

$$\mathbf{x}(t) \approx \bar{\mathbf{x}} + \hat{\mathbf{x}} e^{i\omega t} \tag{2.48}$$

Consequently the mesh velocity is approximated as

$$\dot{\mathbf{x}}(t) \approx \dot{\hat{\mathbf{x}}} e^{i\omega t}. \tag{2.49}$$

Assuming a linear aerodynamic response on the small amplitude oscillations, $\mathbf{W}$ can be decomposed accordingly:

$$\mathbf{W}(t) \approx \overline{\mathbf{W}} + \hat{\mathbf{W}} e^{i\omega t}. \tag{2.50}$$

Note that $\overline{\mathbf{W}}$ corresponds to the result of a steady state solution on the steady mean grid $\bar{\mathbf{x}}$. The integration matrix $\mathbf{\Omega}$ and the residual matrix $\mathbf{R}$ are found by a truncated series expansion.

$$\mathbf{R}(\mathbf{W}, \mathbf{x}, \dot{\mathbf{x}}) \approx \mathbf{R}(\overline{\mathbf{W}}, \bar{\mathbf{x}}, \dot{\bar{\mathbf{x}}}) + \left.\frac{\partial \mathbf{R}}{\partial \mathbf{W}}\right|_{\overline{\mathbf{W}}, \bar{\mathbf{x}}, \dot{\bar{\mathbf{x}}}} \hat{\mathbf{W}} e^{i\omega t} + \left.\frac{\partial \mathbf{R}}{\partial \mathbf{x}}\right|_{\overline{\mathbf{W}}, \bar{\mathbf{x}}, \dot{\bar{\mathbf{x}}}} \hat{\mathbf{x}} e^{i\omega t} + \left.\frac{\partial \mathbf{R}}{\partial \dot{\mathbf{x}}}\right|_{\overline{\mathbf{W}}, \bar{\mathbf{x}}, \dot{\bar{\mathbf{x}}}} \dot{\hat{\mathbf{x}}} e^{i\omega t} \tag{2.51}$$

$$\mathbf{\Omega}(\mathbf{x}) \approx \overline{\mathbf{\Omega}}(\mathbf{x}) + \left.\frac{\partial \mathbf{\Omega}}{\partial \mathbf{x}}\right|_{\bar{\mathbf{x}}} \hat{\mathbf{x}} e^{i\omega t} \tag{2.52}$$

Equations 2.48-2.52 can be introduced into equation 2.47. Higher order perturbation terms are neglected and $\mathbf{R}(\overline{\mathbf{W}}, \bar{\mathbf{x}}, \dot{\bar{\mathbf{x}}})$ is assumed to be zero, since this corresponds to the residual of a steady-state simulation.

This gives the final linearized equation for the amplitude of the aerodynamic response $\hat{\mathbf{W}}$ in the frequency domain:

$$\left[i\omega\bar{\boldsymbol{\Omega}}(\bar{\mathbf{x}}) + \left.\frac{\partial \mathbf{R}}{\partial \mathbf{W}}\right|_{\bar{\mathbf{W}},\bar{\mathbf{x}},\dot{\bar{\mathbf{x}}}} \right] \hat{\mathbf{W}} = -\left[\left.\frac{\partial \mathbf{R}}{\partial \mathbf{x}}\right|_{\bar{\mathbf{W}},\bar{\mathbf{x}},\dot{\bar{\mathbf{x}}}} + i\omega \left(\left.\frac{\partial \mathbf{R}}{\partial \dot{\mathbf{x}}}\right|_{\bar{\mathbf{W}},\bar{\mathbf{x}},\dot{\bar{\mathbf{x}}}} + \bar{\mathbf{W}}(\bar{\mathbf{x}}) \left.\frac{\partial \boldsymbol{\Omega}}{\partial \mathbf{x}}\right|_{\bar{\mathbf{x}}} \right) \right] \hat{\mathbf{x}}. \tag{2.53}$$

The LFD method has been validated for multiple test cases. The TAU-LFD solver has shown to retain the fidelity of conventional non-linear, unsteady RANS solvers for 2D and 3D test cases in the transonic regime, while achieving a computational time reduction of more than one order of magnitude [36]. Further validation experiments on 2D pitching airfoils and 3D low-aspect-ratio wings showed similar positive results [18, 24].
To conclude this discussion, one should consider the advantages and disadvantages of the LFD method. The main improvement is indeed the time reduction, which is achieved by three components. First of all, the non-linear system of equations reduced to a linear system of equations in the frequency domain. Secondly, the need for time-integration is eliminated, and hence convergence studies are no longer required. Finally, only four grid deformations are necessary to determine the right hand side of equation 2.53, instead of one per time-step. On the other hand, the LFD method also comes with some disadvantages. Practical implementation can be complex, since the method has to be implemented in the core CFD code, rather than other reduced order models which can work from outside. Furthermore, the required Jacobians ($\partial \mathbf{R}/\partial \mathbf{W}$) have to be consistent to the corresponding non-linear version. Finally, linearization of the turbulence models can also be challenging. [36]
It is important to note that the LFD method, because of its fundamental assumption of a linear aerodynamic response, can only be applied for small amplitude perturbations. This is suitable to compute the flutter onset or gust analysis [7, 8], but it is unsuited for non-linear limit-cycle oscillations (LCO) [32]. However, altogether it is shown that the LFD method can be a good solution for implementation in direct-CFD flutter simulations.

2.2.6. Tool environment thesis project

TAU, a CFD program developed by DLR, will be used as flow solver [28]. The implemented LFD method is documented in detail by Thormann and Widhalm [36]. However, even though this method poses a significant computational cost reduction with respect to unsteady RANS methods, it is still too expensive to compute each combination of structural lay-out and mass distribution. The LFD computation is therefore only done for a small number of reference conditions, which is in general only one mass distribution - structural lay-out configuration. The results of these computations are then mapped to each considered 'production'-run. This 'production'-run is a similar flight condition scenario with a different mass case or possible structural alterations due to the investigation of failure cases. The mapping is done by a least-squares method based on the relative mode shapes. Assume that the modal shapes of production runs $\boldsymbol{\Phi}_{\text{prod}}$ are superimposed out of the reference modal shapes $\boldsymbol{\Phi}_{\text{ref}}$

$$\boldsymbol{\Phi}_{\text{prod}} = \boldsymbol{\Phi}_{\text{ref}}\boldsymbol{\Psi} + \boldsymbol{\epsilon}, \tag{2.54}$$

with $\boldsymbol{\Psi}$ the least-squares coefficients and $\boldsymbol{\epsilon}$ the residual. The RMS (root mean square) of the residual $\boldsymbol{\epsilon}$ can be found by

$$\text{RMS} = \frac{1}{2}\boldsymbol{\epsilon}^T\boldsymbol{\epsilon} = \frac{1}{2}\left(\boldsymbol{\Phi}_{\text{prod}}^T\boldsymbol{\Phi}_{\text{prod}} - 2\boldsymbol{\Phi}_{\text{ref}}^T\boldsymbol{\Phi}_{\text{prod}}\boldsymbol{\Psi} + \boldsymbol{\Psi}\boldsymbol{\Phi}_{\text{ref}}^T\boldsymbol{\Phi}_{\text{ref}}\boldsymbol{\Psi}\right). \tag{2.55}$$

The least-squares method minimizes this RMS. The minimum is found by equalizing the gradient of the RMS matrix to zero

$$\nabla_{\boldsymbol{\Psi},\text{RMS}} = \boldsymbol{\Phi}_{\text{ref}}^T\boldsymbol{\Phi}_{\text{ref}}\boldsymbol{\Psi} - \boldsymbol{\Phi}_{\text{ref}}^T\boldsymbol{\Phi}_{\text{prod}} = 0, \tag{2.56}$$

which can be resorted to give following expression for the least-squares coefficients $\boldsymbol{\Psi}$

$$\boldsymbol{\Psi} = \left(\boldsymbol{\Phi}_{\text{ref}}^T\boldsymbol{\Phi}_{\text{ref}}\right)^{-1}\boldsymbol{\Phi}_{\text{ref}}^T\boldsymbol{\Phi}_{\text{prod}}. \tag{2.57}$$

Because small amplitude aerodynamics is a fundamental assumption of LFD, superposition of the generalized air force matrices is possible. The 'production' generalized air force matrix is computed by

$$\mathbf{A}^k_{\text{prod}} \approx \mathbf{\Psi}^T \mathbf{A}^k_{\text{ref}} \mathbf{\Psi}. \tag{2.58}$$

2.3. Aeroelastic coupling

Coupling the dynamic structural model and aerodynamic model is not straightforward. Two inherent problems of this coupling will be discussed. The first issue that is tackled is the spatial coupling strategy. The fluid and structural mesh do not match at their physical interface. Moreover, they commonly apply a different spatial discretization. At the interface, pressure forces computed with the flow solver have to be transferred to the structure and the deformation of the structure to the fluid mesh vice versa. This introduces the second problem: the fluid mesh has to adapt to the structural deformations. Automatic mesh deformation algorithms are in this respect indispensable, because complete regeneration of the fluid mesh requires a lot of time and manual input, which is practically impossible. An additional complexity for these mesh motion schemes is that they have to ensure that the resulting deformed mesh still maintains a good quality to solve the flow problem. The finite volume cells should not become skewed and strongly distorted cells resulting in a negative cell volume have to be prevented in any case.
This section will describe the spatial coupling and mesh deformation methods and tools used in the thesis project. Both procedures make use of the radial basis function interpolation method, which is therefore introduced first.

2.3.1. Radial basis function interpolation

The radial basis function interpolation method is a popular tool which approximates function values based on the distance of a target point with respect to the point where the function value is known. This section introduces the mathematical background of the method, the exact usage in the spatial coupling and mesh deformation programs will be discussed later.
Assume the displacement values are known in the structural grid nodes and have to be transferred to the fluid grid. The coordinates of the structural nodes are denoted as $\mathbf{x}_s$ and the corresponding function values as $\mathbf{S}_i$. The radial basis function description is defined for the structural grid s and the fluid grid f as

$$u_k(\mathbf{x}) = \sum_{i=1}^{n} \beta_i \phi(\|\mathbf{x} - \mathbf{x}_{s_i}\|) + q(\mathbf{x}), \quad \text{with, } k = s, f \tag{2.59}$$

where ϕ describes a sum of radial basis functions as a function of the euclidean distance $\|\cdot\|$ between the target and reference point. The coefficients β and $q(x)$ are defined by two interpolation conditions. The first condition is that the interpolation function matches the known values at the center points:

$$u_s(\mathbf{x}_{s_i}) = \mathbf{S}_i. \tag{2.60}$$

The second condition states that for a polynomial p at the center points, of a degree less than polynomial q, the following requirement holds

$$\sum_{i=1}^{n_s} \beta_i p(\mathbf{x}_{si}) = 0. \tag{2.61}$$

The obtained coefficients and polynomial are inserted in the radial basis function, which can then in turn be used to find the unknown function values on the target grid. Multiple radial basis functions ϕ have been developed. In general they can be divided in two groups. Basis functions with compact support as described by Beckert [6] and basis functions with global support as described and tested by Smith [29].

One of the main advantages of the RBF method is its applicability to a cluster of points for which no interconnectivity information has to be provided. This is particularly convenient for simulations covering large aircraft components or full aircraft, since the RBF domain can be easily partitioned in subdomains or groups of points [33]. Furthermore, De Boer et al. showed in a comparison with other frequently used interpolation methods for non-matching meshes that RBF interpolation could be the preferred method as it gives accurate results at a limited computational cost [13].

2.3.2. Spatial coupling of fluid and structural mesh

Spatial coupling at the interface of the fluid and structural mesh is governed by the FSAdvancedSplining module in the FlowSimulator environment. The background of this module is described in detail by Stickan et al [33]. FlowSimulator is the data handling framework linking all computational aeroelastic modules [22]. The employed interpolation method depends on the discretization of the structure used for the fluid-structure coupling:

- Radial basis interpolation, as discussed in the previous section, is used for surface interpolation when the structure is discretized by a dense surface grid. Multiple radial basis functions can be implemented.
- Beam splines are used when the structure is given as a stick model with all nodes on one line. Both translational and rotational degrees of freedom are in this case used in the interpolation.
- Rigid body splines are used if the structure is represented by one node. For this case also both translational and rotational degrees of freedom will be employed.

The program divides the computational surface (full aircraft, wing, etc.) in a number of domains. This is particularly important for the modeling of component boundaries such as the control surfaces. It also enhances the numerical efficiency of the spline functions. Partitioning the mesh requires extra attention at the interface between the sections. The surface meshes overlap at the boundary and a blending function is required to couple these adjacent domains. Furthermore, at critical locations an additional relaxation function can be used. These measures are required to guarantee a smooth transition between sections and a watertight CFD surface mesh.

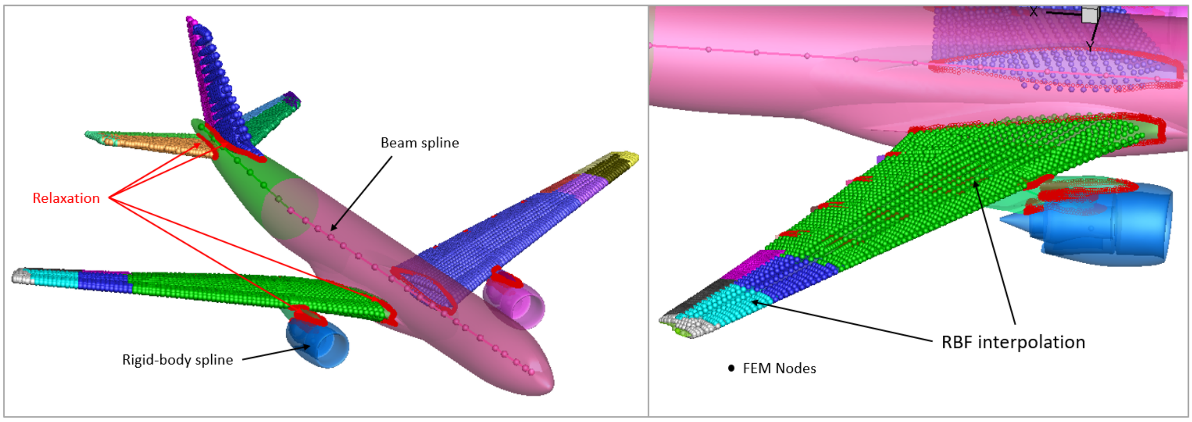

Figure 2.3: CFD-CSM coupling. Adapted from [33].

The coupling lay-out for the realistic aircraft configuration used in the thesis project is shown in Figure 2.3. As can be seen, the lifting surfaces are all modeled with the RBF surface splining method. All RBF interpolations for this configuration use the compact supported Wendland C^2 radial basis function [6]:

$$\phi(||\mathbf{x}||) = \begin{cases} (1-||\mathbf{x}||)^4(1+4||\mathbf{x}||), & 0 \le ||\mathbf{x}|| \le 1, \\ 0, & ||\mathbf{x}|| \ge 1, \end{cases} \tag{2.62}$$

The fuselage, engine pylons and flap track fairings are coupled with beam splines. The engine, which is only represented by one structural point, is coupled with a rigid body spline. Note that this coupling also depends strongly on a range of different settings (blending and relaxation distances, Wendland radius, base point reduction schemes, etc.), which are determined based on engineering judgment and best practice procedures.

2.3.3. Mesh deformation

Fluid mesh deformation is achieved by the FSDeformation module in the FlowSimulator environment. This module is described by Barnewitz and Stickan in detail in [4], and in lesser extent in [33]. The goal of the method is to interpolate the deformation of the aerodynamic surface grid further into the CFD finite volume mesh. Again, a domain partitioning approach is applied to improve the efficiency of the interpolation method and to prevent the computational cost from exploding. Additionally, it also enables independent movement of the different groups.

The deformation at each point of the complete grid is computed for each group deformation. At the interface between groups a linear blending function is applied to merge the deformations. This is shown in equation 2.63. The superscript g indicates a specific group and the subscript i a specific grid point. RZW is the 'Radius Zero Weight', which denotes the distance from the group where the deformations are no longer taken into account. RFW is the 'Radius Full Weight', which denotes the distance from the group within which the full deformations computed by the splining method are used. In the end, each grid point will have a deformation vector with entries corresponding to each group deformation. A weighted averaging function based on the distance between the specific node and group computes the final deformation at each grid point. The weighting function is given in equation 2.64. The computation of the displacement vector dx_i, with the final deformations for all grid points is shown in equation 2.65, where one can see how the deformations induced by each group (dx_i^g) are averaged with the weighting function and blended at the interface of the groups. Note that the partitioning of the domain and the input of the blending or weighting functions are determined based upon engineering best practice.

$$\text{blend}(d_i^g, g) = \begin{cases} 0 : d_i^g > \text{RZW}^g \\ 1 : d_i^g < \text{RFW}^g \\ \dfrac{\text{RZW}^g - d_i^g}{\text{RZW}^g - \text{RFW}^g} : \text{else} \end{cases} \tag{2.63}$$

$$\text{weight}(d_i^g) = \frac{1}{\sqrt{max\{d_i^g, \eta\}}} \tag{2.64}$$

$$dx_i = \frac{\sum_{g=1}^{n_g} \text{blend}(d_i^g, g) \cdot \text{weight}(d_i^g) \cdot dx_{v,i}^g}{\sum_{g=1}^{n_g} \text{weight}(d_i^g)} \tag{2.65}$$

The radial basis function interpolates the deformation of the base fluid nodes at the interface into the domain. The computational cost depends on the third power of the number of these base points. Therefore a base point selection scheme was introduced into the FSDeformation module to reduce the number of base points and consequently the computational time. Three different base point reduction methods are available.

- *Equidistant reduction* tries to select the base points spatial-evenly distributed. The algorithm starts from one base point and selects, outside of a minimum distance d_{min}, the closest new base point.
- *The error correction method* is described in detail by Allen and Rendall [3]. Within one iteration, the algorithm finds the base point for which the interpolation error is largest. It will then update the weighting coefficients of the radial basis function around this point.
- *Error weighting* is similar to equidistant reduction. The goal is to distribute the base points evenly. However, a weighting is applied to the distance calculation, which permits varying the base point density over the domain. The interpolation error can for example be used as weighting factor. Regions with a large interpolation error will then get a denser base point mesh.

The CFD-CSM model used for the thesis project was shown in Figure 2.3. The RZW, RFW, and maximum number of base points per domain were selected based on best practice experience. The fuselage domain used the error weighting reduction method, while all other domains used the equidistant reduction method as base point selection scheme.

2.4. Flutter solver

The end product of the unsteady aeroelastic simulations are damping and frequency curves over a range of flight levels for each combination of Mach number, mass loading and structural lay-out. In theory these curves can be found by brute force calculation of each flight speed - frequency scenario (for all mass loadings, Mach numbers, structural cases), similar to the approach used for flight vibration tests. However, this is not efficient in practice. Therefore dedicated flutter prediction methods have been developed.

The starting point for the flutter solver is the dynamic aeroelastic equation in generalized coordinates which was shown in equation 2.10. The pk-method is applied as solution algorithm. This method was developed specifically for the aeronautical industry with the goal to give an accurate flutter point and flutter curves with a physical meaning close to the flutter boundary. The fundamental assumption of the pk-method suggests that it is valid to approximate the aerodynamics of sinusoidal motions with slowly increasing or decreasing amplitudes using only pure harmonic aerodynamic results:

$$\mathbf{A}(p) = \mathbf{A}(\delta + ik, M_\infty) \approx \mathbf{A}(k, M_\infty). \tag{2.66}$$

Introducing this in the governing equation gives

$$\left[\frac{U_\infty^2}{b^2}p^2\mathbf{M} + \frac{U_\infty}{b}p\mathbf{D} + \mathbf{K}\right]\hat{\mathbf{q}} = \frac{1}{2}\rho U_\infty^2 \mathbf{A}(k, M_\infty)\hat{\mathbf{q}}, \tag{2.67}$$

which can be rewritten and simplified to

$$\left[\frac{U_\infty^2}{b^2}p^2\mathbf{M} + \frac{U_\infty}{b}p\mathbf{D} + \mathbf{K} - \frac{1}{2}\rho U_\infty^2 \mathbf{A}(k, M_\infty)\right]\hat{\mathbf{q}} = 0, \tag{2.68}$$

$$\mathbf{F}(p, k)\hat{\mathbf{q}} = 0. \tag{2.69}$$

This equation can now be solved for the Laplace variable p. Because $\mathbf{F}$ is a function of p and k, an iterative solution method has to be used. Therefore, the determinant iteration solution procedure, first described by Hassig [16], is introduced. Note that the dynamic equation of motion solved by Hassig contains extra transfer function terms to represent the control systems, but these are omitted here for simplicity.

The solution procedure is applied mode by mode and velocity by velocity. For one selected mode and one selected velocity the procedure is as follows. First select two initial guesses for p. For the first velocity case, the first guess can be the natural frequency case at $U = 0$ for p_1 and the same frequency, but a small added damping term for p_2. Subsequent velocity cases can make guesses based on extrapolation out of p-values of the previous velocity case.

$$p_1 = \delta_1 + ik_1 \qquad p_2 = \delta_2 + ik_2 \tag{2.70}$$

Then, compute or interpolate to obtain the aerodynamic force matrices for the assumed reduced frequency $\mathbf{A}(k_1, M_\infty)$ and $\mathbf{A}(k_2, M_\infty)$. Implement these in equation 2.69 and compute determinants $|\mathbf{F}(p_1, k_1)|$ and $|\mathbf{F}(p_2, k_2)|$. Now, the next p value can be computed with the Regula Falsi method:

$$p_{i+2} = \frac{p_{i+1}F_i - p_iF_{i+1}}{F_i - F_{i+1}}, \quad p_3 = \frac{p_2F_1 - p_1F_2}{F_1 - F_2} \tag{2.71}$$

This procedure has to be iterated until accepted convergence for the selected mode and velocity. Proceeding to the next velocity step is done by extrapolating the resulting p-values. Finally, this process has to be repeated for all considered elastic modes. A graphical representation of this solution procedure for one mode and two velocity points is given in Figure 2.4. Note that in this figure acceptable convergence is reached after one determinant iteration.

For the thesis project, the in-house developed program PKREG will be used as flutter solver [26]. In practice, equation 2.68 is used in a slightly adapted form:

$$\left[\mathbf{M}p^2 + \mathbf{D}_{gyro}p + \mathbf{K}(\mathbf{I} + \mathbf{D}_{struc}i) - \frac{1}{2}\rho U_\infty^2 \mathbf{A}(k, M_\infty) - \mathbf{R}(p)\right]\mathbf{q} = 0. \tag{2.72}$$

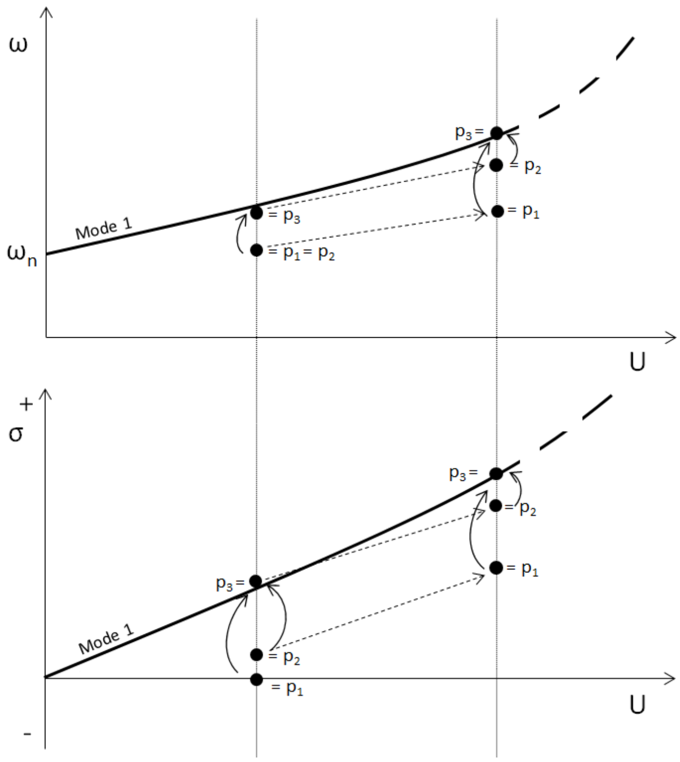

Figure 2.4: Visualization of the pk-method procedure. Adapted from [37].

The damping matrix is split up in two parts. $\mathbf{D}_{gyro}$ contains the gyroscopic damping term obtained from NASTRAN, and $\mathbf{D}_{struc}$ is a diagonal matrix structural damping values derived from GVT results. $\mathbf{M}$ and $\mathbf{K}$ are, respectively, the generalized mass and stiffness matrices, obtained from the finite element model in NASTRAN and $\mathbf{A}$ is the matrix of the generalized air forces obtained from the direct LFD method. The generalized air forces are given for a discrete number of reduced frequencies which are interpolated in the determinant iteration procedure to the desired reduced frequency value. Finally, $\mathbf{R}$ represents the transfer function for control and actuator forces which is computed by other subroutines [33].

2.5. Process overview of the unsteady aeroelastic simulation

Sections 2.1-2.4 described the building blocks of the high-fidelity unsteady aeroelastic simulation procedure. This section will give an overview of their practical interaction. A flowchart presenting the information flow between the different models is shown in Figure 2.5. The flowchart consists out of two parts. The steady CFD-CSM loop on the left and the unsteady (flutter) CFD-CSM loop on the right.

Steady CFD-CSM loop

The steady process uses a conventional RANS CFD scheme instead of the presented LFD method. Nastran Sol-101 (Linear Static) is used as structural solution sequence. The loads and displacement transfers as well as the mesh deformation are done through the spline interpolation functions discussed in Section 2.3. An additional trim control module verifies that the flight dynamical equilibrium is satisfied by assuring that the control surface conditions meet the flight settings ($C_{L_{\text{Target}}}$, $C_{m_y} = 0$, $a_x = 0$). The output of the steady CFD-CSM loop is a converged load (pressure) distribution and a steady flight shape [33, 34].

Unsteady (flutter) CFD-CSM loop

In the unsteady process two loops can be distinguished: the reference run which sets up the aerodynamic database and the production run for the investigated flutter computation.

Reference run
The aerodynamic loads are only computed for a small number of reference conditions (one nominal mass case per Mach number). The unsteady aerodynamics are linearized around the steady flight shape and control surface deflections which are determined with a steady CFD-CSM loop. The elastic mode shapes are determined with a modal analysis (Nastran Sol-103). The mesh deformations required for the LFD procedure are done with the presented FSDeformation module. Finally, the TAU-LFD solver will compute the small perturbation generalized air force matrix in the frequency domain for the reference conditions.

Production run
The production run also starts with a modal analysis performed by Nastran Sol-103 in order to find the mode shapes for the considered load case and structural lay-out. Then, the 'production' generalized air force matrix is determined through the least-squares approximation on the reference results, as shown in Section 2.2.6. Finally, the pk-solver produces the flutter diagrams based on the generalized mass, gyroscopic damping and stiffness matrices from Nastran, the generalized air force matrix from the least-squares approximation, the structural damping matrix derived from GVT results and possible control or actuator transfer functions from other subroutines [33].

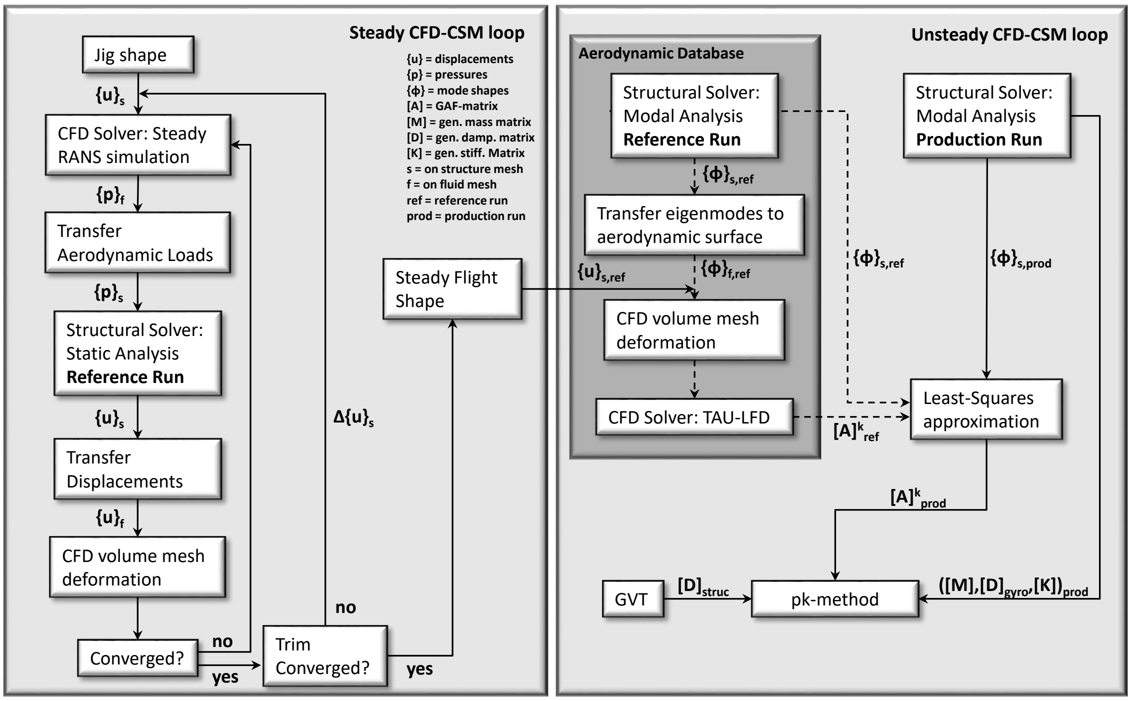

Figure 2.5: Flowchart of a full flutter calculation process. Adapted from [34].

2.6. Proper Orthogonal Decomposition (POD)

POD is a modal decomposition technique which determines the optimal set of modes to represent a reference set based on the L2 norm, which is commonly referred to as 'energy' of the input modes. POD was introduced for aeronautical application by Lumley as a method to extract coherent structures from a turbulent flowfield [21]. Currently, it is actively researched as method for model reduction in unsteady aerodynamic simulations [8, 15, 35]. However, in the scope of this thesis the POD method will be applied for a different purpose. As mentioned in Section 2.2.6, the new LFD unsteady aerodynamic method can only be computed for a limited set of elastic mode shapes. The POD method will be applied to improve the reference selection for this direct LFD application. The input will be a set of vibration modes of the aircraft for different structural lay-outs and mass distributions. The outcome of the POD decomposition will be a mode set which no longer represents the physical vibration modes of the aircraft, but can only be seen in a mathematical sense. This section introduces the working principles and theory of the method.

The goal of the POD method is thus to decompose a wide range of elastic modes for multiple considered mass and failure cases in an optimal, orthogonal reference set. The input modes are structured in a matrix with as column dimension all considered modes and as row dimension the degrees of freedom of each of these modes. The implementation of the POD method depends on the size of this input matrix. If the column dimension exceeds the row dimension, which would be the case if a large set of reference cases and only a subset of the degrees of freedom of the FEM is used, the classical POD method should be applied. When the opposite is true, which could be the case if all nodes and degrees of freedom of the FEM are used or if only a small set of reference cases is considered, the method of snapshots should be applied. Both these solution strategies are introduced here. Note that these methods give the exact same result, and the only reason for selecting one or the other is the memory and computational efficiency of the POD.

Classical POD method
Consider $\mathbf{X}$ to be the input matrix with the elastic mode shapes. The POD modes will be the eigenvectors of the eigenvalue problem

$$\mathbf{R}\boldsymbol{\phi} = \lambda\boldsymbol{\phi}, \tag{2.73}$$

with $\boldsymbol{\phi}$ the resulting POD eigenvectors, which can be assembled in a POD eigenvector matrix $\boldsymbol{\Phi}$, λ the eigenvalues corresponding to each of the POD modes and $\mathbf{R}$ computed as

$$\mathbf{R} = \mathbf{X}\mathbf{X}^T. \tag{2.74}$$

Method of snapshots
As mentioned, if the row dimension is large, the size of matrix $\mathbf{R} = \mathbf{X}\mathbf{X}^T$ can pose memory or computational time issues. Instead, the method of snapshots computes the eigenvalue problem on the, in this case, much smaller matrix $\mathbf{S} = \mathbf{X}^T\mathbf{X}$:

$$\mathbf{S}\boldsymbol{\theta} = \lambda\boldsymbol{\theta}. \tag{2.75}$$

The solution of this eigenvalue problem gives the same eigenvalues, but the POD eigenvector matrix $\boldsymbol{\Phi}$ has to be recovered from the computed eigenvectors $\boldsymbol{\theta}$ by

$$\boldsymbol{\Phi} = \mathbf{X}\boldsymbol{\Theta}\boldsymbol{\Lambda}^{-1/2} \tag{2.76}$$

with the input matrix $\mathbf{X}$, the intermediate eigenvector matrix $\boldsymbol{\Theta}$ and a diagonal matrix with the eigenvalues $\boldsymbol{\Lambda}$.

Properties of the POD mode set
The resulting set of POD modes has for both methods some useful properties. The POD modes are orthonormal, meaning that each mode has euclidean norm 1 and the inner product between two different modes equals 0. The POD eigenvectors are sorted by the relative information content they represent of the input modes. The strictly positive eigenvalue corresponding to each resulting mode is a measure for the amount of energy represented by that mode. Therefore, the eigenvalues are commonly used as truncation parameter to decide how many of the resulting modes should be used in order to capture approximately all energy contained in the reference. Only r number of POD modes have to be retained such that

$$\frac{\sum_{j=1}^{r}\lambda_j}{\sum_{j=1}^{n}\lambda_j} \approx 1, \tag{2.77}$$

with the eigenvalues λ and the total number or resulting POD modes n.

3 Error Estimation of the Reference Modal Basis Selection

The unsteady aerodynamics for a high-fidelity aeroelastic simulation is only computed for a limited number of reference modes due to computational cost constraints. This reference aerodynamics is then mapped to the specific flutter 'production' cases with a least-squares approximation method based on the relative mode shapes, i.e. the production modes are represented by a linear combination of the reference modes:

$$\mathbf{\Phi}_{\text{prod}} = \mathbf{\Phi}_{\text{ref}}\mathbf{\Psi} + \boldsymbol{\epsilon}. \tag{3.1}$$

The coefficients $\mathbf{\Psi}$ can be computed by

$$\mathbf{\Psi} = \left(\mathbf{\Phi}_{\text{ref}}^T\mathbf{\Phi}_{\text{ref}}\right)^{-1}\mathbf{\Phi}_{\text{ref}}^T\mathbf{\Phi}_{\text{prod}}, \tag{3.2}$$

which minimizes the RMS (root mean square) of the residual $\boldsymbol{\epsilon}$. This equation was introduced in Section 2.2.6, but repeated here for clarity because it forms the focal point of the upcoming discussions.
This chapter will present a study investigating the effect of approximation errors on the frequency and damping curves. The first section will investigate the best set of finite element nodes to represent the modes in the least-squares approximation. Then, a test case will be elaborated on which a set of reference modal basis quality criteria will be established. Finally, a study is shown which defines the best reference enrichment approach when the error criteria indicate that the reference modal basis set is not satisfactory for a given flutter computation.

3.1. Least-squares node selection

The least-squares approximation of the unsteady aerodynamics is made on the basis of the relative reference and production mode shapes. The question here is how to represent the modes such that the unsteady aerodynamics of the reference is also accurate for the production case. These modes should therefore represent as closely as possible the modes on the CFD surface which are seen by the flow solver. This section investigates which discrete nodal degrees of freedom should be selected to represent the modes in the least-squares approximation. Assuming that the CFD surface nodes are evenly distributed over the surface would suggest that selecting the CFD surface points would be a good starting point. The modes described on the structural grid have to be interpolated to the CFD surface nodes for each flutter computation to accomplish this. However, this is a computationally expensive process which is not practically feasible to be repeated for all production flutter computations. The least-squares approximation can therefore only be executed on the structural finite element nodes. In this section, four different methods for the LSQ node selection are defined and tested for a flutter computation with a nominal structural lay-out.
The first method uses all mass nodes of the dynamic structural model. At these points the structural and fuel masses are rigidly connected to the structural model. The distribution of the mass nodes is visualized in Figure 3.1a. The fuselage and all lifting surfaces are represented by a line of mass nodes

and the engine and pylon are both represented by one single mass node. The second method has the mass nodes as starting point, but adds interesting nodes based on engineering best practice. These additional nodes are placed on the leading and trailing edges of all lifting surfaces in order to better capture torsional mode shapes. Further points are added on the inlet and outlet of the engines to create a better representation of the engine modes in the least-squares approximation. This subset is visualized in Figure 3.1b. The third method uses only the fluid-structure coupling nodes, as visualized in Figure 3.1c. These nodes have a high density on the lifting surfaces in order to have an accurate fluid-structure coupling and only a limited number of nodes (the mass nodes) for the engines and fuselage. The fourth method uses the same set of fluid-structure coupling nodes, but applies a weighted least-squares approximation with the surface area of the CFD grid connected to each structural node as weighting. This method was used in order to give the limited number of nodes in the fuselage and engines a higher weight in the least-squares method, since these single points are connected to a large area of the CFD surface grid.

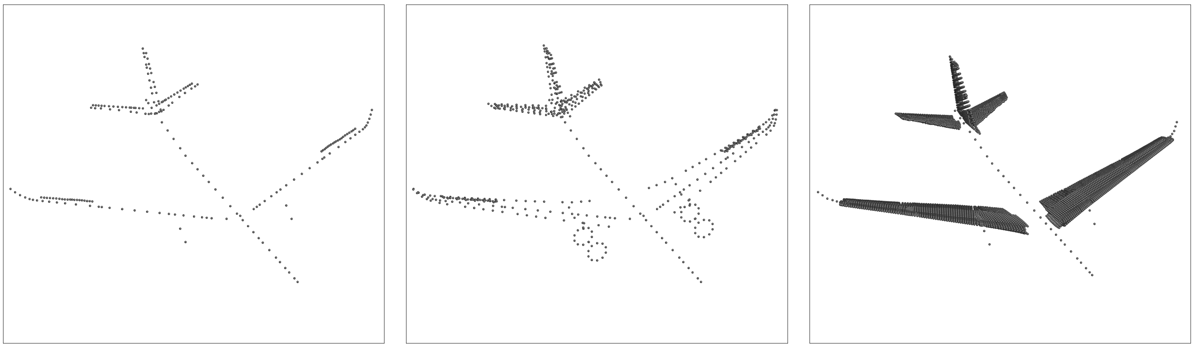

(a) Mass nodes (b) Manually selected LSQ nodes (c) FSI coupling nodes

Figure 3.1: Different finite element node subsets for LSQ approximation

These four different methods to represent the modes in the least-squares approximation were applied to the flutter computation of a nominal structure production case. The reference modal basis consisted of the elastic modes of the same nominal structural lay-out at a different mass distribution. The resulting frequency and damping curves are compared with a direct aerodynamic simulation in Figure 3.3 and 3.4 for different structural modes. The presented modes were selected based on the largest observed qualitative deviations. Figure 3.3 shows the frequency and damping progression of mode 9 and 22, which represent two engine modes as visualized in Figure 3.2. Only a section of the frequency and damping progression is shown to emphasize the differences. The results of the manually selected nodes and the area-weighted fluid-structure coupling nodes are in good agreement with the direct aerodynamics. Slight deviations in the frequency at high VEAS and significant deviations of the damping are visible for the least-squares approximation with the mass nodes and the fluid-structure coupling nodes. The single points in the least-squares approximation at the engine and pylon are not sufficient to represent the engine modes. The area weighting of the fluid-structure coupling nodes solved this issue. The higher weight given to the single engine point improves the representation of the engine deformation in the least-squares approximation.

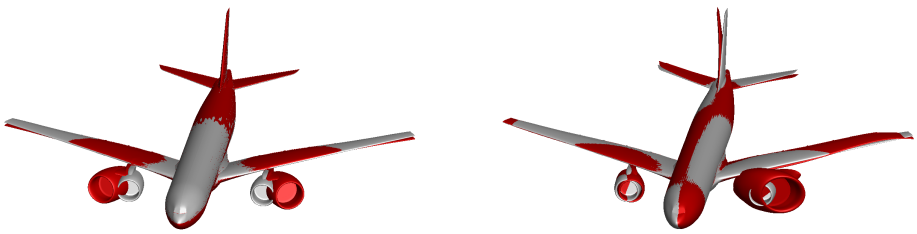

(a) Mode 9: Symmetric engine rotation (b) Mode 22: Non-symmetric engine rotation

Figure 3.2: Visualization of eigenmodes 9 and 22, detailed figures are available in Appendix D

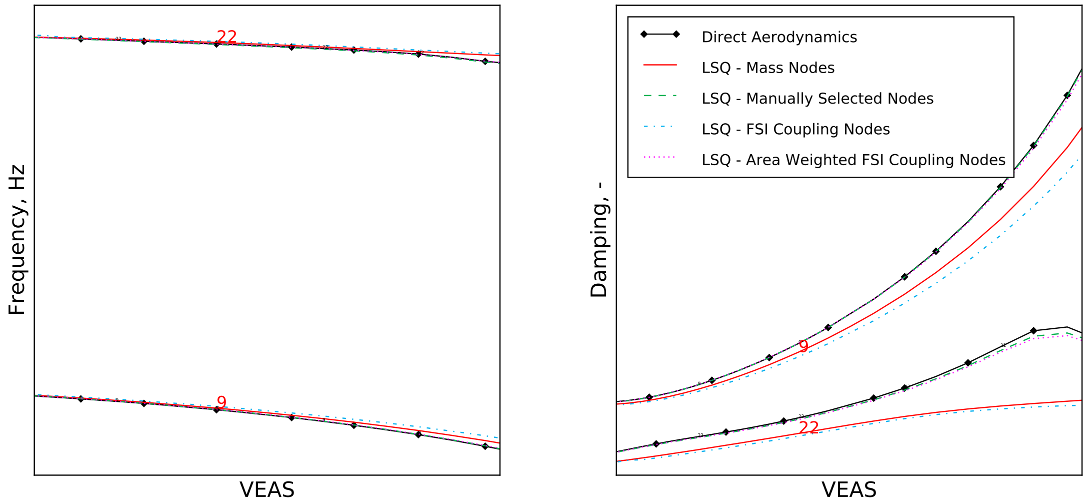

Figure 3.3: Frequency and damping curves of modes 9 and 22 (see Fig. 3.2) with different nodes for the LSQ approx.

Figure 3.4 shows the frequency and damping progression for modes 17, 20 and 49. These are three HTP modes, as visualized in Figure 3.5. These flutter results are presented to indicate that none of the presented methods is accurate for all modes with the given reference set. The poorest results are obtained with the fluid-structure coupling nodes, but small deviations in the damping progression are also visible for the other methods. However, both the method with the manually selected LSQ nodes and the area-weighted FSI coupling nodes are overall in good agreement with the direct aerodynamics. Note that the presented modes were the only ones with significant deviations. Both these strategies would therefore be a justifiable choice. For the remainder of this report the degrees of freedom of the manually selected LSQ nodes will be used to represent the modes in the approximation.

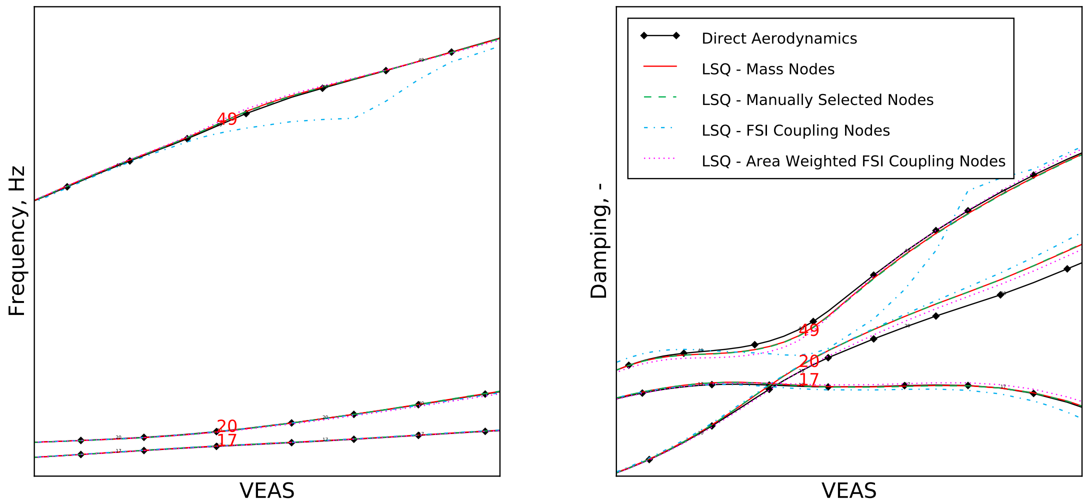

Figure 3.4: Frequency and damping curves of modes 17, 20 and 49 (see Fig. 3.5) with different nodes for the LSQ approximation

(a) Mode 17: HTP roll (b) Mode 20: 2n HTP bending (c) Mode 49: Sym. elevator rotation

Figure 3.5: Visualization of eigenmodes 17, 20 and 49, detailed figures are available in Appendix D

3.2. Error estimation test case description

An elaborate test case is set up to investigate the impact of the introduced approximation errors on the frequency and damping curves. The basis of the test case is a flutter computation with a structural failure of the outer bracket of the HTP-elevator connection. This failure case (FC) creates mode shapes which locally deviate strongly with respect to those of a nominal structure. Accurately approximating these failure case modes with only nominal structural modes as a reference will prove to be impossible. However, the observation was made that adding one HTP mode of this specific failure case to the reference set was sufficient to largely remove the error. The observed error reduction is not sensitive on the specific choice for this added mode, as long as a significant out-of-plane deformation of the HTP is observed in the mode shape. These findings are shown in Figure 3.6. This figure shows the frequency and damping curves of this elevator outer bracket failure case with three different reference sets for the least-squares approximation. The first reference set contains the exact modes of the flutter computation, essentially eliminating the need for interpolation. The second reference set is the nominal structure. And the third set is the same nominal reference set, enriched with the selected FC mode. The shown modes were selected manually, based on the clear deviations for these modes in frequency and damping progression. Mode 15 is the HTP roll mode, mode 20 the 2N HTP bending mode and mode 83 an non-symmetric HTP mode with a strong bending deformation of the damaged elevator. These modes are visualized in Figure 3.7 and in more detail in Appendix D. Significant differences can be observed between the approximation through the nominal reference and the direct aerodynamics and as said before, this error vanishes by adding one failure case mode to the reference set.

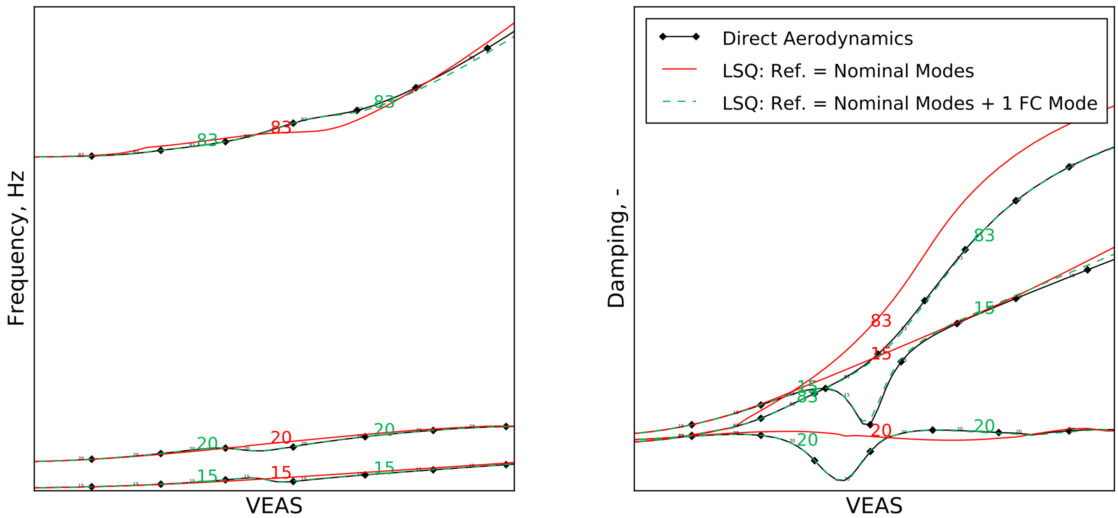

Figure 3.6: Comparison of frequency and damping progression for the Elevator Outer Bracket FC with direct aerodynamics, nominal reference and nominal reference + 1 FC mode

(a) Mode 15: HTP roll

(b) Mode 20: 2N HTP bending

(c) Mode 83: Non-symmetric HTP mode with bending deformation of damaged elevator

Figure 3.7: Visualization of eigenmodes 15, 20 and 83 of the Elevator Outer Bracket FC. Detailed figures are available in Appendix D

These results are exploited to make a test case for the error estimation study. The goal of this test case is to see a convergence from using only nominal reference modes to the nominal reference modes + 1 FC mode. This is achieved by adding a mode where the spring stiffness of the ruptured elevator bracket can be tuned artificially, instead of adding the exact FC mode to the nominal reference set. The tuned spring stiffness is artificial because it has no physical meaning. The only purpose of its introduction is to make mode shapes which lie in between those with the nominal structure and the failure case structure. Using a high spring stiffness is then essentially equal to using a nominal mode while using a decreased spring stiffness will make the mode shapes more closely corresponding to those of the failure case. The convergence of the frequency and damping curves of mode 15, 20 and 83 is shown in Figure 3.8. This convergence is solely influenced by the aerodynamic reference modes. In the next sections a set of quality criteria will be proposed which can be applied to each step of the convergence. This will show whether these error criteria are able to predict the errors and if best-practice thresholds can be defined below which the impact of approximation errors can be assumed to be negligible.

3.3. Reference modal basis quality criteria

The quality of the reference modal basis will be assessed by different quality criteria. All of them assess the approximated 'production' mode with respect to the exact target mode. As mentioned earlier, this quality assessment can in practice only be conducted on the structural grid. Interpolating the modes for all flutter computational cases to the CFD grid is too computationally expensive. The most common modal quality criterion is the MAC (mode assurance criterion) [2]. As starting point of this thesis, it was hypothesized that this criterion and other global mode assurance criteria would not be sufficient, since local errors can be averaged out if there is a good agreement for a large number of structural nodes. Therefore, additional quality criteria, either looking at the local mode approximation errors or the effect of mode errors on the GAF matrix, were established.

Three so-called levels of quality criteria are defined. The first level is the mode approximation errors, purely comparing the approximated mode and the exact, target mode. The second level is the aero-weighted mode approximation errors. The mode approximation errors will be weighted by the approximate magnitude of the unsteady aerodynamic forces at each node. This will make aircraft components with a greater impact on the unsteady loads have a greater impact on the error criteria. Finally, the third level is the approximate GAF errors. The GAF matrix used in the flutter computation is in essence the sum over all nodes of the aero-weighted modes. Therefore an approximate GAF matrix and an approximate error GAF matrix can be established. This section will introduce all quality criteria and later their performance will be shown for the test case.

3.3.1. Mode approximation errors

The mode approximation errors quantify the difference between the approximate and exact production modes, which are denoted as:

$$\begin{aligned}
&\text{Exact production mode matrix} && = \mathbf{\Phi}, \\
&\text{Approximated production mode matrix} && = \mathbf{\Phi}' = \mathbf{\Phi}_{\text{ref}}\mathbf{\Psi}, \\
&\text{Mode approximation error matrix} && = \mathbf{\Phi}^e = |\mathbf{\Phi} - \mathbf{\Phi}'|.
\end{aligned} \tag{3.3}$$

As mentioned before, the most common method to quantify the correspondence between two modes is the Mode Assurance Criterion (MAC) [2]. The MAC Error can be computed as

$$\text{MAC Error} = \max\left\{100\% - \frac{\left(\boldsymbol{\phi}_i^T\boldsymbol{\phi}_i'\right)^2}{\left(\boldsymbol{\phi}_i^T\boldsymbol{\phi}_i\right)\left(\boldsymbol{\phi}_i'^T\boldsymbol{\phi}_i'\right)}\right\}_{i=1,\dots,n_{\text{modes}}}. \tag{3.4}$$

Mode approximation errors can be seen mathematically as the residual $\boldsymbol{\epsilon}$ of the least-squares approximation, shown in equation 3.1. Approximation errors for least-squares methods are usually quantified by the RMS of the residual. This corresponds to the L2-norm of the mode approximation error. This error is normalized by dividing the RMS by the norm of the exact mode:

$$\text{Mode Norm Error} = \max\left\{\frac{\|\boldsymbol{\phi}_i^e\|}{\|\boldsymbol{\phi}_i\|}\right\}_{i=1,\dots,n_{\text{modes}}}. \tag{3.5}$$

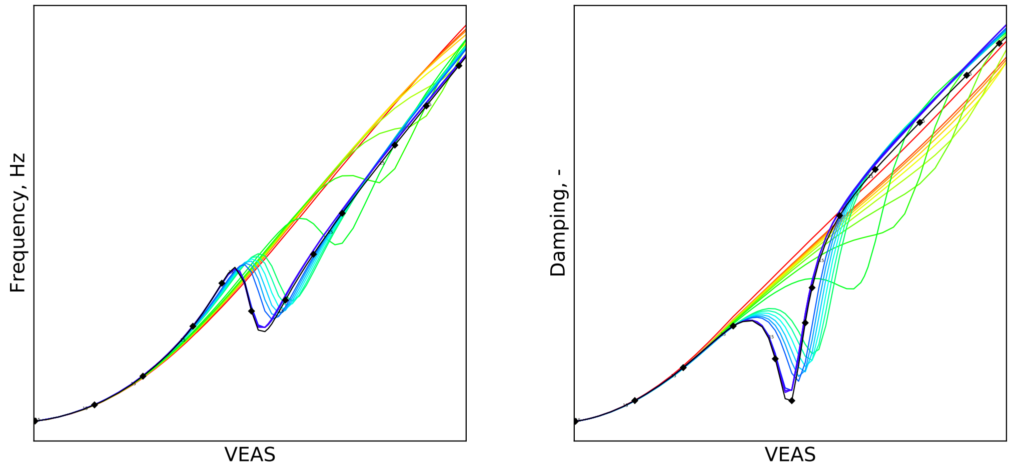

(a) Mode 15: HTP roll mode

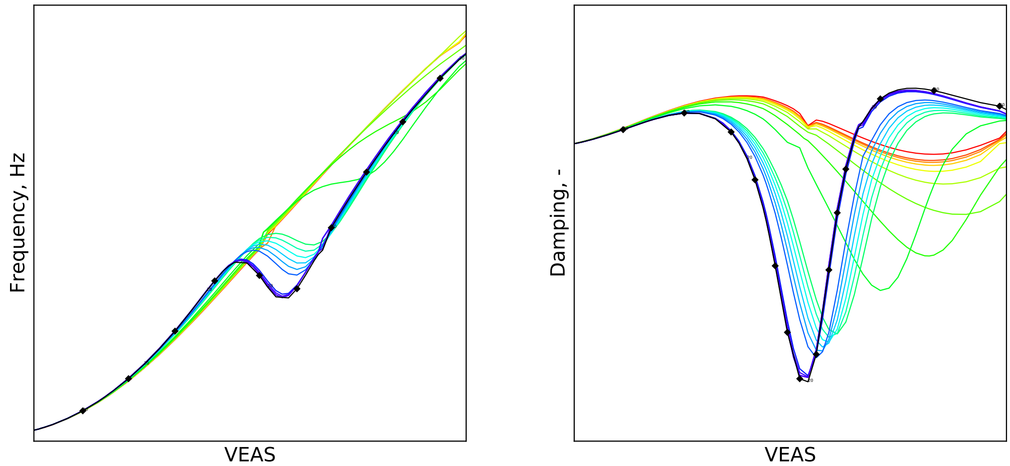

(b) Mode 20: 2N HTP bending mode

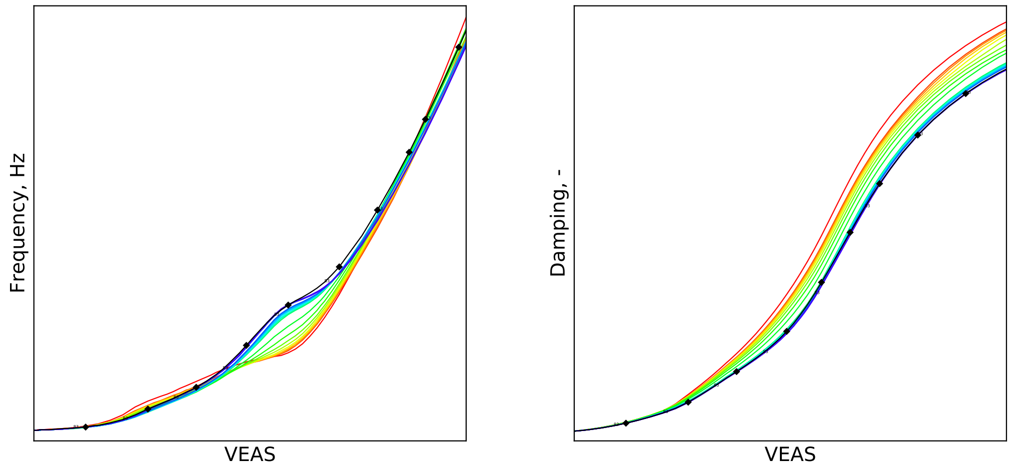

(c) Mode 83: Non-symmetric HTP mode with a strong bending deformation of the damaged elevator

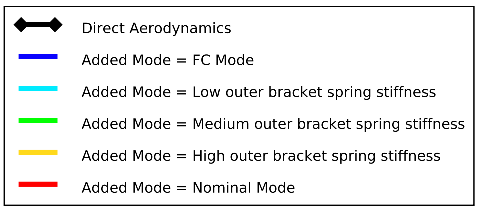

Figure 3.8: Convergence of frequency and damping curves for the error estimation test case. Coloring from red to blue indicates a reducing bracket spring stiffness from nominal mode to FC mode.

It was hypothesized that the MAC (and the mode norm error) could possibly average out local mode approximation errors, therefore maintaining a high quality value while this local bad approximation could have a significant impact on the flutter calculation. Therefore a local mode approximation quality criterium was established. The mode approximation error is assessed at each node of the finite element grid and normalized by the maximum displacement for that mode:

$$\text{Local Mode Approximation Error} = \max\left\{\frac{\max\left(\boldsymbol{\phi}_i^e\right)}{\max\left(\boldsymbol{\phi}_i\right)}\right\}_{i=1,\dots,n_{\text{modes}}}. \tag{3.6}$$

3.3.2. Aero-weighted mode approximation errors

It is hypothesized that even if there are large differences in the mode shapes, they are not necessarily influencing the GAF matrix and correspondingly the flutter computation. If, for example, the mode shape of the fuselage is badly approximated, the mode approximation quality criteria will be low. However, if the unsteady aerodynamic forces on the fuselage are small, a bad fuselage mode approximation will not have a big impact on the flutter results. A weighting of the mode approximation error with the approximate magnitude of the local unsteady aerodynamics is proposed to create the possibility to reduce or eliminate these errors.
The exact unsteady aerodynamics is in general not available for the production cases. The approximate unsteady aerodynamic force $\mathbf{F}_a'$ is therefore also computed through the least-squares approximation from the reference unsteady aerodynamic force $\mathbf{F}_{a,\text{ref}}$:

$$\mathbf{F}_a' = \boldsymbol{\Psi}^T \mathbf{F}_{a,\text{ref}}. \tag{3.7}$$

Note that this reference aerodynamic result $\mathbf{F}_{a,\text{ref}}$ has to be interpolated from the CFD grid to the structural grid. However, this requires only one interpolation which can be used for all flutter computational cases. All aero-weighed mode approximation errors are defined as the element-wise (denoted by $\circ$) multiplication of the modes with the magnitude of the local unsteady aerodynamic force.

$$\begin{aligned} \boldsymbol{\Phi}_w^e &= \boldsymbol{\Phi}^e \circ |\mathbf{F}_a'|, \\ \boldsymbol{\Phi}_w &= \boldsymbol{\Phi} \circ |\mathbf{F}_a'|, \\ \boldsymbol{\Phi}_w' &= \boldsymbol{\Phi}' \circ |\mathbf{F}_a'|. \end{aligned} \tag{3.8}$$

These results could physically be seen as a representation of the local work done on the system by each given mode.
Three similar quality criteria are defined with respect to the mode approximation errors. The first one is the aero-weighted MAC error, which can be computed by

$$\text{MAC}_w \text{ Error} = \max\left\{100\% - \frac{\left(\boldsymbol{\phi}_{w,i}^T \boldsymbol{\phi}_{w,i}'\right)^2}{\left(\boldsymbol{\phi}_{w,i}^T \boldsymbol{\phi}_{w,i}\right)\left(\boldsymbol{\phi}_{w,i}'^T \boldsymbol{\phi}_{w,i}'\right)}\right\}_{i=1,\dots,n_{\text{modes}}}. \tag{3.9}$$

Secondly, the mode norm error can be computed on the aero-weighted modes resulting in

$$\text{Aero-Weighted Mode Norm Error} = \max\left\{\frac{\|\boldsymbol{\phi}_{w,i}^e\|}{\|\boldsymbol{\phi}_{w,i}\|}\right\}_{i=1,\dots,n_{\text{modes}}}. \tag{3.10}$$

Finally, the local aero-weighted mode approximation error is defined as

$$\text{Aero-Weighted Local Mode Approximation Error} = \max\left\{\frac{\max\left(\boldsymbol{\phi}_{w,i}^e\right)}{\max\left(\boldsymbol{\phi}_{w,i}\right)}\right\}_{i=1,\dots,n_{\text{modes}}}. \tag{3.11}$$

3.3.3. Approximate GAF errors

The final group of error estimators are the approximate GAF errors. The GAF matrix is the input for the flutter computation and represents the energy contribution of each modal displacement on all other modes. The approximate GAF matrix and approximate error GAF matrix can be computed as the matrix product of the modes with the local unsteady aerodynamic forces:

$$\begin{aligned} \mathbf{GAF}^e &= \mathbf{\Phi}^e \cdot |\mathbf{F}'_a|, \\ \mathbf{GAF}' &= \mathbf{\Phi} \cdot |\mathbf{F}'_a|. \end{aligned} \tag{3.12}$$

The GAF matrices are in general square for each considered reduced frequency. Three different approximate GAF errors are defined. The elements on the diagonal of the GAF matrix represent the energy contribution of a certain mode to itself, i.e. how much energy is added or subtracted to a certain mode by its own modal deformation. This corresponds to the sum over all structural nodes of the aero-weighted modes. The first GAF error describes the relative difference of these diagonal elements between the error and the approximated GAF matrix:

$$\text{relative GAF error (diagonal terms)} = \max \left\{ \frac{\left|\mathbf{GAF}^e_{ii}\right|}{\left|\mathbf{GAF}'_{ii}\right|} \right\}_{i=1,\dots,n_{\text{modes}}}. \tag{3.13}$$

Taking the row sum of the GAF matrix is a measure for the energy contribution of all modes on a certain influenced mode. This gives a measure for the approximation error of all modes on the GAF for this specific mode. Again, this error is established relative with respect to the approximate GAF matrix:

$$\text{relative GAF error (influenced mode)} = \max \left\{ \frac{\left|\sum_{j=1}^{n} \mathbf{GAF}^e_{ij}\right|}{\left|\sum_{j=1}^{n} \mathbf{GAF}'_{ij}\right|} \right\}_{i=1,\dots,n_{\text{modes}}}. \tag{3.14}$$

On the other hand, the column sum of the GAF matrix is a measure for the energy contribution to all other modes of one specific excitation mode. This gives a measure for the impact of the approximation error of one mode on the GAF of all other modes:

$$\text{relative GAF error (excitation mode)} = \max \left\{ \frac{\left|\sum_{i=1}^{n} \mathbf{GAF}^e_{ij}\right|}{\left|\sum_{i=1}^{n} \mathbf{GAF}'_{ij}\right|} \right\}_{j=1,\dots,n_{\text{modes}}}. \tag{3.15}$$

3.4. Results of the error estimation test case

This section shows the resulting error estimation quality criteria for the presented test case. The error estimators were computed for each intermediate step of the convergence of the frequency and damping curves, visualized in Figure 3.8. Qualitative errors in the flutter curves were observed up to the last 4 steps of this convergence.

The mode approximation errors are the first level of error estimators. This error is graphically represented in Figure 3.9 for five snapshots of the flutter convergence. This figure shows the out-of-plane component of the mode approximation error on the fluid-structure coupling nodes for an HTP mode with the failure case. The error is high near the location of the ruptured elevator bracket when only the nominal reference is used or when the artificial spring stiffness of the added mode is kept high. Reducing this artificial spring stiffness of the added mode corresponds to a reduction and eventually disappearance of the mode approximation error.

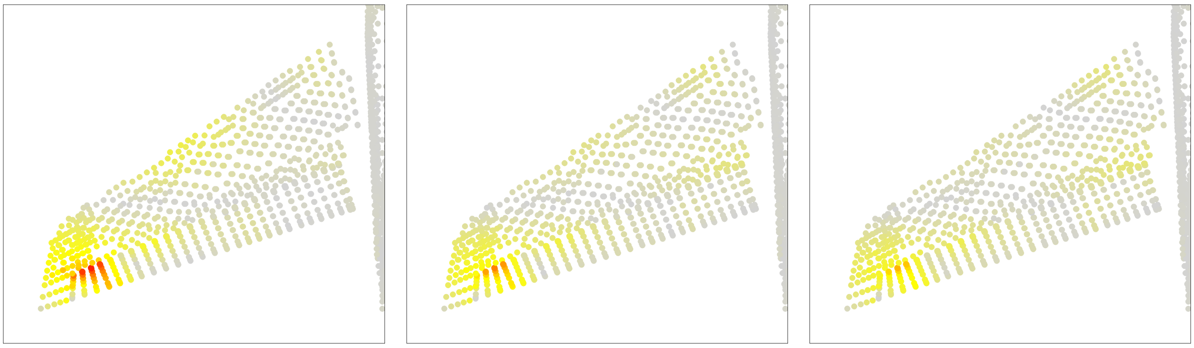

(a) Added Mode = Nominal Mode (b) Added Mode = High outer bracket spring stiffness (c) Added Mode = Medium outer bracket spring stiffness

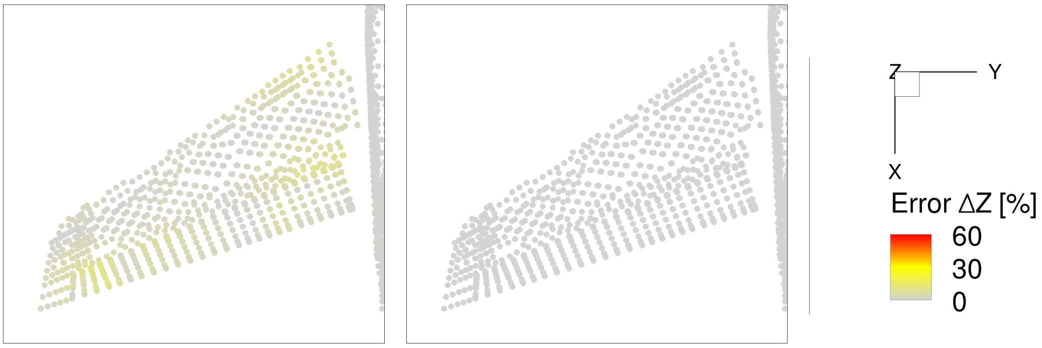

(d) Added Mode = Low outer bracket spring stiffness (e) Added Mode = FC Mode

Figure 3.9: Snapshots of the mode approximation error of an HTP mode of the Elevator Outer Bracket FC for the error estimation test case

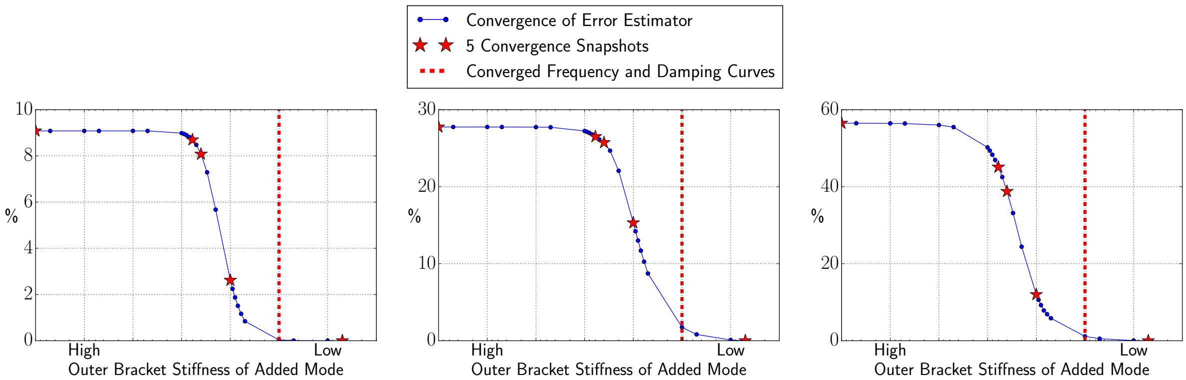

(a) Max. MAC Error (b) Max. Mode Norm Error (c) Max. Local Mode Error

Figure 3.10: Convergence of the mode approximation error estimators analogous to the convergence of the frequency and damping curves seen in Figure 3.8

The convergence of the mode approximation error estimators is shown in Figure 3.10. This figure shows the maximum MAC error, mode norm error and local mode error for each step of the flutter convergence which was shown in Figure 3.8. The x-axis represents the artificial spring stiffness of the additional reference mode which was variable to establish the qualitative convergence of the frequency and damping curves. If this artificial stiffness is high, the added reference mode corresponds to the nominal structure mode and the mode approximation errors are high. On the other hand, if the artificial spring stiffness is low, the added mode will correspond closer to the failure case mode which leads to low mode approximation errors. The convergence of the qualitative error which was seen in the frequency and damping curves in Figure 3.8 is found as well in the convergence of the mode approximation error criteria. The red markers in Figure 3.10 correspond to the snapshots shown in Figure 3.9. As mentioned previously, qualitative errors in the flutter curves were visible up to the four last convergence steps. This point is indicated here by the dotted red line. Each of the estimators shows a clear convergence up to this point corresponding to the qualitative errors seen in the frequency and damping curves. Even the MAC error and mode norm error are able to predict the LSQ error due to the bad local mode approximation. Figure 3.9 shows that these mode approximation errors were only locally around the ruptured elevator point. The hypothesis that the MAC and mode norm error would average these local errors because the majority of the structural nodes has a good mode approximation is thus not valid for this failure case.

The aero-weighted mode approximation errors are visualized for the same five snapshots of the flutter convergence in Figure 3.11. These figures show the distinct error when a nominal structure mode or a mode with a high artificial spring stiffness is added to the nominal reference set. The observed error is highly local around the failure case location, since here the mode approximation error is high and the unsteady aerodynamic forces are high due to the strong local deformation of the elevator tip for this HTP mode.

(a) Added Mode = Nominal Mode

(b) Added Mode = High outer bracket spring stiffness

(c) Added Mode = Medium outer bracket spring stiffness

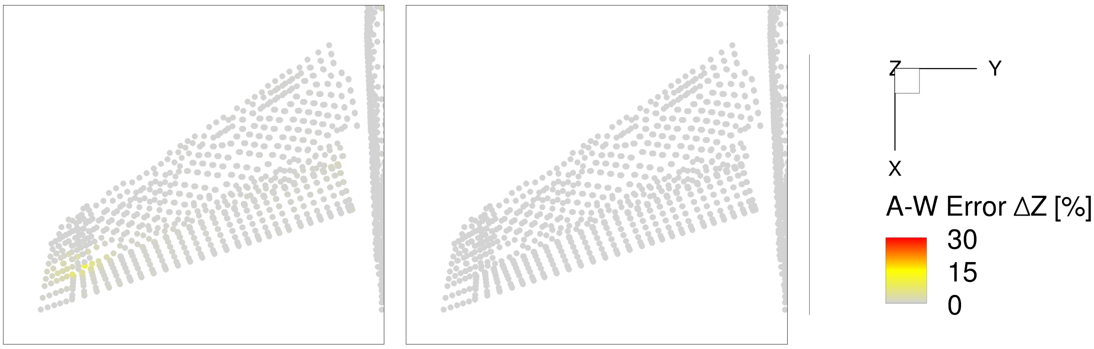

(d) Added Mode = Low outer bracket spring stiffness

(e) Added Mode = FC Mode

Figure 3.11: Snapshots of the aero-weighted mode approximation error of an HTP mode of the Elevator Outer Bracket FC for the error estimation test case

The convergence behavior of the aero-weighted mode approximation errors is shown in Figure 3.12. Again, all estimators seem to capture the qualitative convergence of the frequency and damping curves. The error criteria are high if the added reference mode has a high artificial stiffness and low if the artificial stiffness is low. However, the exact convergence trend is not equal for all estimators. An example of this different convergence behavior is the location of the second last (4th) snapshot. For the aero-weighted MAC error this point is located at a relatively small error of 1% (the max. error is 9%), while this point has relatively a higher error for the aero-weighted mode norm error and the aero-weighted local mode error.

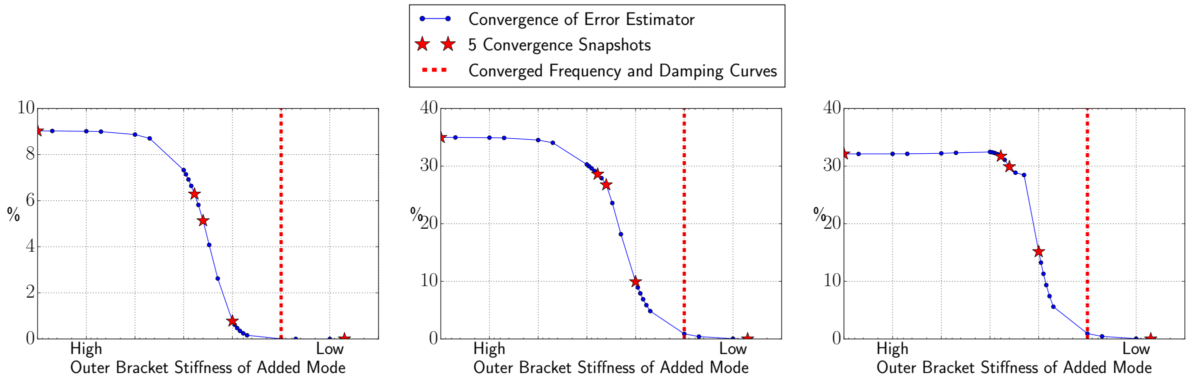

(a) Max. Aero-Weighted MAC Error (b) Max. Aero-Weighted Mode Norm Error (c) Max. Aero-Weighted Local Mode Error

Figure 3.12: Convergence of the aero-weighted mode approximation error estimators analogous to the convergence of the frequency and damping curves seen in Figure 3.8

Finally, the convergence of the approximate GAF error estimators is shown in Figure 3.13. Also here the qualitative convergence of the frequency and damping curves is visible in all error estimators. However, for both the maximum relative GAF Error of the excitation mode and the maximum relative GAF Error on the diagonal terms a small increase of the error estimator can be seen before the error converges. The relative GAF error for one of the modes becomes worse, while the error in the frequency and damping curves decreases.

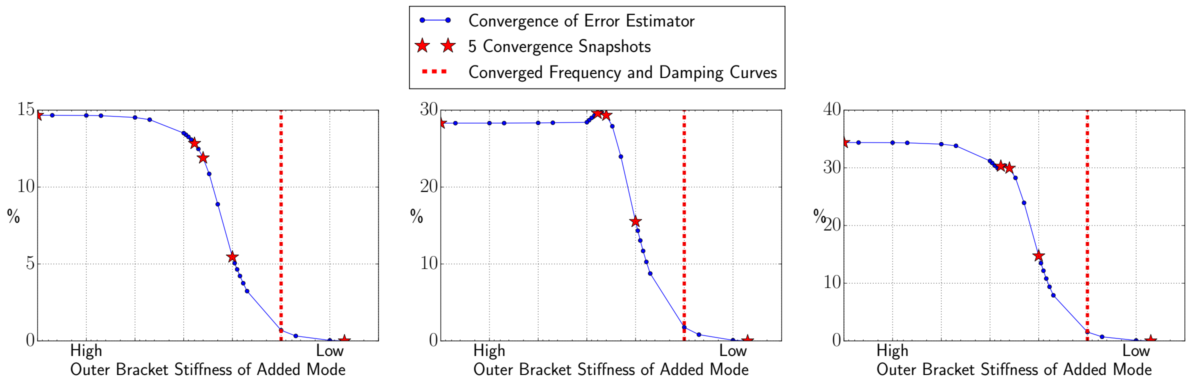

(a) Max. relative GAF Error influenced mode (b) Max. relative GAF Error excitation mode (c) Max. relative GAF Error - diagonal terms

Figure 3.13: Convergence of the approximate GAF error estimators analogous to the convergence of the frequency and damping curves seen in Figure 3.8

As a final result, the convergence of all error estimators is visualized in the same graph in Figure 3.14 with a normalized range of the respective errors. This figure shows clearly the similarity in the results of all error estimators. As mentioned before, the qualitative errors were visible in the frequency and damping curves up to the last 4 steps of the convergence, as indicated by the red line in the figure. Each of the estimators is able to predict this qualitative error as seen by the convergence up to this point. However, there are differences in the convergence behavior. An important parameter is the gradient of the curve close to the convergence point (red line). A flat convergence implies that a small change in normalized error would mean a large difference in resulting frequency and damping curves. This is unfavorable because it makes it difficult to define best-practice error estimation thresholds. This kind of convergence is seen for the aero-weighted MAC error. More favorable is a steep increase of the error estimator left of the convergence point, which is the case for all other error estimators.

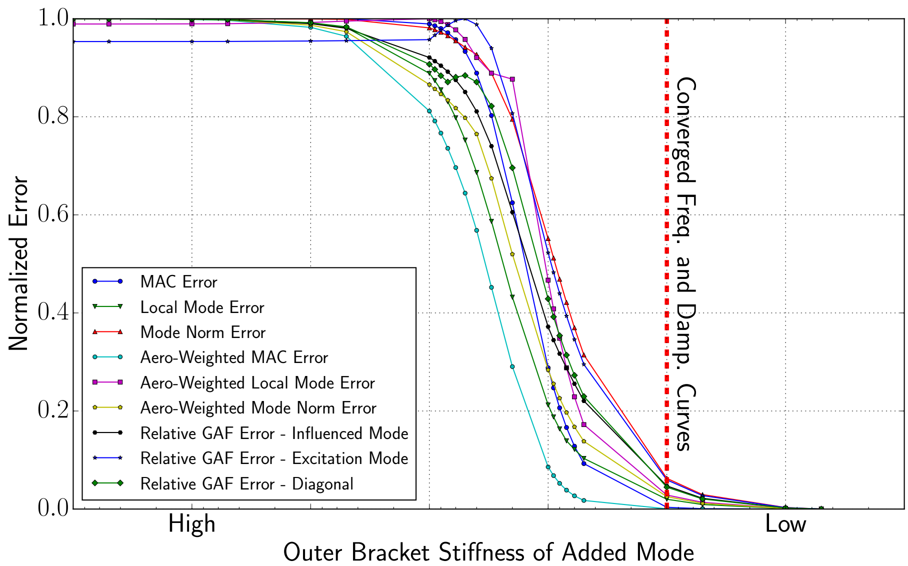

Figure 3.14: Comparison of convergence behavior of all error criteria

The conclusion of this error estimation study is that all quality criteria suffice for the presented test case, but the convergence behavior might favor some criteria. Global error criteria such as the MAC and the mode norm errors do not average out the local mode approximation errors, even though for the presented test case the mode approximation and aero-weighted mode approximation errors were situated only at a small area of the HTP around the ruptured bracket.

Best-practice thresholds can be defined for each quality criterium by relating the error estimator convergence with the qualitative convergence of the frequency and damping curves. For both the MAC error and aero-weighted MAC error this threshold was defined at 1%. For the relative GAF Error (diagonal terms) a larger error up to 5% was allowed. These criteria and their thresholds will be used in Chapter 4 to assess the quality of different reference sets. An overview of all best-practice thresholds is given in Appendix C.

3.5. Enrichment of the reference modal basis set

In the beginning of the chapter it was shown that adding one failure case mode to the reference basis was enough to eliminate the deviations in the frequency and damping curves. The selection of this mode was done by engineering judgment. An HTP mode was chosen for which a strong out-of-plane deformation of the elevator was visible. The question now arises if there is an optimal, automated way to enrich the reference modal basis with one or more additional modes such that the deviation is eliminated at the lowest possible cost.

Four different enrichment methods were examined. Method 1 adds the production mode for which the MAC error is largest. This corresponds to one column of the eigenvector matrix $\mathbf{\Phi}_{\text{prod}}$ in equation 3.1. Method 2 assembles the 10 modes for which the MAC errors are largest and then applies the POD theory, shown in Section 2.6 to decompose these modes into an orthogonal set. The first of these resulting POD modes, which should give the highest information content of the 10 selected modes, is added to the reference. Method 3 adds the error mode of the mode for which the MAC error is largest. This corresponds to a column of the residual matrix $\boldsymbol{\epsilon}$ of equation 3.1. Method 4 again applies the POD algorithm, but this time on the 10 largest error modes. The first mode of the resulting POD set is added to the reference. A visualization of the added modes for each of these four methods is shown in Figure 3.15. Note that method 1 and 3 are equal from a mathematical point of view. The exact production mode which is added for method 1 is a linear combination of the original reference modes $\mathbf{\Phi}_{\text{ref}}$ and the residual $\boldsymbol{\epsilon}$, which is added for method 3. Both methods should therefore give exactly the same results.

(a) Method 1: Production mode with highest MAC Error

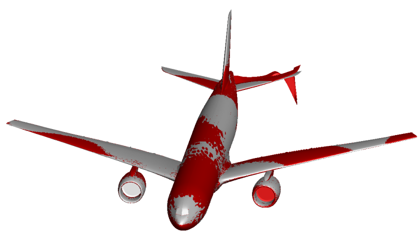

(b) Method 2: Dominant POD mode decomposed out of 10 production modes

(c) Method 3: Error mode of mode with highest MAC Error

(d) Method 4: Dominant POD mode decomposed out of 10 error modes

Figure 3.15: Added mode for each of the four investigated modal enrichment methods. Detailed figures are available in Appendix D

The effect of these different methods on the MAC error criterium is shown in Figure 3.16. Only the MAC error criterium is shown, but the same behavior was seen for all criteria. The MAC error drops with all four methods well below the best-practice quality threshold, which was defined at 1% MAC error. Based on these error criteria it seems that all four methods perform equally well. The error estimator for method 1 and 3 are exactly equal, confirming the mathematical theory.

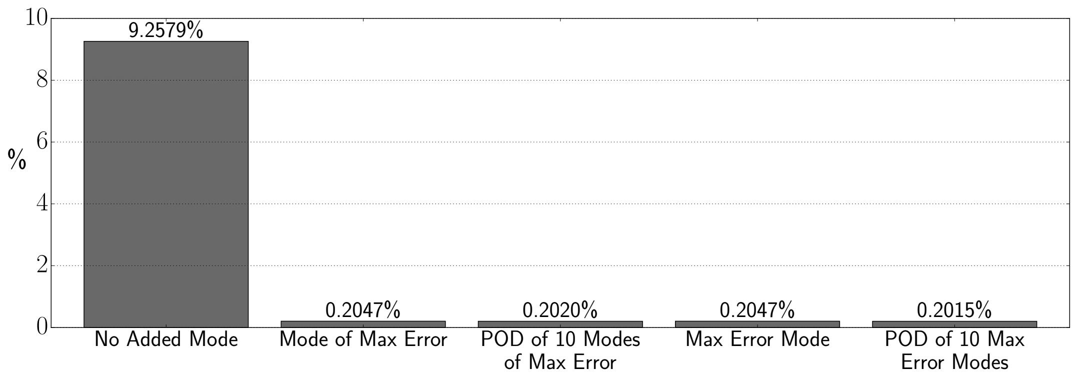

Figure 3.16: MAC Error for the Elevator Outer Bracket FC flutter computation with the four modal enrichment methods

As predicted by the MAC quality criterium, the error on the frequency and damping curves is eliminated by all four methods, as shown in Figure 3.17. All four enriched reference sets are in excellent agreement with the direct aerodynamics. The nearly equal performance of all methods can be explained by taking a closer look at the error modes for the production modes with the highest MAC error. The three modes with the highest MAC error and their corresponding error modes are visualized in Figure 3.18. These three most critical error modes are nearly identical, which shows that the mode approximation error is dominated by the small missing piece of modal information caused by the failure case, i.e. the residual is the same for the most critical modes. Each of the four presented enrichment methods succeeds in adding exactly this missing piece of information and correspondingly eliminates the approximation error. Enrichment of the modal basis when the error criteria indicate a non-satisfactory reference set can therefore be achieved automatically, without relying purely on engineering judgment.

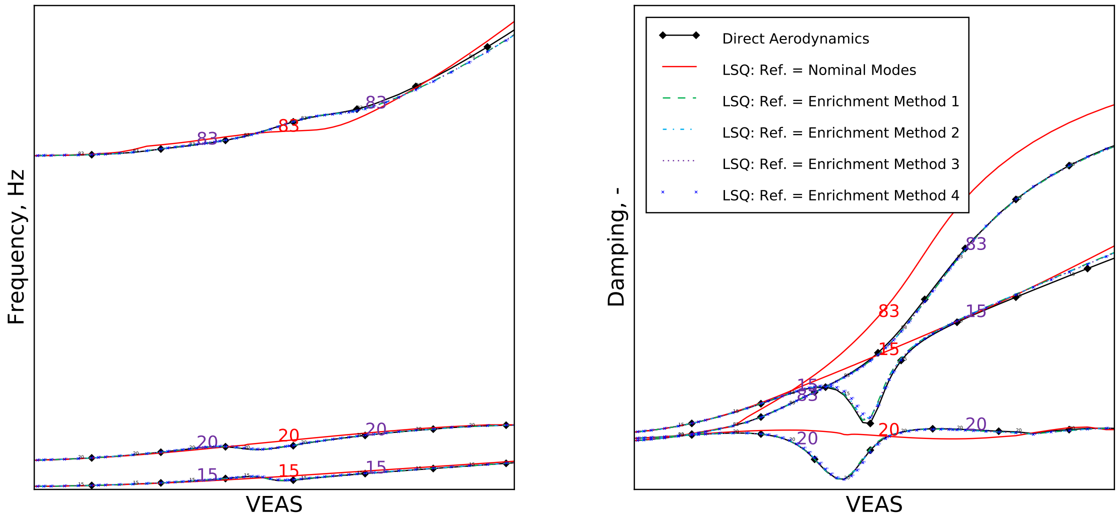

Figure 3.17: Comparison of frequency and damping progression of the Elevator Outer Bracket FC with direct aerodynamics, nominal reference and enriched nominal reference

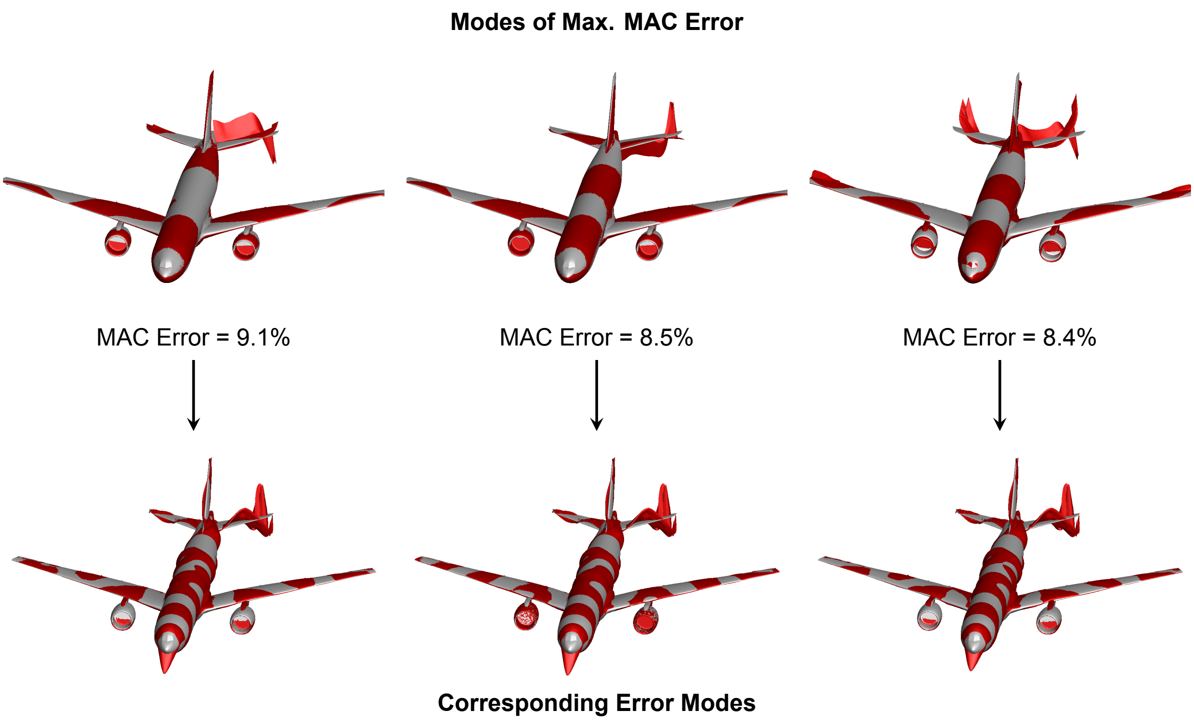

Figure 3.18: Three most critical error modes corresponding to the highest MAC errors. Detailed figures are available in Appendix D

3.6. Conclusion

The presented error estimation study of the elevator outer bracket failure case showed that multiple error estimators can be applied to predict the impact of the approximation error on the quality of the frequency and damping curves. This answers research question A posed in the thesis outline in Section 1.2. The hypothesis that a global quality criteria such as the MAC or mode norm errors would average out local mode approximation errors is disproved for this case, which was known for its strong local

mode approximation error. In cases where the quality criteria indicate a non-satisfactory reference set, the enrichment study has proven that an automated enrichment of the reference will eliminate the approximation errors by adding only one mode.
Despite these positive results, two drawbacks of the presented test case study have to be mentioned. First, for this test case there was no benefit in weighting mode approximation errors with the magnitude of the local unsteady aerodynamic forces. However, this result is influenced by the characteristics of the test case. The location of the mode approximation error, the outer section of the elevator, has for all critical modes also high unsteady aerodynamic loads. Yet, the hypothesis that aerodynamic weighting could benefit the error estimation does not apply to this case. As mentioned, it could give better results if a bad mode approximation of an aircraft component with relatively low unsteady loads occurs. This approximation error would not necessarily lead to deviations in the frequency and damping curves, which could be predicted if the mode approximation error is weighted by the low unsteady aerodynamics. Second, the results of the error estimators for a certain mode do not correspond directly to the errors in the frequency and damping for that specific mode. For a significant number of modes the error estimators are above the quality threshold while the frequency and damping curves are still in good agreement with direct aerodynamics. Hence, the error estimators should rather be seen as indicators for the likelihood of deviations in the frequency and damping due to least-squares approximation errors.
In practice, the knowledge obtained in this study can be used to predict the accuracy of reference mode sets for all production flutter computations and more specifically for the failure cases which have a large impact on the elastic mode shapes. Introducing these error checks will make the overall high-fidelity unsteady aeroelastic simulation more robust. Moreover, the error estimators can also be used to verify that an aerodynamic reference set is still satisfactory even if the structural model is updated throughout the development process, for example after the GVT or FVT. Otherwise the basis can be enhanced using the presented enrichment methods and thus re-computation of the complete reference aerodynamics can be avoided for e.g. updates of the structural model.

4
POD-based Reference Modal Basis Selection

The implementation of the direct-CFD method in the unsteady aeroelastic process could be improved by a more automated, robust and accurate reference modal basis selection. This section will present a study showing two methods for this reference selection and their performance for four different flutter computational cases. The first method uses the elastic modes of a nominal structural lay-out at one load case as reference. The second method will use the POD theory, explained in Section 2.6, to decompose a wide range of elastic modes for multiple load and structural failure cases into a proper orthogonal reference set. Both methods will be compared to the direct unsteady aerodynamics which were computed for the four test cases.

4.1. Description of the test cases

The performance of the two different reference modal basis selection methods will be tested by four flutter computational cases for which the exact unsteady aerodynamics are available as verification. The four flutter computational cases are:

- *Nominal structure case*: a case with a nominal structural lay-out. The applied mass distribution for this test case represents 100% payload and 0% fuel in all tanks.
- *Elevator Outer Bracket FC*: structural failure of the most outboard bracket of the HTP-elevator connection, see location in Figure 4.1. This is the same failure case which was used in the previous chapter. The rupture of the outer bracket of the elevator was known to give mode shapes with local deformations which are difficult to approximate with an unaltered, nominal structure.
- *Aileron Outer Bracket FC*: structural failure of the most outboard bracket of the outboard aileron, see location in Figure 4.1. This failure case was selected because of its resemblance to the Elevator Outer Bracket FC.
- *Rudder Outer Bracket FC*: structural failure of the most outboard bracket of the rudder, see location in Figure 4.1.This failure case was selected because of its low MAC mode approximation values and because of its resemblance to the Elevator Outer Bracket FC.

The steady flight conditions are the same for all test cases. The Mach number is 0.89 and the aircraft is trimmed to C_L= 0.40. The trimming is done rigidly assuming no additional deformation upon control surface deflections. The stiffness and mass matrices used in the flutter computations come from a validated Nastran FEM model and the structural damping values are derived from GVT data. Each flutter computation is done for 150 structural modes (of which 6 rigid-body and 8 control modes).

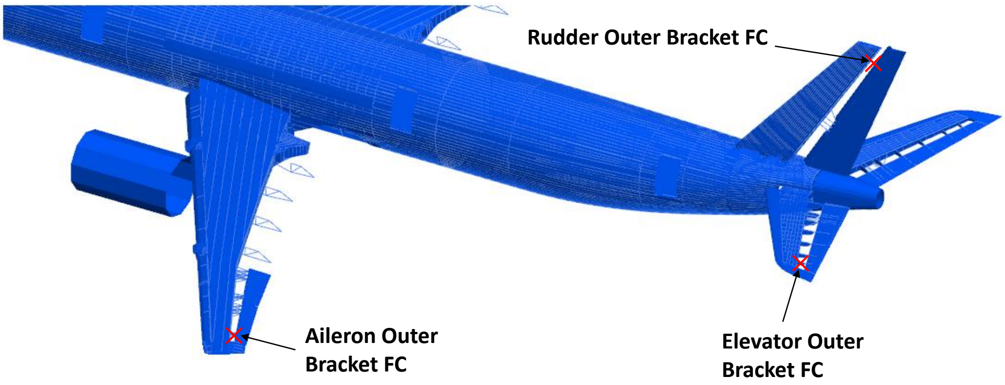

Figure 4.1: Location of the structural failures for the reference modal basis selection test cases

4.2. Selection of the reference sets

As mentioned, two methods for the reference set selection are tested. The first method uses the elastic modes of a single load case with a nominal structural lay-out. The second method applies the POD technique on a wide range of combinations of load case and structural failure cases.
The selection of the reference set for the first method is straightforward. All 150 elastic modes for a nominal structural case for one load case are used. The load case selection was made by engineering judgment to fit most closely with critical cases. The selected mass distribution of this reference set represents an empty aircraft with 50% fuel in the inner wing tanks, 100% fuel in the outer wing tanks, 0% fuel in the center tank and 100% fuel in the HTP trim tank.
The performance of the second reference selection method, however, is strongly influenced by some initial choices. Following five parameters are identified as the main influences:

1. *Input cases*: the selection of the input cases for the POD method is the first factor. The total certification space consists of more than 100 structural lay-out cases, each with approximately 30 load cases. For a complete description of the dynamic structural behavior each combination of structural lay-out and load case should be represented by at least 100 modes. This makes a total of approximately 300,000 possible POD input modes. Given the eigenvalue analysis and matrix products required for the POD method it is computationally impossible to use all these modes. Therefore a selection of the input cases will have to be made both for this test case scenario or when this POD-based reference selection method would be applied in practice.

2. *FEM nodes*: similar to the discussion in Section 3.1, the structural modes can be represented by different subsets of structural nodes. The whole finite element grid could be used, or only the fluid-structure coupling nodes, or even a subset of this. Optimally the lowest amount of nodes should be used which still gives an accurate representation of all important mode shape information such that the approximation errors are minimized.

3. *Mode normalization*: the mode normalization also plays a major role, since this determines the error norm which is minimized by the POD algorithm. The POD method decomposes the input based on the energy content. This makes that modes with a higher energy (L2-norm of the mode) will dominate the POD decomposition. The effect of different mode normalizations will be tested and discussed.

4. *Frequency limit*: the number of elastic modes for each selected input case could also be adapted. This mode selection can be done selectively, however in the scope of this thesis only the effect of an upper frequency limit on the input modes will be investigated.

5. *POD truncation*: the POD method will result in a mode set with an equal number of modes as provided in the input. This will be a large number of modes with the majority only representing a minimal amount of information of the input. Therefore a truncation method is required which decides how many resulting POD modes are retained.

Investigating the influence of these parameters by computing the unsteady aerodynamics for different parameter combinations is practically difficult given the significant computational cost of the unsteady aerodynamics. Therefore the error estimators for the four test cases are analyzed to predict the performance of the POD reference set for different parameter combinations. Only the MAC, aero-weighted MAC and relative GAF error (diagonal terms) will be used. All error estimators shown in this section are an average over the four test cases. The quality criteria are only computed for the first 75 modes of each test case, because of the importance of a good approximation quality of these lower frequency modes. This section will justify the choices made concerning each of these influential parameters either by their performance or by a practical implementation argument.

4.2.1. Input cases

As discussed in Section 4.2, four test cases will be used to check the performance of the selection methods. For this test case scenario only these structural cases will be used as input for the POD. The proposed method to select the input cases for the POD to represent the full flutter space will be discussed in Section 4.4 of this chapter. More input cases with a nominal structure were selected to give the nominal structural modes a higher weight. In total 7 different load cases with a nominal structural lay-out were used alongside 3 load cases for each of the 3 considered failure cases. This makes a total of 16 input cases.

4.2.2. Node selection

Different subsets of finite element nodes can be selected to represent the POD input modes. Ultimately, the selected nodes should be optimal to give the best POD set for the least-squares mapping from the reference to each of the flutter production cases. It is therefore evident that using the same nodes as for the least-squares approximation would be a good choice. In Section 3.1 it was shown that a manually selected subset with the mass nodes and the additional nodes on leading and trailing edges of lifting surfaces as well as on the inlet and outlet of the engines will be used for this purpose. Moreover, this is only a small subset of approximately 500 nodes which is favorable from a computational point of view. Computational efficiency of the POD decomposition is no issue for the considered test case scenario with only 16 input cases, but could be a significant factor if the method will be applied to the full flutter computational space.

This subset of LSQ nodes has one disadvantage. The POD method will only describe the resulting modes for the same nodes which are provided in the input. However, in order to be able to transfer the modal deformations to the aerodynamic grid for the unsteady aerodynamic computations, these deformations have to be known at all fluid-structure coupling nodes. Therefore an additional mapping of the POD modes to the fluid-structure coupling nodes is needed if only the LSQ nodes are used. The working process of this approximation is shown in Figure 4.2. This method has a high efficiency and accuracy. The MAC mode approximation error remains smaller than 0.01% and thus is not affected through the approximation.

This section will provide a performance comparison between the use of the LSQ nodes and the corresponding required interpolation and the use of the LSQ nodes and the fluid-structure coupling nodes directly in the input, eliminating the interpolation need.

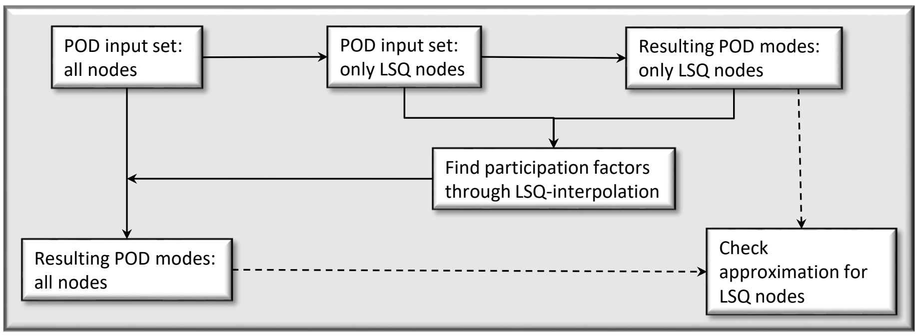

Figure 4.2: Approximation method from LSQ nodes to all nodes for the POD method

Figure 4.3 shows the average of the error estimators of the four different test cases for both methods. Representing the input modes only by the LSQ nodes leads to a significantly lower average MAC error. However, the average MAC error when both the LSQ and fluid-structure coupling nodes are used is still below 1%, the best-practice quality threshold. The lower mode approximation performance is an effect of the distribution of the coupling nodes. As was seen in Figure 3.1c, the coupling density varies over the aircraft with a high density on the lifting surfaces and a low one on fuselage and engines. As a result, the fuselage and engine mode deformations will not be well represented in the resulting POD set. This conclusion is supported by the results for the aero-weighted MAC error and relative GAF error. Here, the performance for both methods is almost equal, with only slightly favorable results if only the LSQ nodes are used. The mode approximation errors at locations with a low number of coupling nodes is averaged out by the aero-weighting, because areas with a low coupling node density correspond to areas with a low magnitude of the unsteady aerodynamic forces.
These results show that both from a performance and computational efficiency perspective the use of the LSQ nodes will be the most optimal choice of nodes to represent the POD input modes.

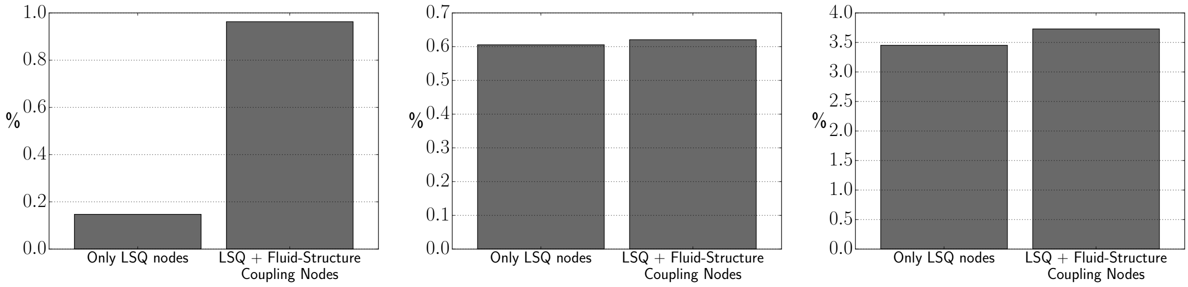

(a) MAC Error (b) Aero-Weighted MAC Error (c) Relative GAF Error

Figure 4.3: Average error estimators of the test cases for different POD input node selections

4.2.3. Mode normalization

The POD method decomposes the input modes based on their L2-norm, which is referred to as energy of the input modes. The normalization of the input modes will therefore affect the weight of these modes in the POD decomposition. Three different mode normalization options are tested. First option: Mass normalization, which is often the preferred format in structural dynamic tools (Nastran), because it simplifies the aeroelastic equation. Second option: Max normalization, which normalizes the maximum deflection of all modes to 1. Third option: Orthonormalization, which normalizes each mode to vector length 1. The energy content of a given mode can be represented by this L2 vector norm. As an example, the L2 norm of the three discussed normalizations for a nominal structure mode set is given in Figure 4.4. Mass normalization causes the higher frequency modes to have the highest energy content. Max normalization gives an approximately even distributed energy content, with a slight increase for the first modes and some significant outliers. The L2 norms after orthonormalization are all equal to 1, by definition.

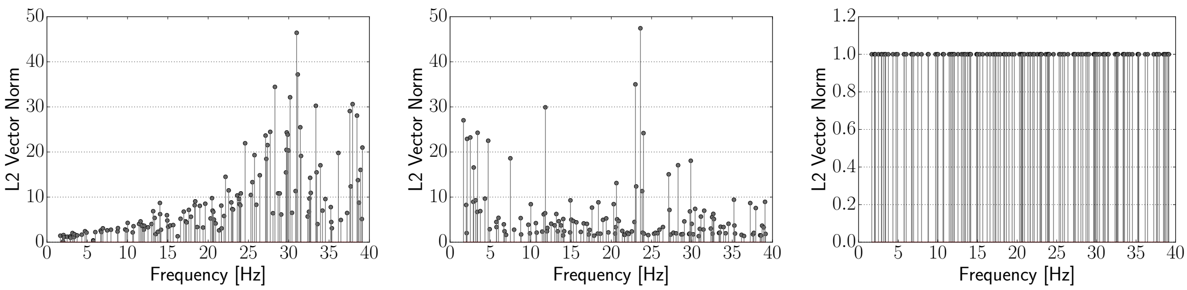

(a) Mass Normalization (b) Max. Normalization (c) Orthonormalization

Figure 4.4: Example of L2 vector norm for all modes of nominal structure for different mode normalizations

The resulting average error criteria for the four test cases are shown in Figure 4.5. The same conclusions can be drawn from all three criteria. Max- and orthonormalization do not differ significantly in their performance, but they are both clearly better than mass normalization. This is caused by the unfavorable L2 norm distribution after mass normalization, as seen in Figure 4.4a. Lower frequency modes should have a good approximation and should therefore be well represented in the POD. Using both max and orthonormalization would therefore be a good choice. For this thesis max normalization will be applied.

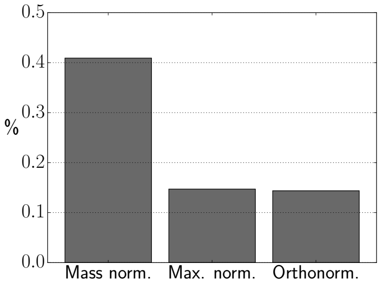

(a) MAC Error

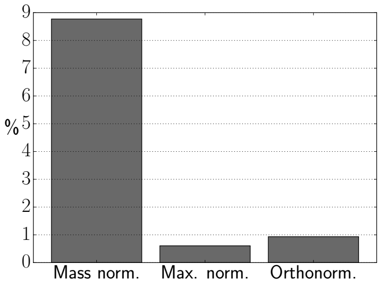

(b) Aero-Weighted MAC Error

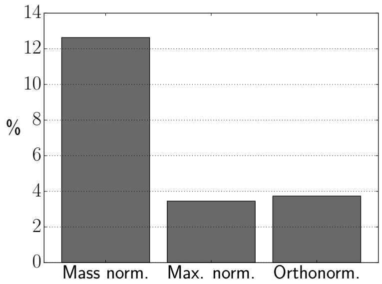

(c) Relative GAF Error

Figure 4.5: Average error estimators of the test cases for different normalizations of the POD input modes

Moreover, this study shows that normalization of the input modes can be a strong tool which can be used to further improve the performance of the POD method in the future. Low frequency modes could be favored by giving them an additional weight, or modes which are known to be critical for a given aircraft model could be emphasized similarly by giving these an additional weight in the input. Besides this, advanced weighting methods could be applied. Simple and quick DLM aerodynamics can be computed for the input modes and added as a weighting factor such as to favor those modes and nodes which have a strong influence on the generalized air force matrix.

4.2.4. Frequency limit

A selection of modes could be made for each of the input cases. First, it is important to note that only the natural modes are considered in the POD method. The rigid-body and control modes are independent of the structural lay-out and load case and would therefore be superfluous in the POD input. The 6 rigid-body modes and 8 control deflection modes are added to the resulting POD set afterwards. The modes considered for each input case could be picked selectively, but for this thesis only the effect of an upper frequency limit is considered. Table 4.1 illustrates the average number of modes per input case related to each considered frequency limit. The average error estimators for the lowest 75 modes of the four test cases are shown in Figure 4.6. The errors reduce when the frequency limit is increased. However, the aero-weighted MAC error and the relative GAF error increase again for 30 Hz or without frequency limit. This is because the modes added above 25 Hz do not provide any information for the lowest 75 modes which were used for the error estimation. Adding this superfluous information in the POD input therefore only deteriorates its performance.

Table 4.1: Average number of modes vs. frequency limit

Freq. Limit [Hz]	10	15	20	25	30	No Limit
Average # of modes per input case	26.8	46.4	63.6	84.8	102.6	136

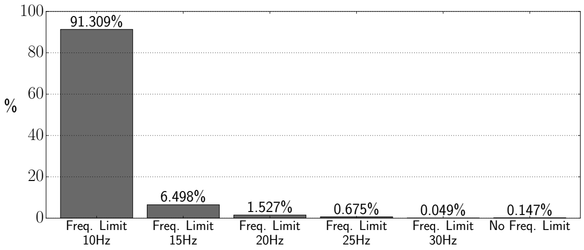

(a) MAC Error

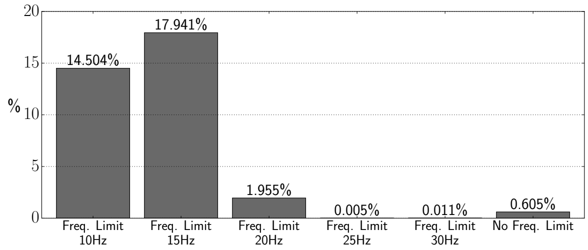

(b) Aero-Weighted MAC Error

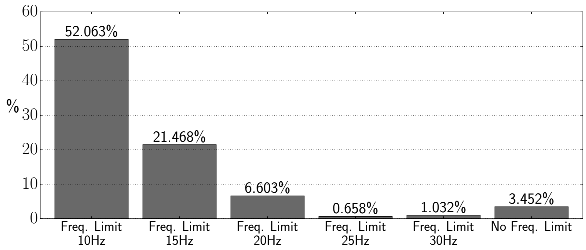

(c) Relative GAF Error

Figure 4.6: Average error estimators of the test cases for different frequency limits imposed on the POD input modes

This effect is even more clearly visible in Figure 4.7, which shows the MAC error for all modes of the Elevator Outer Bracket FC test case with the POD reference made with different frequency limits imposed on its input. The error shifts together with the frequency limit which was imposed on the POD input. This leads to the conclusion that the frequency limit should be imposed on the same limit one is interested in for the flutter computations. For the test case scenario in this report no frequency limit is imposed, since the same frequency band is represented in the input modes as will be used in the end to perform the flutter computation.

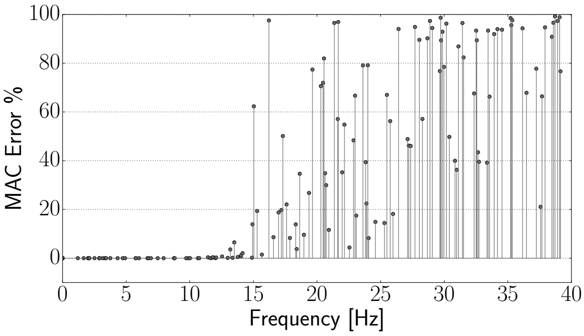

(a) Frequency limit of 10 Hz

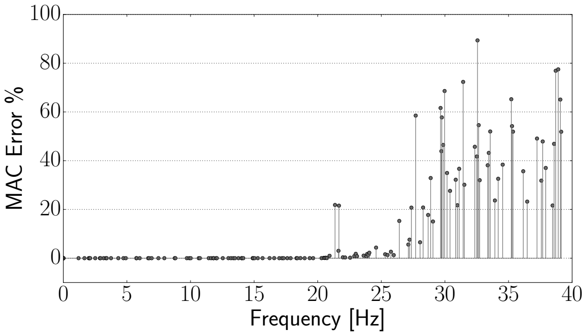

(b) Frequency limit of 20 Hz

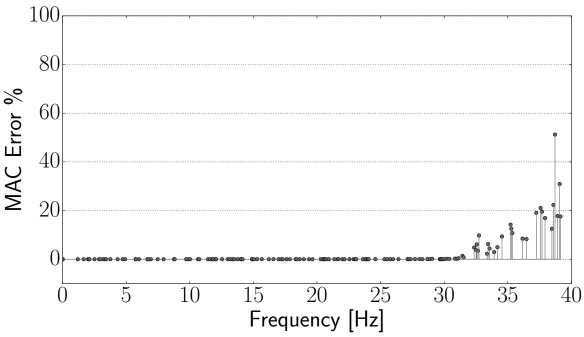

(c) Frequency limit of 30 Hz

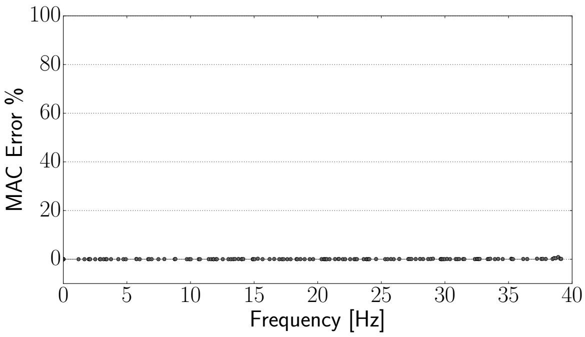

(d) No frequency limit

Figure 4.7: Effect of an imposed frequency limit on the POD input modes on the MAC error for all modes of the Elevator Outer Bracket FC test case

4.2.5. POD modes truncation

The POD decomposition will result in a mode set with an equal number of modes as given in the input. This will be an excess amount of modes and a truncation has to be applied selecting only the first r number of modes. Commonly, the eigenvalues of the resulting POD modes are used as truncation parameter [8, 35]. As explained in Section 2.6, the POD eigenvalues are a measure for the relative information content of the resulting POD modes. Therefore only r number of POD modes are retained such that the cumulative relative information content, as computed in equation 2.77, becomes approximately 1. The relative information content of the first 136 POD modes is shown in the top plot of Figure 4.8. The bottom plot shows the cumulative relative information content (the graphical form of equation 2.77). According to this method 99.9% of the cumulative information content is reached by 122 modes (108 POD modes + 14 rigid-body and control modes).

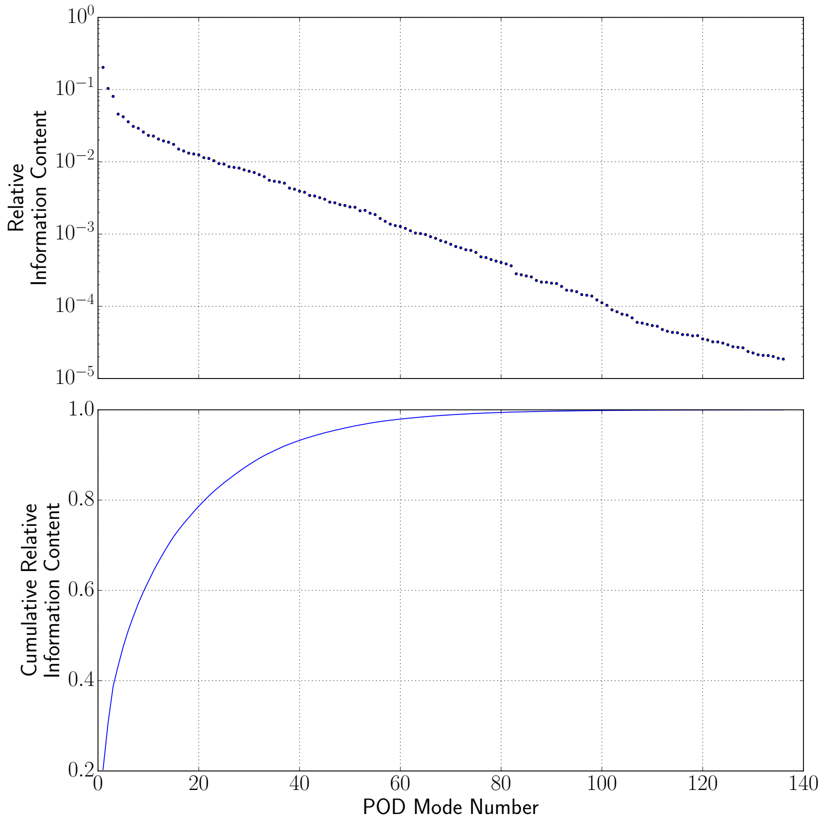

Figure 4.8: (Cumulative) relative information content of the resulting POD mode set

The error criteria were also computed for different truncation values, as shown in Figure 4.9. The approximation error reduces if more modes are added to the reference. A significant number of modes is needed for the error criteria to reduce below the thresholds defined in the previous chapter and shown in Appendix C. For the MAC error 130 modes are needed to decrease the error to 0.54%, for the aero-weighted MAC error 140 modes are needed to decrease the error to 0.71% and for the relative GAF Error 150 modes are needed to decrease the error to 3.5%. The conventional method looking at the relative information content estimated the truncation at 122 modes for an information content of 99.9%. Therefore it could be argued that for this new application of the POD method it is more conservative to look at the error estimators rather than estimating the truncation based on the relative information content.

This study will apply 136 POD modes decomposed out of the natural modes selected for the POD input, together with the 14 rigid-body and control modes. This makes a total of 150 modes, an equal amount, and thus computational time, as the other reference selection method. This enables a clear comparison of the performance of both methods for an equal computational cost.

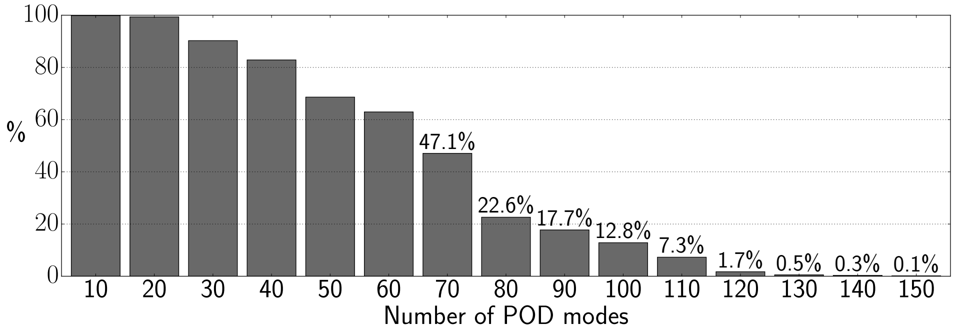

(a) MAC Error

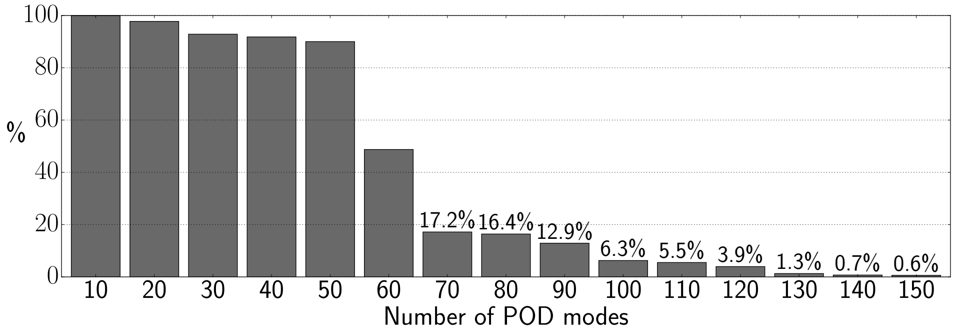

(b) Aero-Weighted MAC Error

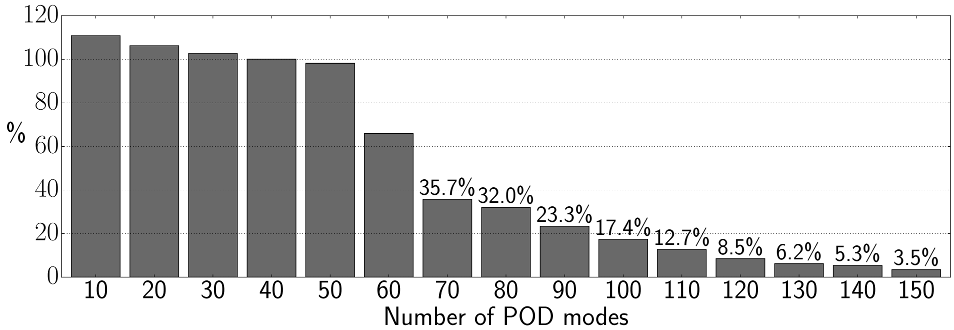

(c) Relative GAF Error

Figure 4.9: Average error estimators of the test cases for different POD truncation levels

Table 4.2 concludes the discussion of the reference set selection by giving an overview of the two chosen sets. Their performance for four test cases is presented in the next section.

Table 4.2: Overview of the modal basis reference sets

	Modes obtained from:
Method 1: Nominal structure reference set	Elastic modes of a nominal structural lay-out for one predefined mass distribution.
Method 2: POD-based reference set	Proper orthogonal modes decomposed out of an input set of 2176 input modes belonging to 16 different dynamic structural cases (16 input cases x 136 natural modes = 2176 input modes). These input modes were max. normalized and only the manually selected LSQ nodes were used for the mode representation.

4.3. Test case results

This section will show the effect of the two reference selection methods on the frequency and damping curves for the four different test cases; a nominal structure case, a failure case of the elevator outer bracket, a failure case of the aileron outer bracket and a failure case of the rudder outer bracket.

4.3.1. Nominal structure

The first test case is the nominal, unaltered structural lay-out. The considered load case is different from the one used by method 1 for the reference selection. In Figure 4.10 is shown that the error estimators for both methods are well below the quality thresholds (indicated by the red line). Both methods should therefore give satisfactory results for the frequency and damping curves.

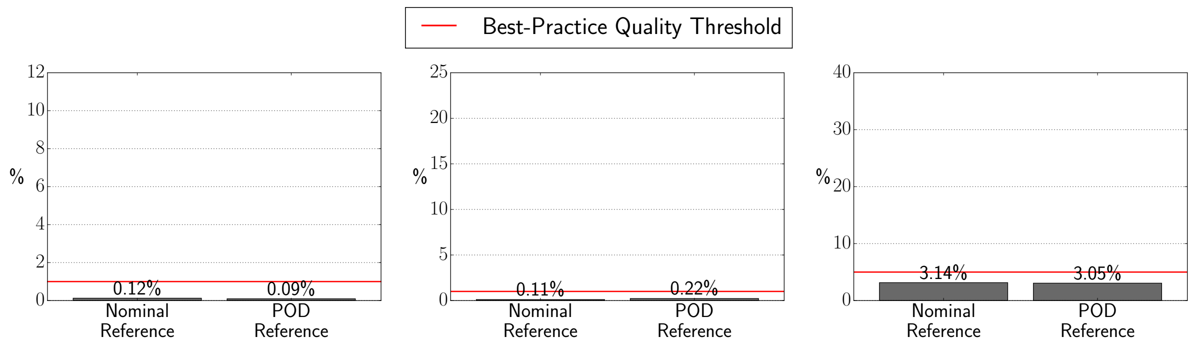

(a) MAC Error (b) Aero-Weighted MAC Error (c) Relative GAF Error

Figure 4.10: Comparison of error estimators for the nominal structure flutter computation with 1) Nominal structure reference and 2) POD reference

A selection of the frequency and damping curves is shown in Figure 4.11. These four modes were selected based on the largest observed deviations either in frequency or damping. No notable disagreements with direct aerodynamics were observable for all other modes. Mode 17 and 60 show small deviations in the damping with the POD reference basis and modes 20 and 45 show small deviations with the nominal reference basis. However, overall the approximation with both reference methods is in excellent agreement with the direct aerodynamics. So, both methods could indeed be used satisfactorily for this flutter computation as predicted by the error estimators.

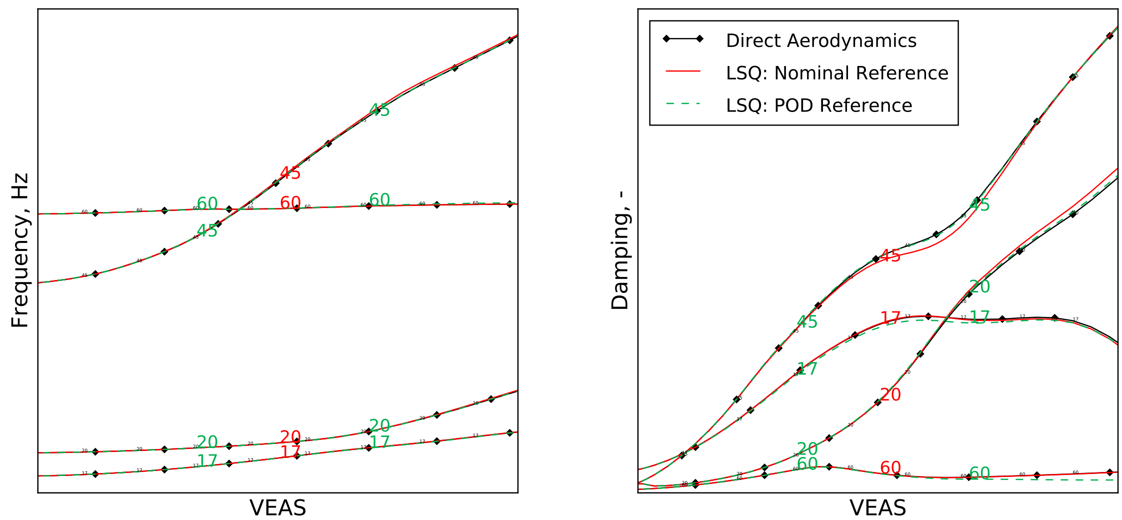

Figure 4.11: Frequency and damping progression for a nominal structure flutter computation with direct aerodynamics, LSQ with the nominal structure reference set and LSQ with the POD-based reference set

4.3.2. Elevator Outer Bracket FC

The error estimators for the Elevator Outer Bracket FC are shown in Figure 4.12. As already discussed in depth in the previous chapter, using only the nominal structure reference modes does not suffice for this failure case. The predicted errors are well above the defined thresholds. The POD reference, however, is for all criteria below the threshold.

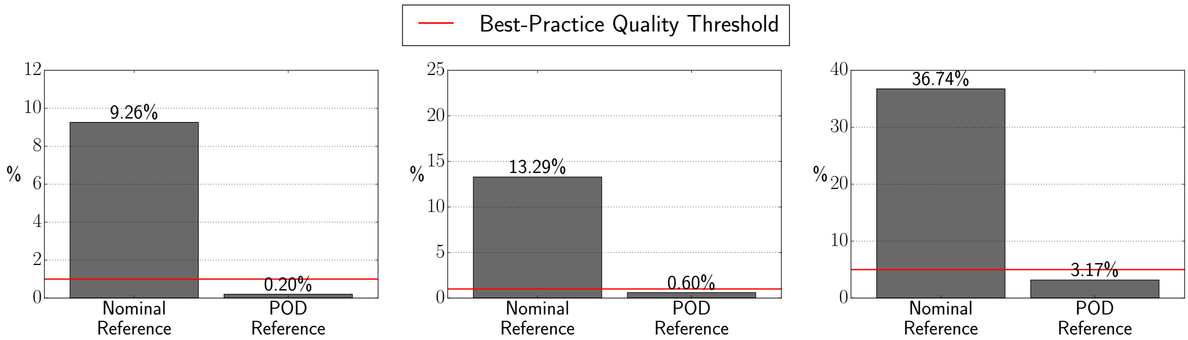

(a) MAC Error (b) Aero-Weighted MAC Error (c) Relative GAF Error

Figure 4.12: Comparison of error estimators for the Elevator Outer Bracket FC flutter computation with 1) Nominal structure reference and 2) POD reference

The comparison of the frequency and damping curves with direct aerodynamics in Figure 4.13 confirms the results of the error estimators. Large deviations with respect to the direct aerodynamics are visible for the nominal structure reference method. On the other hand, the results with the POD reference are in excellent agreement with the direct aerodynamics. The extra information on the elevator bracket failure case, which was in the POD input, is thus well represented in the final POD-based reference set and therefore the approximation error is eliminated.

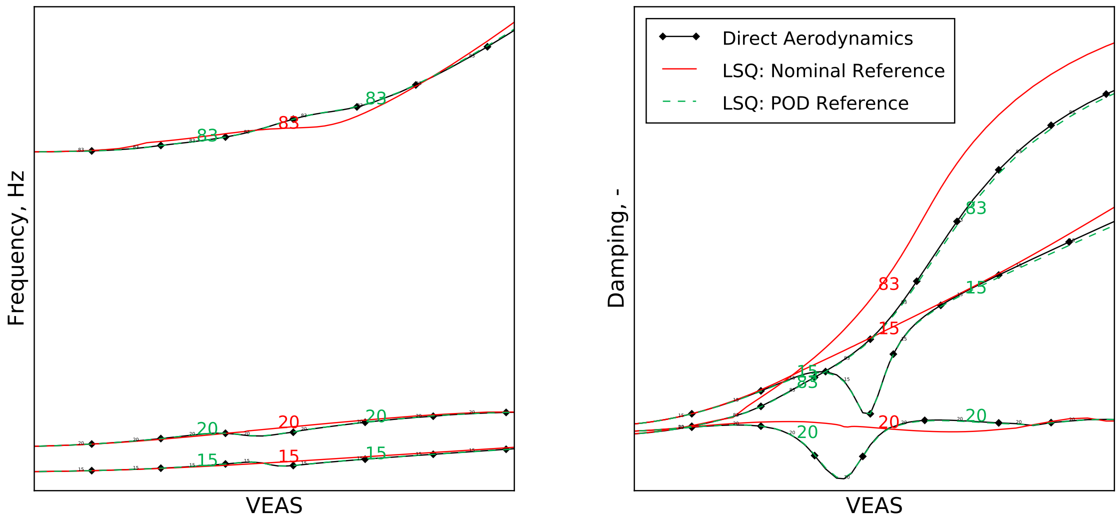

Figure 4.13: Frequency and damping progression for the Elevator Outer Bracket FC with direct aerodynamics, LSQ with the nominal structure reference set and LSQ with the POD-based reference set

4.3.3. Aileron Outer Bracket FC

The third test case is the rupture of the outer bracket of the outer aileron. The error estimators for both reference selection methods are shown in Figure 4.14. The predicted error with the nominal reference is larger than the POD reference for all quality estimators. Moreover, the nominal reference does not meet the best-practice quality threshold for the aero-weighted MAC and the relative GAF Error. The best-practice POD does meet all quality thresholds.

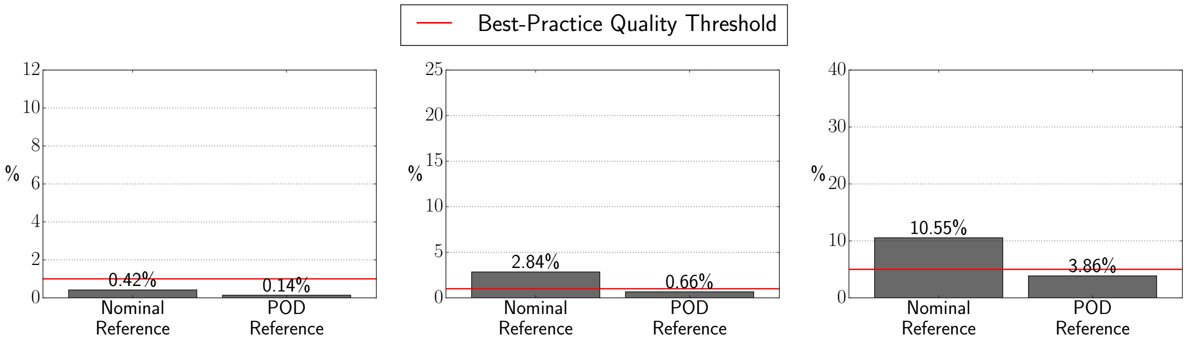

(a) MAC Error (b) Aero-Weighted MAC Error (c) Relative GAF Error

Figure 4.14: Comparison of error estimators for the Aileron Outer Bracket FC flutter computation with 1) Nominal structure reference and 2) POD reference

Figure 4.15 shows the frequency and damping curves for the Aileron Outer Bracket FC flutter computation. Again, the presented modes were selected manually, based on the deviations from the direct aerodynamics observed in the frequency and damping curves. The POD reference method produces frequency and damping curves with negligible deviations with respect to the direct aerodynamics. More significant deviations are seen with the nominal structure reference method. Especially for modes 63 and 72 these deviations are clear both in frequency and damping. Both these modes have a strong deformation of the ruptured aileron, as visualized in Figure 4.16. Mode 63 is a symmetrical outer aileron rotation mode and mode 72 is a non-symmetrical mode with a differential rotation of the inner and outer aileron of the left wing. The mode approximation error for modes 63 and 72 with both reference selection methods is visualized in Figure 4.17 and 4.18, respectively. The nominal structure reference method causes a bad mode approximation around the location of the ruptured bracket position, which has a similar appearance for both modes. This error does not exist with the POD-based reference set.

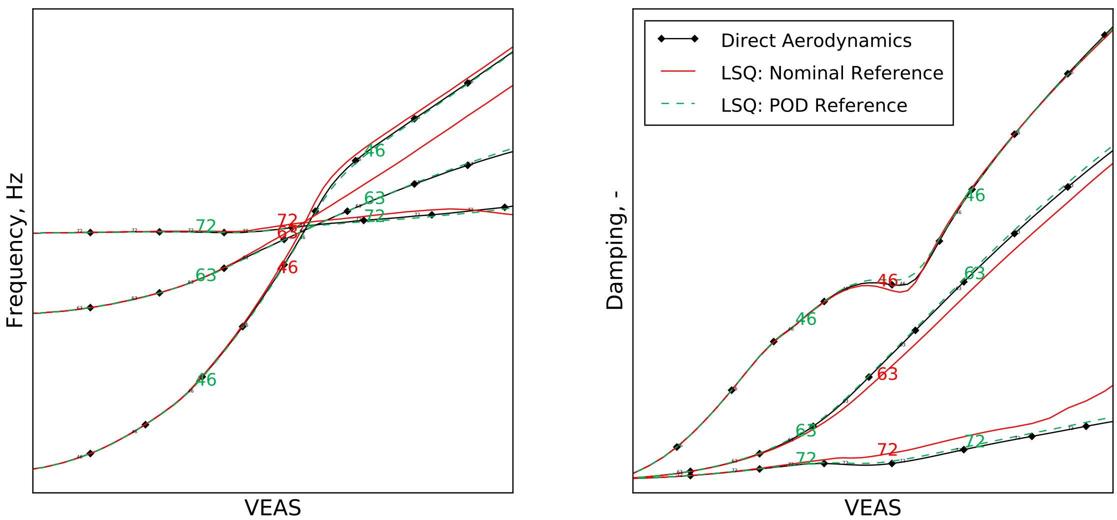

Figure 4.15: Frequency and damping progression for the Aileron Outer Bracket FC computation with direct aerodynamics, LSQ with the nominal structure reference set and LSQ with the POD-based reference set

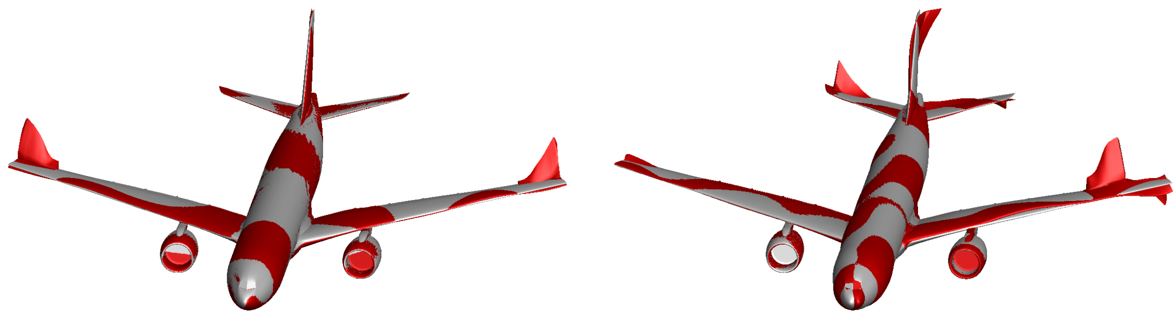

(a) Mode 63 of the Aileron Outer Bracket FC: Outer aileron rotation

(b) Mode 72 of the Aileron Outer Bracket FC: Differential rotation of left wing inner and outer aileron

Figure 4.16: Visualization of mode 63 and mode 72 of the Aileron Outer Bracket FC. Detailed figures available in Appendix D

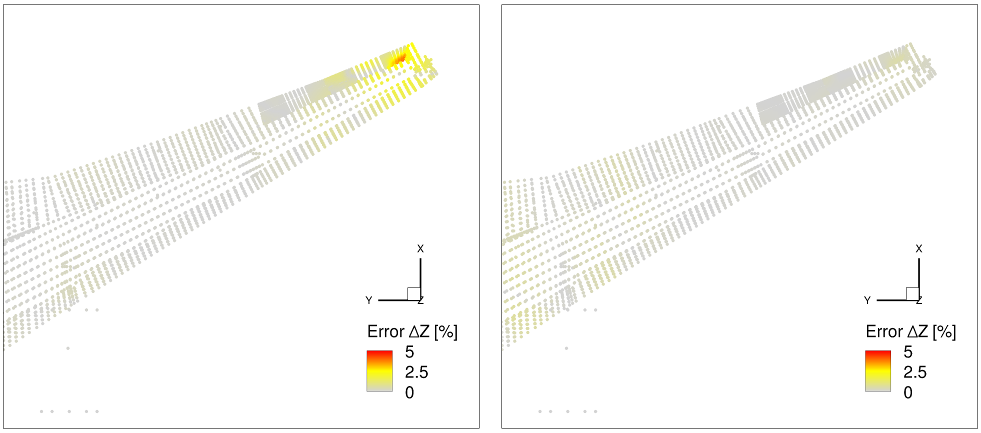

(a) Nominal reference

(b) POD reference

Figure 4.17: Mode approximation error of mode 63 of the Aileron Outer Bracket FC with different reference sets

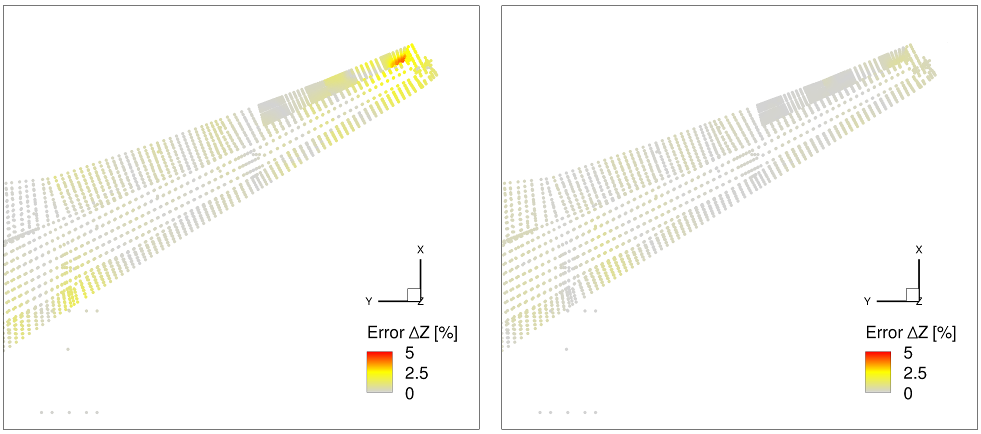

(a) Nominal reference

(b) POD reference

Figure 4.18: Mode approximation error of mode 72 of the Aileron Outer Bracket FC with different reference sets

It is clear that the approximation error is caused by missing information in the reference set due to the failure case. In Section 3.5 it was shown that this approximation error for the Elevator Outer Bracket FC could be solved by enrichment of the modal basis. The enrichment technique is now also applied for this failure case. The four enrichment methods presented in Section 3.5 performed equally well. Here, method 1 is applied to define the enrichment mode: the failure case mode with the highest MAC error is added to the reference. The resulting frequency and damping progression are shown in Figure 4.19. The approximation error vanishes for all modes, which confirms the results seen in Section 3.5. This shows again that the modal basis enrichment can be applied effectively (the error is almost completely removed) and efficiently (only one mode has to be added to the reference).

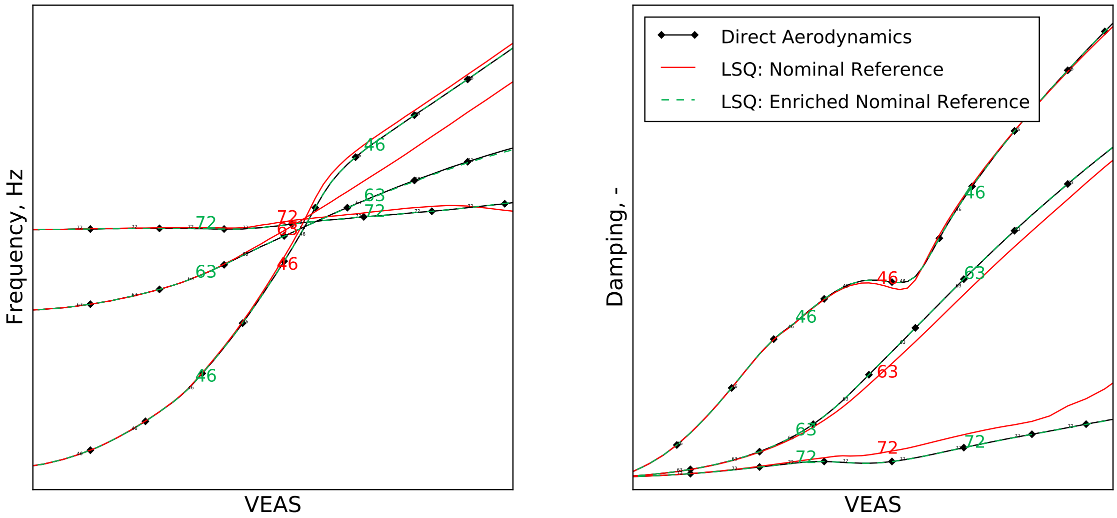

Figure 4.19: Frequency and damping progression for the Aileron Outer Bracket FC computation with direct aerodynamics, LSQ with the nominal structure reference set and LSQ with the enriched nominal structure reference set

4.3.4. Rudder Outer Bracket FC

The error estimators for the Rudder Outer Bracket FC are shown in Figure 4.20. All estimators indicate a bad mode approximation with the nominal reference set, exceeding the best-practice threshold largely. The POD reference method performs better, but also exceeds the threshold for the aero-weighted MAC criteria slightly.

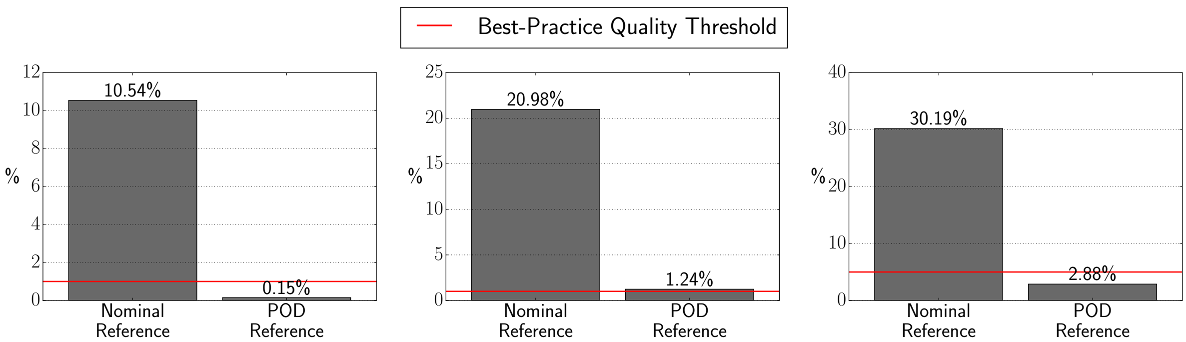

(a) MAC Error (b) Aero-Weighted MAC Error (c) Relative GAF Error

Figure 4.20: Comparison of error estimators for the Rudder Outer Bracket FC flutter computation with 1) Nominal structure reference and 2) POD reference

The frequency and damping progression for this failure case are shown in Figure 4.21. The approximation through the POD reference is in good agreement with the direct aerodynamics, only minor deviations can be noted for modes 16, 19 and 43. Contrary, large deviations with respect to direct aerodynamics are seen with the nominal reference for all presented modes, especially significant deviations are seen for mode 26 and 31, both in frequency and damping. These modes have a large rudder deflection, as shown in Figure 4.22. The nominal reference set is not capable of approximating these failure case modes accurately enough. This is confirmed by the mode approximation errors of these modes for both the POD reference and the nominal reference, as visualized in Figure 4.23 and 4.24.

Large mode approximation errors around the location of the ruptured rudder bracket are observed with the nominal reference, while these errors are non-existent with the POD-based reference.

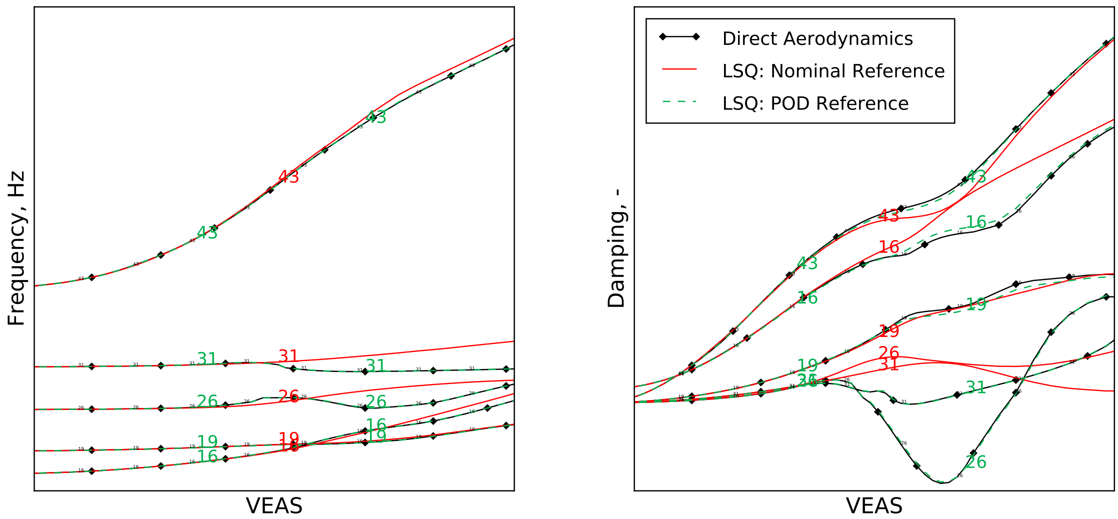

Figure 4.21: Frequency and damping progression for the Rudder Outer Bracket FC computation with direct aerodynamics, LSQ with the nominal structure reference set and LSQ with the POD-based reference set

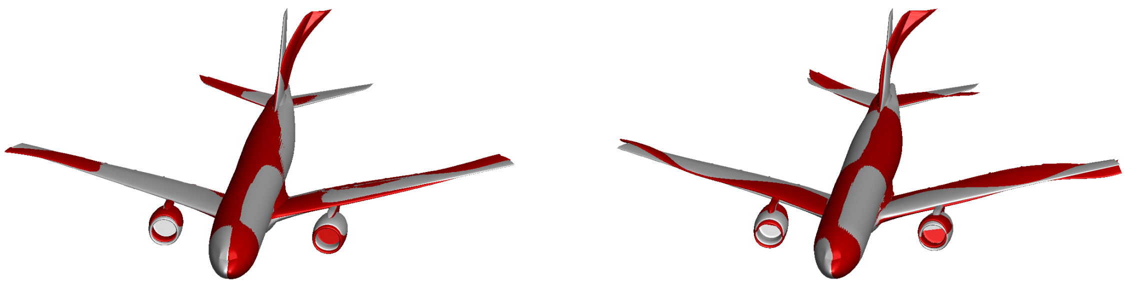

(a) Mode 26: VTP bending

(b) Mode 31: VTP bending combined with 3n HTP and wing torsion

Figure 4.22: Visualization of mode 26 and mode 31 of the Rudder Outer Bracket FC. Detailed figures available in Appendix D

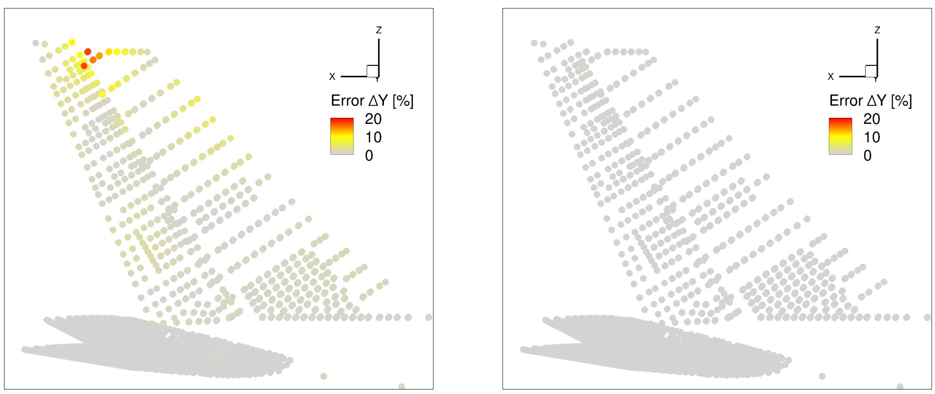

(a) Nominal reference

(b) POD reference

Figure 4.23: Mode approximation error of mode 26 of the Rudder Outer Bracket FC with different reference sets

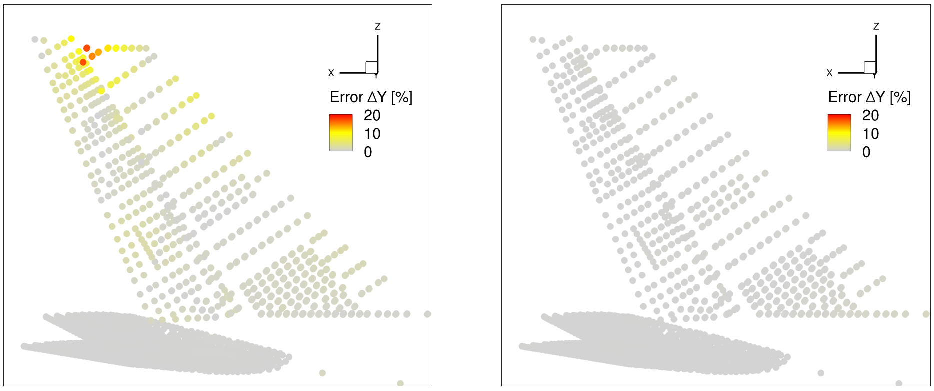

(a) Nominal reference (b) POD reference

Figure 4.24: Mode approximation error of mode 31 of the Rudder Outer Bracket FC with different reference sets

The modal basis enrichment method is applied again to remove the approximation error with the nominal reference set. The failure case mode with the highest MAC error is added to the reference. Again, the approximation error is removed efficiently as shown in the frequency and damping curves in Figure 4.25.

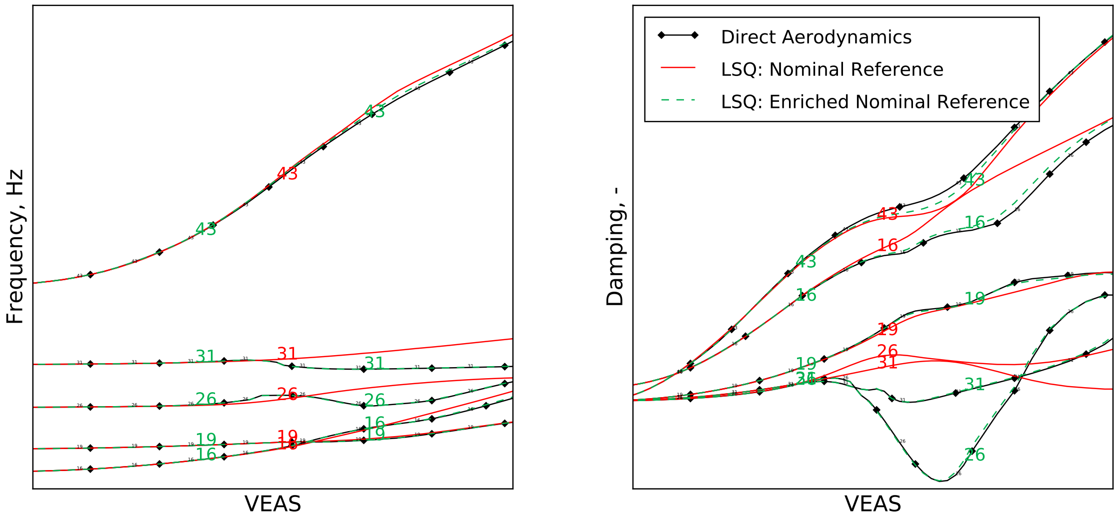

Figure 4.25: Frequency and damping progression for the Rudder Outer Bracket FC computation with direct aerodynamics, LSQ with the nominal structure reference set and LSQ with the enriched nominal structure reference set

4.4. Implementation POD method in an industrial process

This section discusses the implementation of the POD method in the high-fidelity unsteady aeroelastic simulation process in industry. One parameter which is still to be defined is the selection of the input cases if the POD reference basis has to represent the full flutter computational space, spanning all mass and failure cases. For the test case scenario the input cases were manually chosen in order to represent the test cases dominantly in the POD. As mentioned in Section 4.2.1, for each test case related to a structural failure (elevator, aileron, rudder) 3 input cases were used on a total of 16 input cases. So, approximately 20% of the considered input case modes belonged to each of these failure cases. Hence, the considered deformations specific for these failure cases were dominantly present in the resulting POD reference set. However, all considered failure cases (generally in the order of 100 FC's) have to be included in the POD input for the full flutter computational space. Each of these cases will therefore have a lower weight and be less prominently represented in the reference set. Figure 4.26 demonstrates these observations. This figure shows the MAC error criterium of the four test cases for POD reference sets with different input case selections. The green bars are the results of the POD reference set which was shown in the previous sections. The ratio between the failure case (FC) modes and the nominal case (NC) modes in the input is approximately 20%. As thoroughly discussed in the previous sections, this gives low mode approximation errors for all test cases. The blue bars show the results of a POD reference set where the failure case modes represent only 1% of the POD input modes. Correspondingly, the performance of this reference for the failure case simulations deteriorates. For the elevator FC it even exceeds the quality threshold. However, the results are still clearly better compared to the nominal reference set. Finally, the gray bars give the results for a third POD reference set where the failure case modes are completely removed from the POD input. This reference set performs equally poor as the nominal reference set for the failure case simulations, which indicates the necessity to include all failure cases in the POD input. This test shows the sensitivity of the POD reference set performance on the input case selection and it demonstrates the need for further investigations on an optimal input case selection for the full flutter computational space.

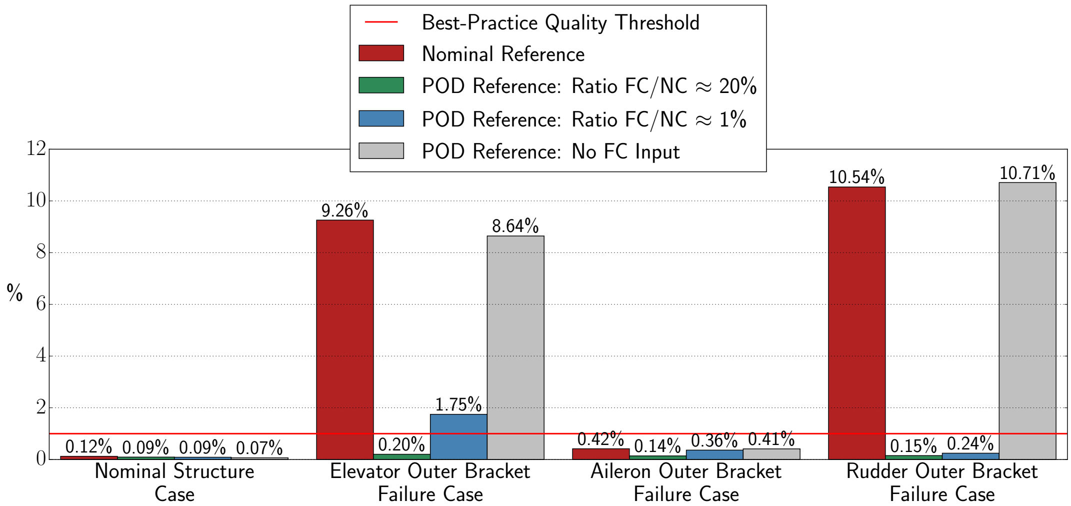

Figure 4.26: MAC error of the four test cases for different POD input case selections

The practical implementation of the POD-based reference selection method does not require major procedural changes. This is visualized in the updated process overview flowchart in Figure 4.27. All modal analysis runs required for the input production of the POD can be reused for the final flutter computations.

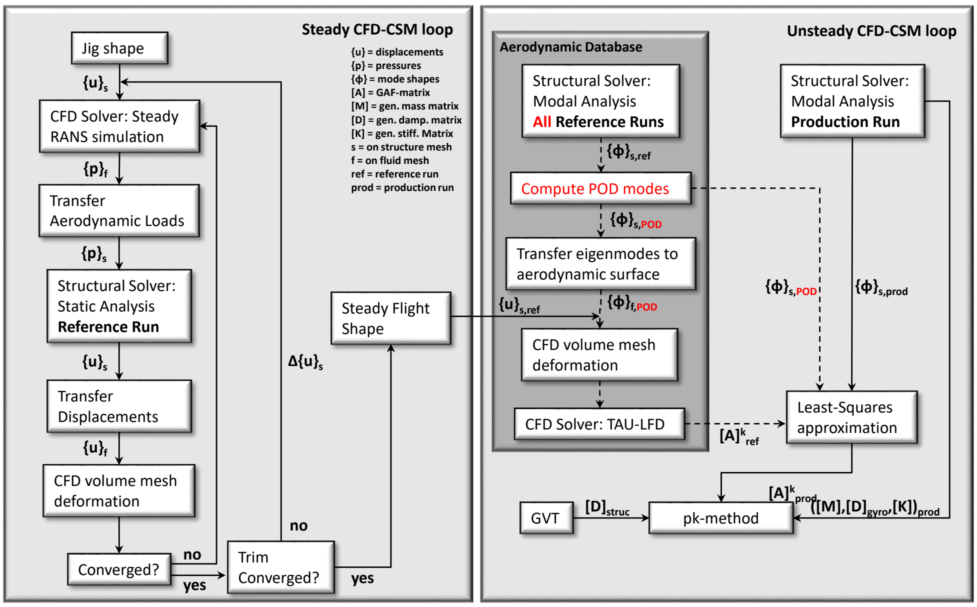

Figure 4.27: Flowchart of a full flutter calculation process with implementation of the POD-based modal basis reference selection

4.5. Conclusion

The study of the four test cases has shown that using a nominal reference set is justified for flutter computations of nominal structural lay-outs and failure cases which do not cause large local mode deviations. Only for some very specific failure cases with strong local deformations the purely nominal reference set is insufficient with respect to approximation errors. The modal basis quality criteria can detect these errors such that deviations in the frequency and damping curves can be prevented by enriching the reference modal basis.

The POD-based reference selection method has shown superior characteristics for these kind of critical failure cases. The mode approximation errors for all presented test cases are small, and correspondingly the frequency and damping curves match well with those made by direct aerodynamics. A prerequisite for the good performance of the POD method is a well-considered selection of the input cases giving information for all desired flutter computations and the appropriate set up of this reference considering which nodes, normalization, frequency limit and truncation to be used. Another advantage of the POD method is the opportunity for optimization of the reference selection in the future. More optimized normalization methods or input case selection could lead to even more accurate performance. For the four test cases the accuracy with 150 POD modes is high. It could therefore be expected that a decrease of the POD truncation is possible, which would reduce the computational cost accordingly.

Research question B posed in Section 1.2 can be answered when reviewing all results. Both methods can be used satisfactorily for unsteady flutter computations, but only when incorporating some prerequisites. For the nominal reference method the error estimation and modal basis enrichment scheme (as discussed in Chapter 3) have to be implemented to prevent errors for certain failure cases. For the POD-based reference method further analysis and optimization of the input case selection is required to make the method suitable for the full certification computational space.

5

Conclusions and Outlook

This thesis presents improvements on the unsteady aeroelastic simulation process with direct-CFD computation of the unsteady aerodynamics. For agreement with certification guidelines, flutter simulations have to be executed for a wide range of parameters covering all flight conditions and variations in the aircraft loading or structural lay-out. Due to the large parameter space, the unsteady aerodynamic computation for these aeroelastic simulations requires a low computational cost while retaining accuracy in predicting transonic flow phenomena such as shocks and separation. Recently, a high-fidelity, time-linearized CFD method was introduced in the flutter simulation procedure. This method offers the inherent quality to represent the important unsteady flow phenomena in the transonic regime while providing a spatially more detailed flow representation. Considering the computational cost constraint, the unsteady aerodynamics can only be computed for a limited number of elastic mode shapes, which are subsequently mapped to all 'production' computational cases. The error introduced in the frequency and damping curves due to bad approximations was not well understood. Therefore the research question of this thesis report reads:

How can the selection of aerodynamic reference modal basis be made more robust and accurate for usage of direct-CFD methods in unsteady aeroelastic simulations?

This research question has been assessed analyzing two topics. An error estimation study quantified the impact of the approximation error on the frequency and damping curves and a comparative study of two reference modal basis selection methods demonstrated their performance for four flutter simulations.

In the error estimation study a range of quality criteria was established and their performance was assessed on the basis of a test case. All presented error estimators, even global mode quality criteria, proved to be good indicators for the quality of the reference set. This disproved the hypothesis that local mode approximation errors would be averaged out for these global mode quality criteria. In addition, a modal basis enrichment method was provided which can be applied if the error estimators indicate an insufficient modal reference set. This enhancement can be done automatically and proved to be effective and efficient. Adding one single mode sufficed to obtain an excellent agreement with the direct aerodynamic approach. The knowledge obtained in this study can be used to assess the quality of the reference modal basis set for all flutter certification computations without further implementation requirements. Furthermore, the re-computation of the unsteady aerodynamics can be prevented for every update of the structural modeling.

The second topic evaluated the performance of two reference selection methods for the flutter computation of four test cases. The first method uses the elastic modes of a nominal structural model at one predefined mass case as a reference, while the second method applies the POD (Proper Orthogonal Decomposition) theory to decompose a wide range of modes for different failure and mass cases into a reference set. Using the elastic modes of a nominal structure as a reference proved to be sufficient for the flutter computation of nominal structural lay-outs and failure cases which do not deviate strongly from these nominal structural modes. This makes up the majority of the flutter computational space. Mode approximation errors arise only for specific failure cases which introduce local deformations not represented in the nominal mode set. However, the error estimators have shown to predict these approximation errors, such that their impact on the frequency and damping curves can be prevented by modal basis enrichment. The POD-based reference set proved to be accurate for all test cases with only minor deviations in the frequency and damping curves due to the approximation error. The prerequisite for a good performance of the POD method is a well-considered selection of the input cases and the appropriate set up of this input considering which nodes, normalization, frequency limit and truncation to be used.

Based on the presented findings and conclusions a recommendation can be made for further investigations on this topic. Throughout this report the same least-squares method was used for approximating unsteady aerodynamic forces. The modes in this approximation are represented by the degrees of freedom of manually selected nodes. The expected error due to this selection of nodes is small, however some further improvements are still possible which could lead to a more accurate and/or more automated procedure. The mapping of the unsteady aerodynamics should be based on the mode shapes on the CFD surface, but the modes can only be described on the structural grid due to computational constraints. Using the structural fluid-structure coupling nodes is not optimal, as shown in the report. However, this could be improved by applying an automatic weighting function based on the interpolation of the structural node displacements to the CFD surface. The proposed area-weighting was a good first step, but there are further influential parameters which could be introduced. One example is the distance of the structural node to the interface. Rotational deformations of nodes which are located far from the interface lead to large deformations at this interface. The distance of the structural nodes to the interface could therefore be incorporated in the weighting. Alternatively, the LSQ approximation could be enhanced by a component-wise division of the aircraft. For example, the production aerodynamics of the wings can be approximated from the reference by only looking at their relative mode shapes. The additional difficulty with this method is the non-orthogonality of the reference when considering the aircraft components independently. This can give numerical issues which have to be addressed. Furthermore, component interaction aerodynamics is neglected for this method. A trade-off should therefore be made between the benefits of a reduced computational cost and an improved mode approximation and the reduced modeling accuracy due to the neglect of this component interaction aerodynamics.

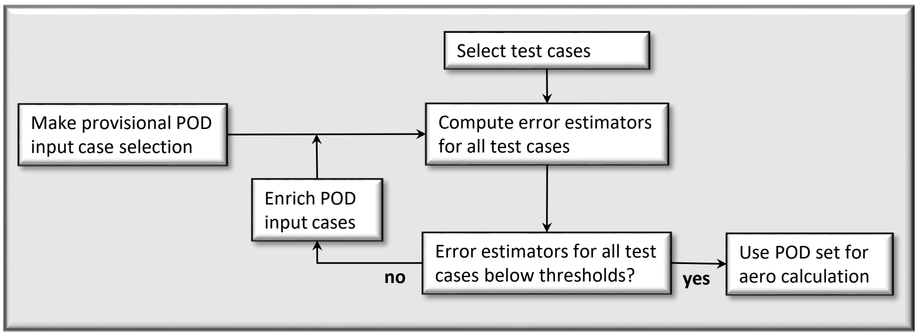

Figure 5.1: Flowchart of a proposed POD input case selection optimization.

Moreover, further improvements on the POD-based reference selection method could be achieved in multiple ways. First, in order to prepare the method to be used for the full flutter computational space, an additional study is needed on the most optimal input case selection. For the presented scenario with only four test cases this could be done by manually selecting the input cases belonging to each of these four computational cases. For the full computational space, however, more attention has to be paid on the representation of all desired cases in the input. A possibility could be an automated near-random sampling of the mass and failure cases based on statistical methods, such as latin hypercube sampling. Further improvement could be an automated optimization of the input case selection. An example how this could work is illustrated in Figure 5.1. A provisional POD input case selection is made and the resulting POD reference set is used to compute the error estimators for predefined test cases. Based on the error estimation, the modes of the test cases with the poorest approximation can be added to the POD input. This will make these specific modes more dominant in the resulting POD reference set and

enhance their approximation. This loop can be repeated until satisfactory error estimators for all test cases. Besides this, the normalization of the input modes showed promising opportunities for further development. Critical modes could be favored by giving them a higher norm through a weighting factor or an aero-weighted algorithm could be foreseen to favor the aircraft surfaces with a high magnitude of the unsteady aerodynamics and corresponding high influence on the GAF matrix.
Besides a better mapping of the reference aerodynamics, other improvements on the implementation of the high-fidelity LFD should be considered as well. One example is the trim condition of the steady reference aerodynamics. Currently, these steady reference aerodynamics are computed for a single trim case, independent of the considered mass case of the flutter computation. A possibility is the computation of the unsteady reference aerodynamics for a small number of steady flight conditions for the given modal reference set, followed by an interpolation to the considered mass case of the flutter computation. A trade-off has to be made between the additional computational cost and the increased modeling accuracy.

A
Structural Sensitivity Study

The recent transition from low-fidelity DLM aerodynamics to the high-fidelity LFD method opened the question whether the available dynamic structural model fidelity is satisfactory in combination with a high-fidelity aerodynamic model. The first research topic therefore examined whether it is possible to increase the accuracy of the unsteady aeroelastic simulations by improving the dynamic structural model. This chapter will show a study on the sensitivity of dynamic structural modeling alterations on the unsteady aeroelastic results.
This research topic was triggered by a specific case which emerged during a validation process with the new aeroelastic simulation setup. During this validation process a deviation between the FVT measured frequency and the theoretical model was observed for the 3-node bending mode of the HTP. Due to the recently improved aerodynamic modeling, the source for this deviation was hypothesized to be modeling imperfections of the structural finite element model. This case will form the test subject for the sensitivity study. The question for this test subject therefore reads: Are there dynamic structural model sensitivities which could explain the deviation between the theoretical model and FVT results? These sensitive parameters could point to imperfections in the dynamic structural model which could be improved to lead to an overall more accurate aeroelastic simulation.

A.1. Case description

The results of the flight vibration test (FVT) and the theoretical model are shown in Figure A.1. From the top down, the frequency curves are given for the 2-node, 3-node and 4-node HTP bending modes, respectively. The theoretical model is in good agreement with the flight test for the 2-node and 4-node bending modes, but a deviation of approximately 1 Hz (10%) can be seen for all measurement points for the 3-node HTP bending mode. The goal of this study is thus to find a sensitivity which could explain this deviation, i.e. find a structural parameter which affects the frequency of the 3n bending mode significantly and does not adversely affect the other modes. The sensitivity on all HTP related modes was considered, but only the results for the 2n, 3n and 4n HTP bending modes will be shown. These modes are visualized in Figure A.2.

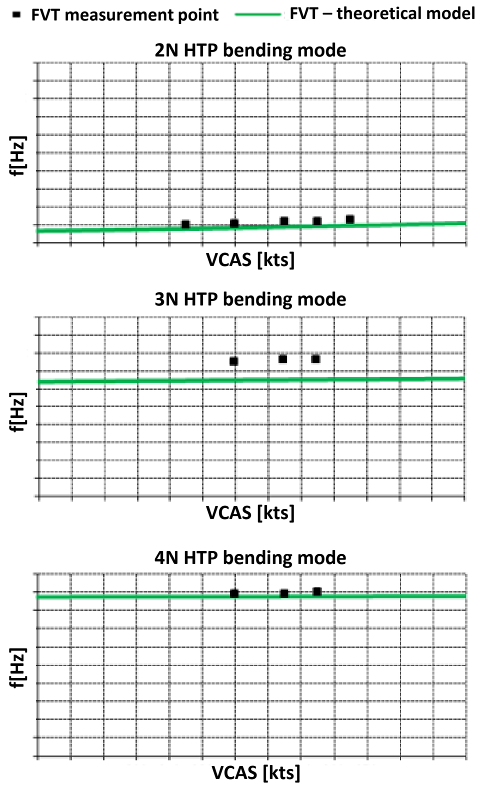

Figure A.1: Comparison of observed and predicted frequency between FVT (black dots) and theoretical model (green line). Top plot: 2-node HTP, Middle plot: 3-node HTP, Bottom plot: 4-node HTP. Horizontal grid spacing = 10kts, Vertical grid spacing = 1 Hz. (Property of Airbus GmbH)

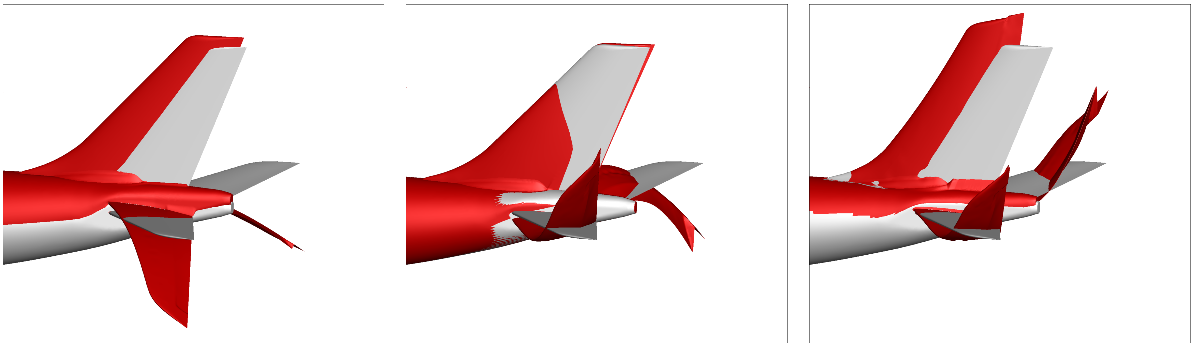

(a) 2n HTP (b) 3n HTP (c) 4n HTP

Figure A.2: Visualization of the 2n, 3n and 4n HTP bending modes

The theoretical structural model is a detailed, full aircraft finite element model. This model was validated with a Dynamic Ground Test (DGT) and a specific high-frequency HTP Ground Vibration Test (GVT). The model was tuned to match the GVT results as close as possible in the fully loaded configuration. The sensitivity of multiple structural parameters will be shown. Firstly, global stiffness variations in the HTP and elevator modeling were considered. These variations were introduced in the model through a tuning bar, a condensed beam model representative of the global stiffness characteristics of the full finite element model. The procedure to establish this tuning bar is shown in Appendix B. The vertical bending stiffness will be altered in this manner for the full elevator and HTP and for the HTP inboard and outboard section independently, as indicated in Figure A.3. Similarly, torsional stiffness variations of the HTP and elevator will also be introduced through these tuning bars. Additionally, the impact of some local modeling imperfections was considered. The sensitivity of the modeling of both the HTP and elevator spars was investigated. Furthermore, also the effect of removing the trailing edge rigidity, a recently introduced model improvement, was tested. A full overview and motivation of the different structural sensitivity parameters is given in Table A.1.

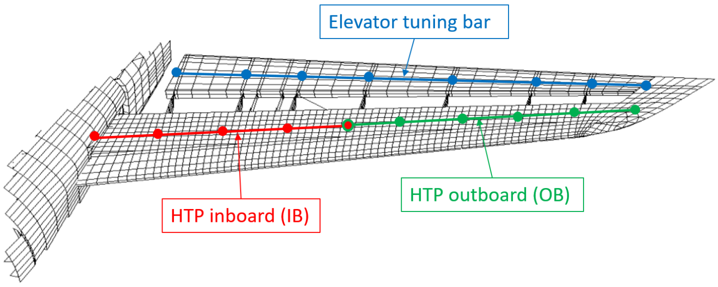

Figure A.3: Condensed structural model

Table A.1: Overview and motivation of sensitivity adjustments

Parameter	**Sensitivity range**	**Motivation**
	Global sensitivity adjustments	
HTP EI	+10%, +20%, +30%	Vertical bending stiffness variation over entire HTP.
HTP IB EI	+10%, +20%, +30%	Vertical bending stiffness variation over the inboard section of the HTP (see Figure A.3).
HTP OB EI	+10%, +20%, +30%	Vertical bending stiffness variation over the outboard section of the HTP (see Figure A.3).
HTP GJ	+10%, +20%, +30%	Torsional stiffness variation over entire HTP.
Elevator EI	+10%, +20%, +30%	Vertical bending stiffness variation over entire elevator.
Elevator GJ	+10%, +20%, +30%	Torsional stiffness variation over entire elevator.
	Local sensitivity adjustments	
HTP front/rear spar [HTP_FS / HTP_RS]	Double thickness dimension	Effect of HTP front and rear spar modeling. Modeling thickness of the spar is doubled as sensitivity input.
Elevator front spar [Elev_FS]	Double thickness dimension	Effect of Elevator front spar modeling. Modeling thickness of the spars is doubled as sensitivity input.
Elevator TE rigidity [Elev_TE]	TE rigidity elements removed	The last update to the structural model was an addition of springs at the TE of the elevator to make the TE behave more rigid, because non-physical shear deformation of the TE was noticed. The effect of this model improvement is tested by removing the stiffening elements. Note that this sensitivity is thus not an increased stiffness, but a removal of additional spring elements.

A.2. Effect on FVT-model frequency

The results of the sensitivity study on the frequency of the theoretical FVT model will only be shown at one velocity (345 kts) and relative to the frequency of the baseline theoretical model. The deviation between this baseline theoretical model and the test results is smaller than 2% for the 2n and 4n mode and approximately 10% for the 3n mode, as was shown in Figure A.1.

The sensitivity of the frequency results on the structural parameters is shown in Figure A.4. Different conclusions can be drawn from these results. The vertical stiffness variations of the HTP tuning bar have a relatively strong impact on the frequency. However, for a theoretical one degree of freedom spring-mass element the frequency would increase by approx. 5% by a 10% stiffness increase. The observed frequency increases of approximately 3% for the 2n and 3n bending modes are therefore within expected bounds. Another clear result is that the 2n HTP mode is only influenced by the inboard stiffness increase, which can also be expected since this is the region where most of the strain energy is exerted for this mode. The same reason explains that stiffness variations outboard have a significant impact on the 3n mode, less impact on the 4n mode and a negligible effect on the 2n mode. This could therefore be an interesting parameter to explain the deviation with the FVT results. However, only a frequency increase of approx. 1.5% for the 3n HTP mode is computed for a 10% stiffness increase of the full outboard section of the HTP. The sensitivity of the HTP torsional stiffness and the elevator vertical stiffness are negligible for all modes. The elevator torsional stiffness, however, has a small, but notable negative effect on all modes. Both the front and rear HTP spars have the biggest impact on the 3n mode and a significant impact on the 4n mode. As could be seen in Figure A.2, these modes have next to a strong bending deformation also a significant portion of torsion, which is significantly affected by the HTP spars. The 2n mode, which shows almost pure bending deformation, shows a smaller sensitivity towards this parameter. The elevator front spar has a negligible impact on all modes. However, removing the rigid elements from the elevator TE does have an increasing impact on the frequency. Removing the TE rigidity will reduce the torsional stiffness of the elevator, therefore it is not surprising to see the opposite effect which could be seen for the increase in elevator torsional stiffness.

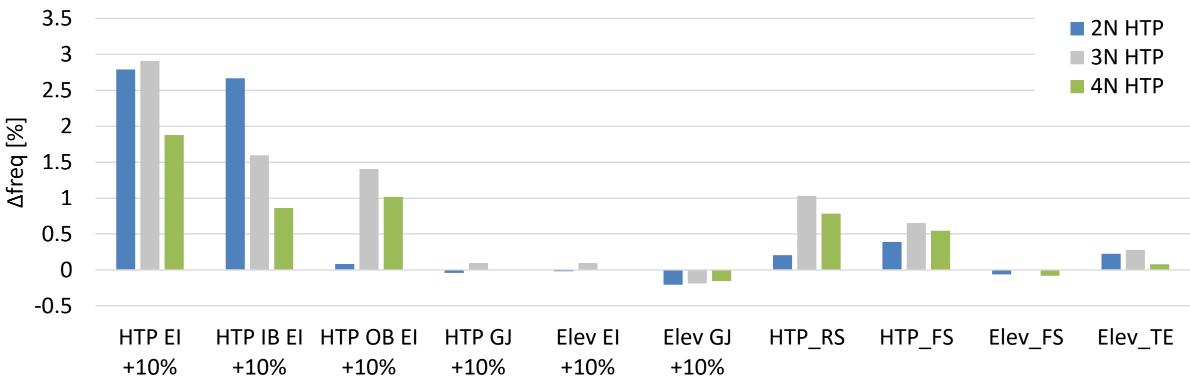

Figure A.4: Effect of structural parameters on frequency of 2n, 3n, and 4n HTP bending modes

In Figures A.5, A.6 and A.7 the effect of increasing the stiffness variations of the tuning bars in the HTP and elevator is shown for the 2n, 3n and 4n HTP modes, respectively. The most notable result here is the quasi linear effect of the stiffness variations for all modes and for all variations. This satisfies the idea that the observations made above do not change upon the strength of the sensitivity parameters, as long as the variations are kept within reasonable bounds. It is also interesting to see in Figure A.6 that none of the tested structural alterations would suffice to make the 3n HTP mode theoretical frequency match the FVT result, since therefore a 10% frequency increase would be needed. The tested model variations up to an increase of 30% stiffness achieve only frequency increases up to 5% for the 3N HTP bending mode. The hypothesis that the deviation could be attributed to local model imperfections of the dynamic structural model is rejected based on these findings.

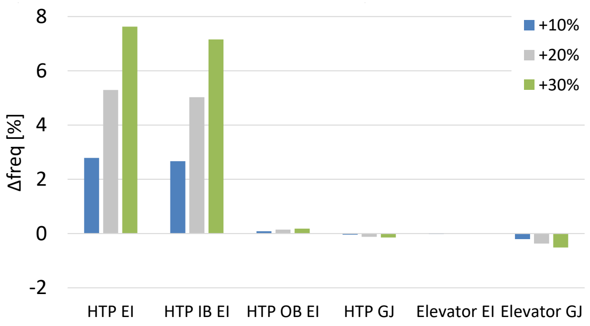

Figure A.5: Effect of structural parameter variations on 2n HTP bending frequency

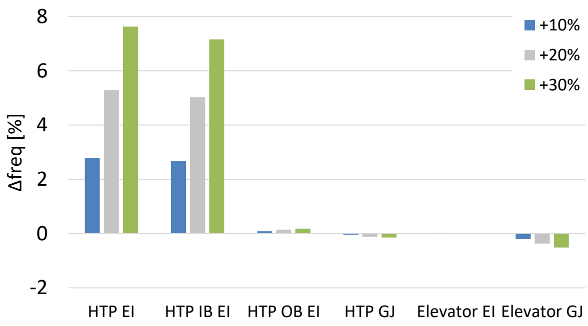

Figure A.6: Effect of structural parameter variations on 3n HTP bending frequency

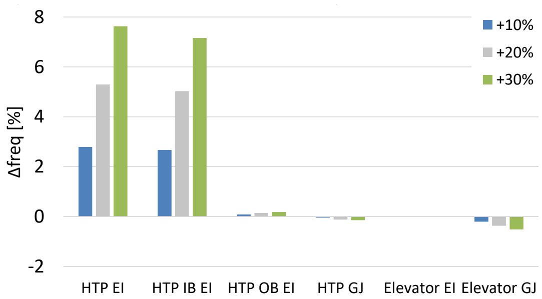

Figure A.7: Effect of structural parameter variations on 4n HTP bending frequency

A.3. Conclusion

The goal of the sensitivity study was to find structural modeling areas which could explain the deviation between the theoretical model and the FVT results for the 3n HTP mode frequency. Finding the root cause for this deviation could uncover imperfections in the dynamic structural model in relation with the new aerodynamic model.

The results showed that the sensitivity of global structural parameters such as the vertical and torsional stiffness in both HTP and elevator could not explain the deviation. Observed frequency sensitivities were within expected bounds. None of the investigated parameters affected the 3n mode significantly enough without having an impact on the other modes. Local model sensitivities for some areas of interest (HTP spars, elevator spars and TE) neither revealed significant imperfections in the model. The observed deviation between the theoretical model and the flight vibration test can therefore not be attributed to modeling imperfections in the dynamic structural model. The expected benefits in accuracy or robustness of the unsteady aeroelastic simulation for local improvements of the dynamic structural model are small. Local modeling improvements are therefore no further investigated in the scope of this thesis project.

B

Parameterization of the Structural Finite Element Model

In order to efficiently execute the structural sensitivity studies, the full finite element model has to be parameterized and reduced into a condensed model with a limited amount of nodes and degrees of freedom. The lifting surfaces of aircraft are for this purpose often represented as simple beam models. This methodology was used for the structural sensitivity studies of the HTP and Elevator. The procedure to condense the full finite element model is discussed here.

As a first step, the finite element model of the considered structural element is isolated. For the presented studies this was either the HTP box or the elevator. A static analysis (Nastran SOL101) is then performed, clamping the model at the root and applying known loads at the tip. The bending and torsional stiffness of the considered sections of the tuning beam can then be calculated using the standard beam equations.

B.1. Bending stiffness

The bending stiffness is found by applying a tip load and bending moment and solving for the relative rotation about the y-axis, as shown in figure B.1.

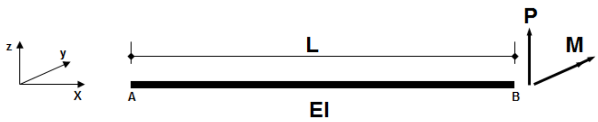

Figure B.1: Free-body diagram for determination of bending stiffness of the full finite element model

The relative rotation θ of a bending beam under the known tip force P and bending moment M can be computed according to:

$$\theta = \theta_B - \theta_A = \frac{ML}{EI} + \frac{PL^2}{2EI} \tag{B.1}$$

Rewriting for the unknown bending stiffness EI as a function of the known load components M and P and the length of the beam L gives following expression.

$$EI = \frac{ML + \frac{PL^2}{2}}{\theta} \tag{B.2}$$

B.2. Torsional stiffness

The torsional stiffness can be computed analogously by applying a known torque at the tip of the structural component and tracking the relative rotation around the x-axis, as visualized in figure B.2.

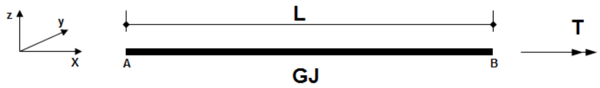

Figure B.2: Free-body diagram for determination of torsional stiffness of the full finite element model

The relative rotation θ is computed as:

$$\theta = \theta_B - \theta_A = \frac{TL}{GJ}, \tag{B.3}$$

with, T the applied torque, L the length of the beam and GJ the torsional stiffness. Rewriting for the unknown torsional stiffness then gives:

$$GJ = \frac{TL}{\theta}. \tag{B.4}$$

C

Thresholds for the Reference Modal Basis Quality Criteria

Table C.1 of the best-practice thresholds for all presented reference modal basis quality criteria. These thresholds were defined based on the test case presented in Chapter 3 and on the limited experience gained with other case studies.

Table C.1: Thresholds for the reference modal basis quality criteria

Quality Criterium	Best-Practice Threshold
Mode approximation errors	
MAC Error	1%
Mode Norm Error	5%
Local Mode Error	5%
Aero-weighted mode approximation errors	
Aero-Weighted MAC Error	1%
Aero-Weighted Mode Norm Error	5%
Aero-Weighted Local Mode Error	5%
Approximate GAF errors	
Relative GAF Error influenced mode	3%
Relative GAF Error excitation mode	5%
Relative GAF Error diagonal terms	5%

D

Detailed Mode Shape Figures

This appendix gives more detailed mode shape figures for those presented in this report. Note that the amplification factor on the modes is solely selected to give a clear visualization. Relating the magnitude of deformations between figures (e.g. of the error modes) is therefore not possible.

D.1. Mode shapes nominal structure test case

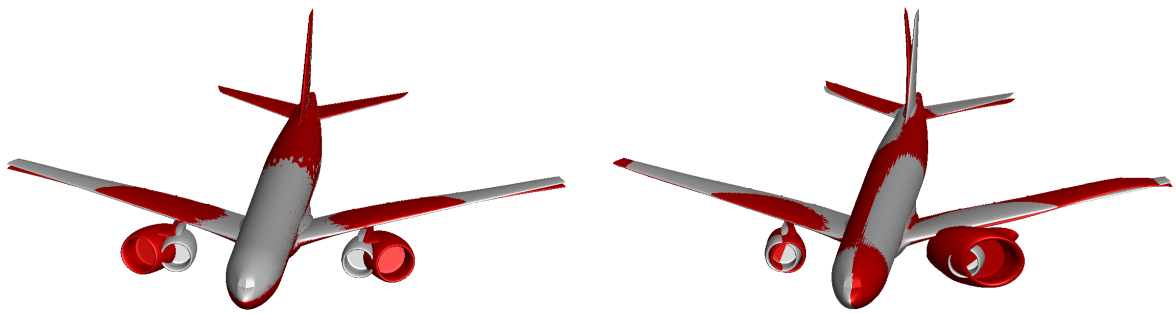

(a) Mode 9: Symmetric engine rotation

(b) Mode 22: Non-symmetric engine rotation

Figure D.1: Visualization of eigenmodes 9 and 22

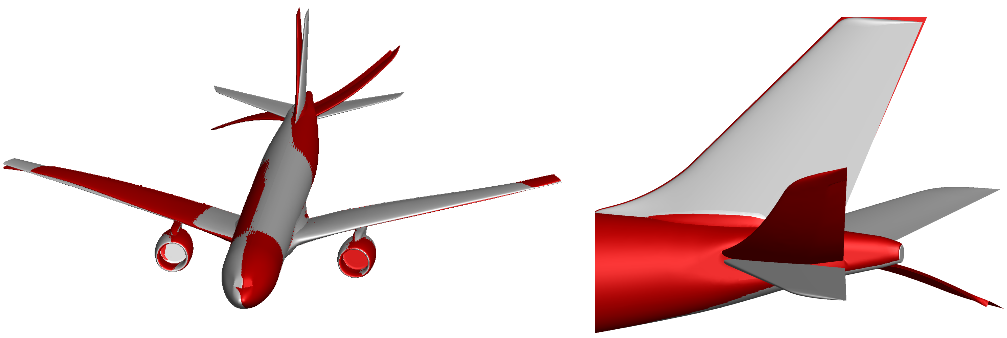

Figure D.2: Visualization of eigenmode 17: HTP roll

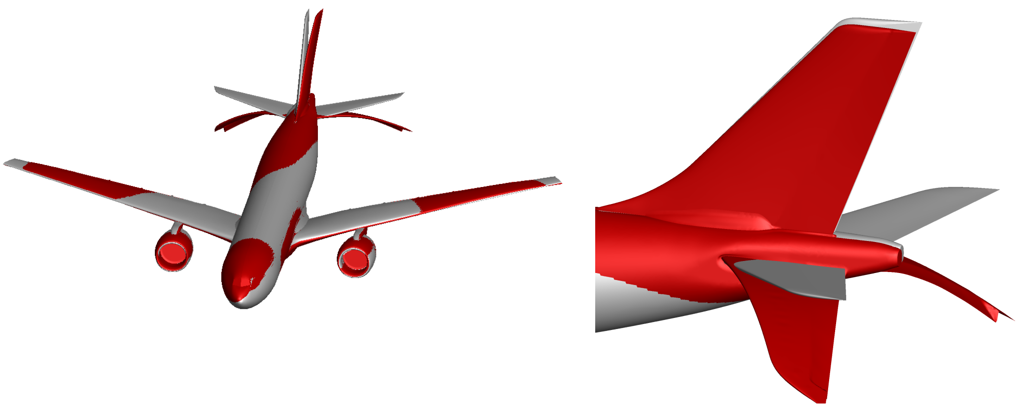

Figure D.3: Visualization of eigenmode 20: 2n HTP bending

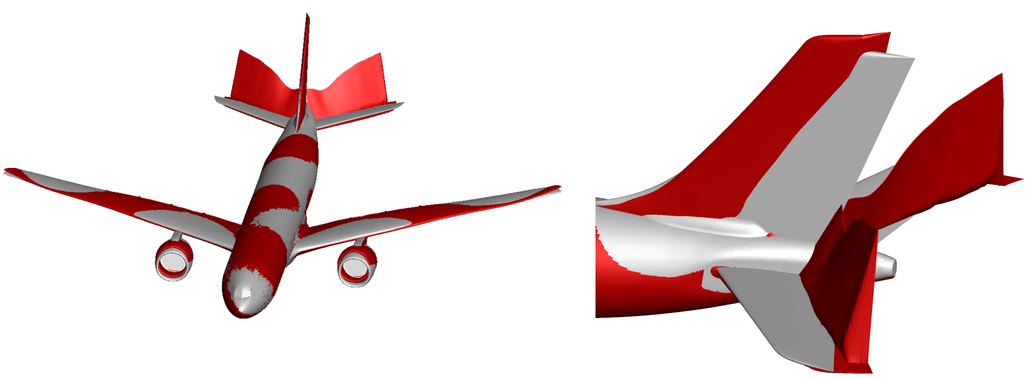

Figure D.4: Visualization of eigenmode 49: Symmetric elevator rotation

D.2. Mode shapes Elevator Outer Bracket FC

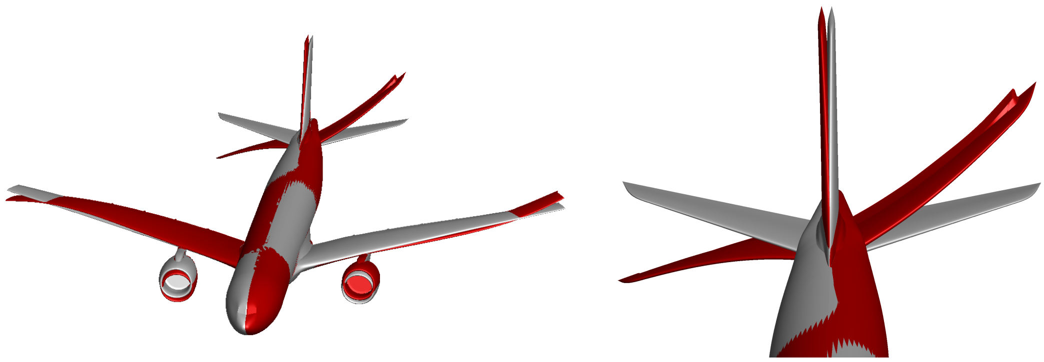

Figure D.5: Visualization of eigenmode 15: HTP roll

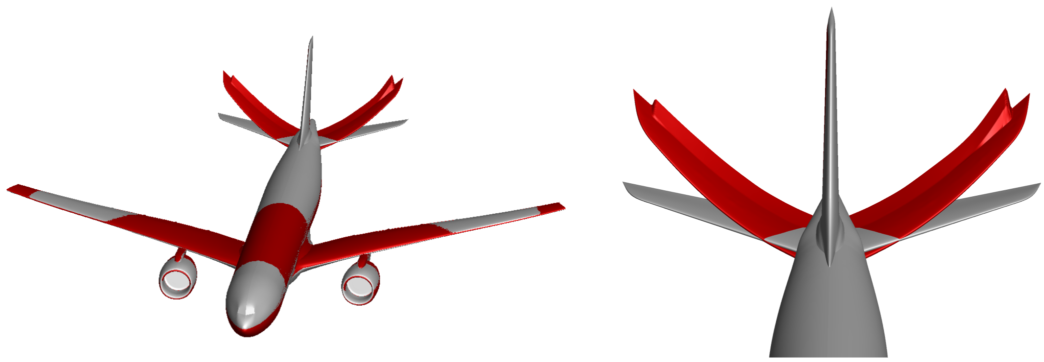

Figure D.6: Visualization of eigenmode 20: 2n HTP bending

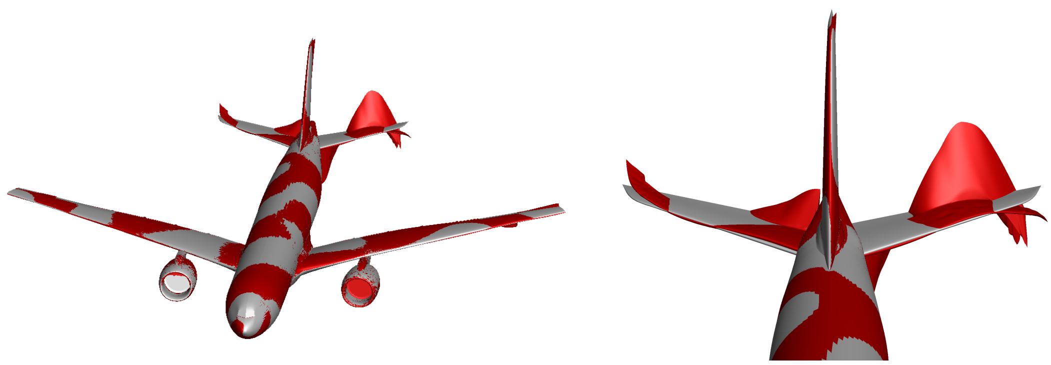

Figure D.7: Visualization of eigenmode 83: Non-symmetric HTP bending mode with 3n elevator bending

D.3. Mode shapes Aileron Outer Bracket FC

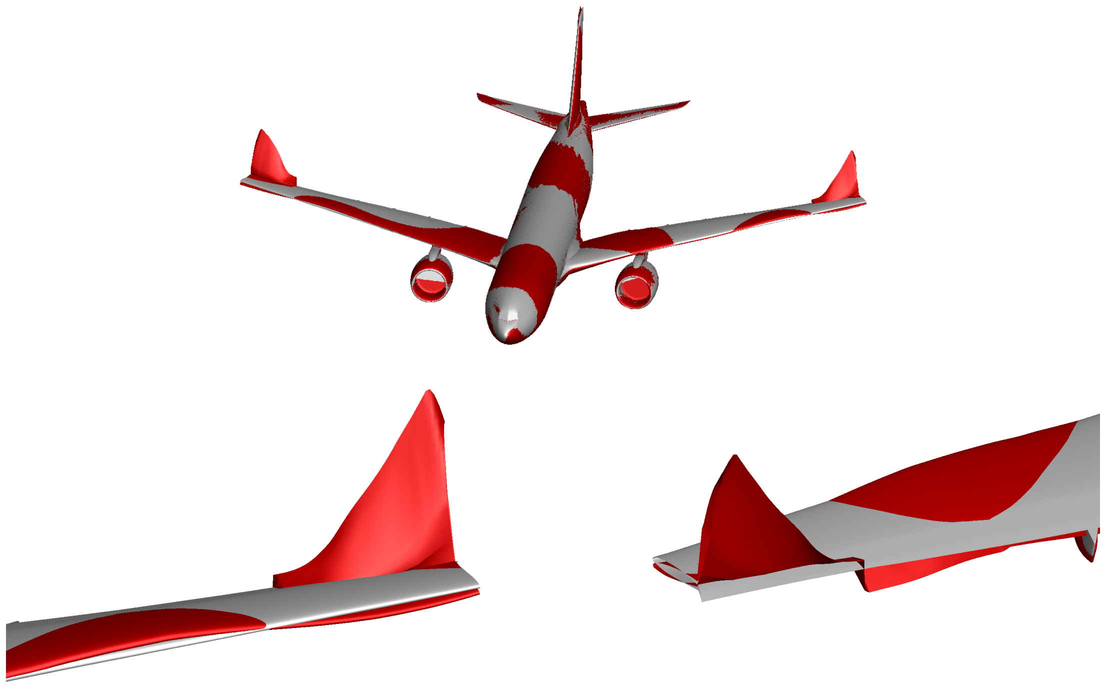

(a) Front view wing tip

(b) Rear view wing tip

Figure D.8: Visualization of eigenmode 63: Outer aileron rotation

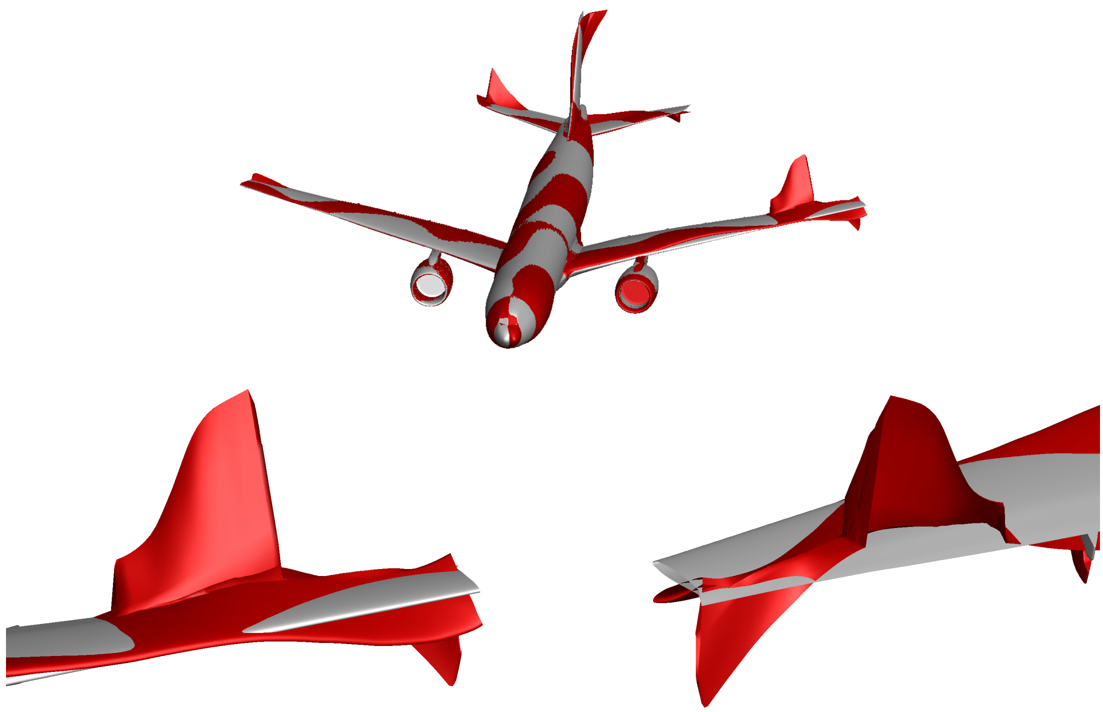

(a) Front view wing tip

(b) Rear view wing tip

Figure D.9: Visualization of eigenmode 72: Differential rotation of left wing inner and outer aileron

D.4. Mode shapes Rudder Outer Bracket FC

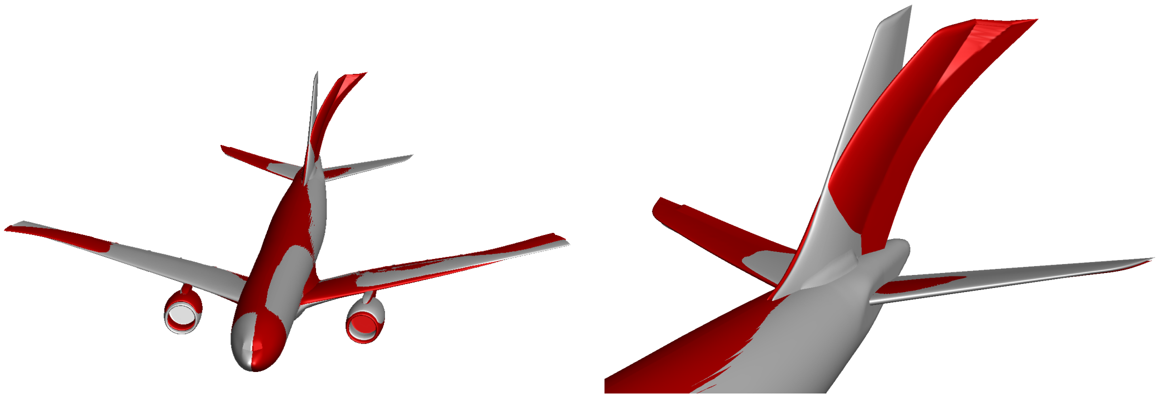

Figure D.10: Visualization of eigenmode 26: VTP bending

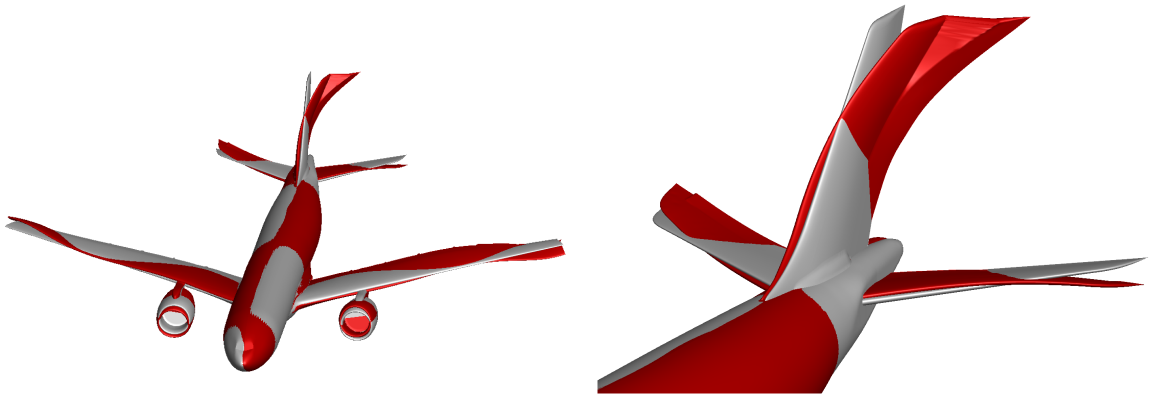

Figure D.11: Visualization of eigenmode 31: VTP bending combined with a 3N HTP bending and wing torsion

D.5. Mode shapes of modal basis enrichment studies

Added mode for each of the four modal basis enrichment methods

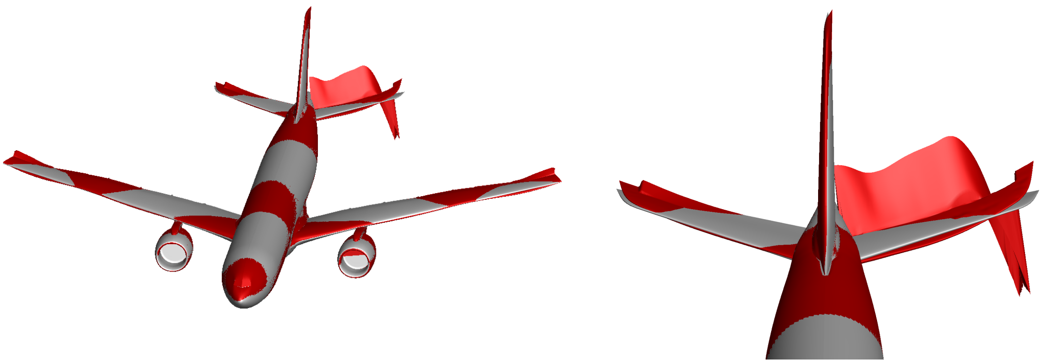

Figure D.12: Added mode for enrichment method 1

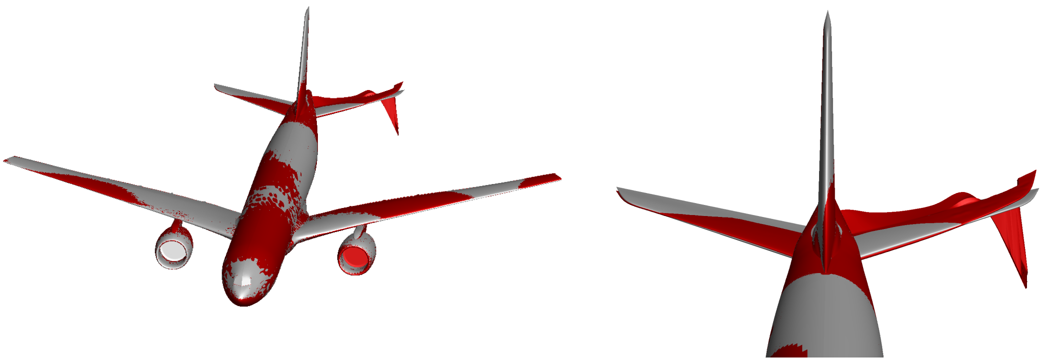

Figure D.13: Added mode for enrichment method 2

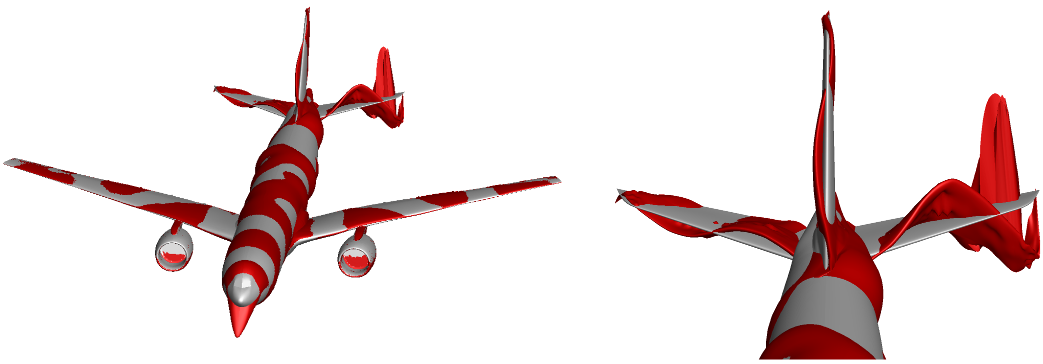

Figure D.14: Added mode for enrichment method 3

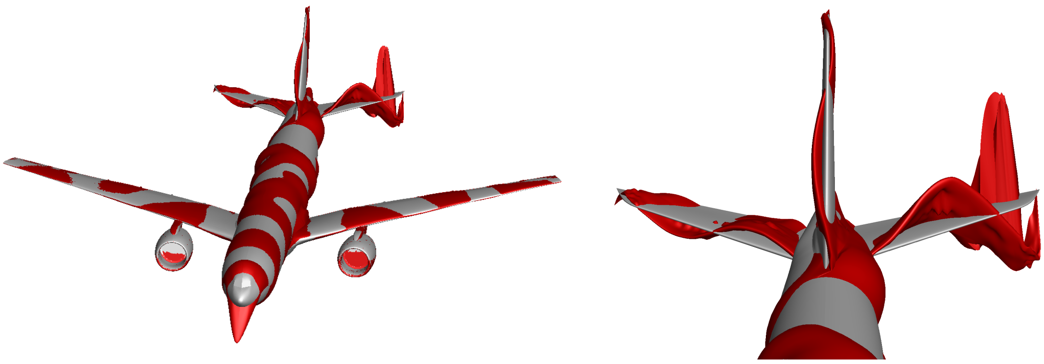

Figure D.15: Added mode for enrichment method 4

Three most critical error modes

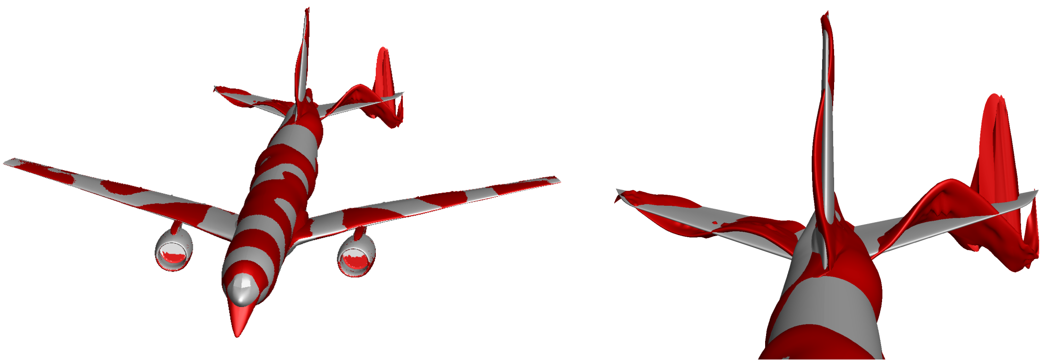

Figure D.16: Error Mode 1

Figure D.17: Error Mode 2

Figure D.18: Error Mode 3

Bibliography

[1] Edward Albano and William P. Rodden. A Doublet-Lattice Method for Calculating Lift Distributions on Oscillating Surfaces in Subsonic Flows. *AIAA Journal*, 7(2), February 1969.

[2] R. J. Allemang. The Modal Assurance Criterion - Twenty Years of Use and Abuse. *Sound and Vibration*, August 2003.

[3] C. B. Allen and T. C. S. Rendall. Efficient mesh motion using radial basis functions with data reduction algorithms. *Journal of Computational Physics*, 228:6231–6249, May 2009.

[4] H. Barnewitz and B. Stickan. Improved Mesh Deformation. In B. Eisfeld, H. Barnewitz, W. Fritz, and F. Thiele, editors, *Management and Minimisation of Uncertainties and Errors in Numerical Aerodynamics, volume 122 of Notes on Numerical Fluid Mechanics and Multidisciplinary Design*, pages 219–243. Springer Berlin Heidelberg, 2013.

[5] K.-J. Bathe. *Finite Element Procedures*. Prentice Hall, Pearson Education, Inc., 2nd edition, 2014.

[6] A. Beckert and H. Wendland. Multivariate interpolation for fluid-structure-interaction problems using radial basis functions. *Aerospace Science and Technology*, 5(2), 2001.

[7] P. Bekemeyer and S. Timme. Reduced Order Transonic Aeroelastic Gust Response Simulation of Large Aircraft. In *35th AIAA Applied Aerodynamics Conference*, Denver, Colorado, 2017. AIAA Paper.

[8] P. Bekemeyer, R. Thormann, and S. Timme. Rapid gust response simulation of large civil aircraft using computational fluid dynamics. *The Aeronautical Journal*, 121(1246):1795–1807, December 2017.

[9] H. Bijl, A. H. van Zuijlen, and A. de Boer. *Fluid-structure interaction, an introduction to numerical coupled simulation*. Delft University of Technology, 2007-2008.

[10] M. Brüderlin, B. Stickan, B. Schulze, and M. Behr. Numerical Aero-Structural Dynamic Simulations of the ASDMAD Wing. In A. Dillmann, A. Heller, E. Krämer, C. Wagner, and C. Breitsamter, editors, *New Results in Numerical and Experimental Fluid Mechanics X: Contributions to the 19th STAB/DGLR Symposium*, Munich, Germany, 2016. Springer International Publishing.

[11] A. Celic and E. H. Hirschel. Comparison of Eddy-Viscosity Turbulence Models in Flows with Adverse Pressure Gradient. *AIAA Journal*, 44(10), October 2006.

[12] A. R. Collar. The Expanding Domain of Aeroelasticity. *Journal of Royal Aeronautical Society*, 50: 613–636, 1947.

[13] A. de Boer, A. H. van Zuijlen, and H. Bijl. Review of coupling methods for non-matching meshes. *Computer Methods in Applied Mechanics and Engineering*, 196:1515–1525, 2007.

[14] I. E. Garrick and W. H. Reed. Historical Development of Aircraft Flutter. *Journal of Aircraft*, 18(11), November 1981.

[15] K. C. Hall, J. P. Thomas, and E. H. Dowell. Proper Orthogonal Decomposition Technique for Transonic Unsteady Aerodynamic Flows. *AIAA Journal*, 38(10):1853–1862, October 2000.

[16] H. J. Hassig. An Approximate True Damping Solution of the Flutter Equation by Determinant Iteration. *Journal of Aircraft*, 8(11), November 1971.

[17] S. Hickel. *CFD for aerospace engineers: Reynolds-Averaged Navier-Stokes*. Delft University of Technology, 2016-2017.

[18] M. Iatrou, C. Breitsamter, and B. Laschka. Small Disturbance Navier-Stokes Equations: Application on Transonic Two-Dimensional Flows Around Airfoils. In Hans-Josef Rath, Carsten Holze, Hans-Joachim Heinemann, Rolf Henke, and Heinz Hönlinger, editors, *New Results in Numerical and Experimental Fluid Mechanics V*, pages 471–478, Berlin, Heidelberg, 2006. Springer Berlin Heidelberg. ISBN 978-3-540-33287-9.

[19] C. Kaiser, R. Thormann, D. Dimitrov, and J. Nitzsche. Time-Linearized Analysis of Motion-Induced and Gust-Induced Airloads with the DLR TAU Code. In *64th Deutscher Luft- und Raumfahrtkongress*, pages 1–9, Rostock, Germany, 2015. Deutsche Gesellschaft für Luft- und Raumfahrt. ISBN 370189.

[20] E. Kreiselmaier and B. Laschka. Small Disturbance Euler Equations: Efficient and Accurate Tool for Unsteady Load Prediction. *Journal of Aircraft*, 37(5), September-October 2000.

[21] J. L. Lumley. The Structure of Inhomogeneous Turbulent Flows. In A. M. Yaglam and Tatarsky V. I., editors, *Proceedings of the International Colloquium on the Fine Scale Structure of the Atmosphere and Its Influence on Radio Wave Propagation*, Nauka, Moscow, 1967. Doklady Akademii Nauk SSSR.

[22] M. Meinel and G. Einarsson. The FlowSimulator framework for massively parallel CFD applications. *PARA 2010: State of the Art in Scientific and Parallel Computing*, June 2010.

[23] A. Pechloff and B. Laschka. Small Disturbance Navier-Stokes Method: Efficient Tool for Predicting Unsteady Air Loads. *Journal of Aircraft*, 43(1), January-February 2006.

[24] A. Pechloff and B. Laschka. Small Disturbance Navier-Stokes Computations for Low-Aspect-Ratio Wing Pitching Oscillations. *Journal of Aircraft*, 47(3), May-June 2010.

[25] A. Pechloff, M. Iatrou, C. Weishäupl, and B. Laschka. The Small Disturbance Navier-Stokes Equations: Development of an Efficient Method for Calculating Unsteady Air Loads. In C. Breitsamter, B. Laschka, H.-J. Heinemann, and R. Hilbig, editors, *New Results in Numerical and Experimental Fluid Mechanics IV*, pages 278–285, Berlin, Heidelberg, 2004. Springer Berlin Heidelberg. ISBN 978-3-540-39604-8.

[26] A. Schoon. Flutter Solver PKREG: Theoretical and User's manual. Technical Report B081/02, Airbus, December 2002.

[27] D. M. Schuster, D. D. Liu, and L. J. Huttsell. Computational Aeroelasticity: Succes, Progress, Challenge. *Journal of Aircraft*, 40(5), September-October 2003.

[28] D. Schwamborn, T. Gerhold, and R. Heinrich. The DLR TAU-code: Recent applications in research and industry. In *European Conference on Computational Fluid Dynamics*, Egmond aan Zee, The Netherlands, 2006. ECCOMAS CFD.

[29] Marilyn J. Smith, Dewey H. Hodges, and Carlos E. S. Cesnik. Evaluation of Computational Algorithms Suitable for Fluid-Structure Interactions. *Journal of Aircraft*, 37(2), March-April 2000.

[30] MSC Software. MSC-Nastran, 2018. URL `http://www.mscsoftware.com`.

[31] P. R. Spalart and S. R. Allmaras. A One-Equation Turbulence Model for Aerodynamic Flows. In *30th Aerospace Sciences Meeting & Exhibit*, Reno, NV, January 1992. Boeing Commercial Airplane Group, AIAA.

[32] B. Stickan. *Explanation of AEROSTABIL Limit-Cycle Oscillations via High-Fidelity Aeroelastic Simulations*. Deutches Zentrum für Luft- und Raumfahrt, Institut für Aeroelastik, 2018. ISBN 1434-8454.

[33] B. Stickan, H. Bleecke, and S. Schulze. NASTRAN Based Static CFD-CSM Coupling in FlowSimulator. In N. Kroll, R Radespiel, J. W. van der Burg, and K. Strensen, editors, *Computational Flight Testing, volume 123 of Notes on Numerical Fluid Mechanics and Multidisciplinary Design*, pages 223–234. Springer Berlin Heidelberg, 2013.

[34] B. Stickan, F. Schöder, S. Helm, and H. Bleecke. On Recent Advances in Industrial High-Fidelity Aeroelasticity. In R. Heinrich, editor, *AeroStruct: Enable and Learn How to Integrate Flexibility in Design, volume 138 of Notes on Numerical Fluid Mechanics and Multidisciplinary Design*, pages 85–101. Springer Berlin Heidelberg, 2015.

[35] K. Taira, S. L. Brunton, S. T. M. Dawson, C. W. Rowley, T. Colonius, B. J. McKeon, O. T. Schmidt, S. Gordeyev, V. Theofilis, and L. S. Ukeiley. Modal Analysis of Fluid Flows: An Overview. *AIAA Journal*, 55(12), December 2017.

[36] R. Thormann and M. Widhalm. Linear-Frequency-Domain Predictions of Dynamic-Response Data for Viscous Transonic Flows. *AIAA Journal*, 51(11), November 2013.

[37] W. P. W. van den Bekerom. Sensitivity of Flutter Predictions to Aerodynamic Input for a Realistic Aircraft Configuration. Master's thesis, Delft University of Technology, November 2010.